# QUANTITATIVE ELECTRON DIFFRACTION AND SPECTROSCOPY AND THEIR APPLICATION ON POLYMERS AND 2D MATERIALS

CHEN CHANGSHENG

PHD

The Hong Kong Polytechnic University

2024

THE HONG KONG POLYTECHNIC UNIVERSITY

Department of Applied Physics

# Quantitative electron diffraction and spectroscopy and their application on polymers and 2D materials

Chen Changsheng

A thesis submitted in partial fulfilment of the requirements for the degree of Doctor of Philosophy

August 2023

# CERTIFICATION OF ORIGINALITY

I hereby declare that this thesis is my own work and that, to the best of my knowledge and belief, it reproduces no material previously published or written, nor material that has been accepted for the award of any other degree or diploma, except where due acknowledgement has been made in the text.

_______________________________________ (Signed)

___Chen Changsheng______________ (Name of student)

# Abstract

The determination of structures and phases in functional materials is crucial for understanding and optimizing their properties. However, traditional direct-imaging electron microscopy techniques often fall short in identifying structural orderings and phases of dose-sensitive materials at the nanoscale, such as some semicrystalline polymers and emerging 2D materials. Their intrinsic structure can be rapidly damaged under electron beam irradiation, like a few e/Å$^2$ for polymers and hundreds of e/Å$^2$ for some 2D materials, and can only be identified on certain zone axes. Within the developing low-dose methods, four-dimensional scanning transmission electron microscope (4D-STEM) has demonstrated the potential to unveil the hierarchical structures and spatial distribution of degree of crystallinity in polymers. Additionally, thanks to single-electron direct detection and low-sampling conditions, electron energy loss spectroscopy (EELS), which contains rich and strong signals within the energy range of valence electron, becomes another dose-efficient avenue for phase identification at the nanoscale and on various zone axes. Furthermore, quantitative analysis of electron diffraction and EEL spectra is implemented to fully reveal nuanced differences in these data and elucidate underlying reasons.

In this work, we first investigated the electron beam effects on spherulite thin films made of polyethylene (PE), polycaprolactone (PCL), and poly(3-hexylthiophene) (P3HT) at room temperature and cryogenic condition for identification of polymeric structures and phases with minimized artifacts. The beam effects on structure and chemical bonding evolution are demonstrated by quantitative electron diffraction and spectroscopy. Thus, both amorphization and mass loss from electron beam irradiation have been clearly identified, most of which can be suppressed effectively by cryo-protection. Moreover, the different degradation paths are revealed on PE/PCL and on P3HT which shows an individual two-stage damage process at cryogenic temperature. Furthermore, the methodology employed in this study also establishes a robust framework for quantitatively analyzing the crystalline and amorphous components paving a path for the spatial distribution of degree of crystallinity in polymers.

With knowledge of polymer damage under electron beams, we optimized the acquisition conditions of 4D-STEM technique on PE and PCL spherulite thin films. Our quantitative algorithm for 4D electron diffraction allowed us to examine the microstructures of these films, including their circular symmetry and degree of crystallinity distribution. In PE, we observed a growth direction along [1-10], and a twisting motion approximately around the crystallographic b axis in the lamellae within the spherulites. Besides, its orientation distribution exhibited continuous circular symmetry. Similarly, PCL also displays a growth direction along the [1-10] in the radial direction. However, PCL does not exhibit a twist in the lamellae. Instead, an inhomogeneous crystallinity pattern is observed in the tangent direction, forming a radial arrangement of crystalline and amorphous regions. Furthermore, an increase of crystallinity from spherulite cores to peripheries is revealed in both PE and PCL. Hence, our developed technology using the 4D-STEM system showcases great potential in

uncovering local information, but additional research is necessary to fully exploit its capabilities.

For another dose-sensitive material, namely the 2D $In_2Se_3$, its second phase can form down to a single quintuple layer (~ 1.0 nm) thus requiring high-resolution characterization. However, the crystal structures of the various phases show only subtle differences on specific zone axes, and defects tend to occur more frequently under high electron dose irradiation of conventional STEM imaging. As a result, these factors pose significant obstacles to overcome in terms of quantitative analysis and TEM techniques. In this case, the 4D-STEM technique becomes ineffective owing to the large overlap of diffraction disks from a small probe. Fortunately, EELS can identify the phase of $\alpha/\beta'$ $In_2Se_3$ on both 2D plane and cross-section with a slightly lower dose than STEM imaging. The phase identification using quantitative EELS has a resolution of approximately 1.1 nm. Besides, the *in-situ* results of EELS and XRD not only confirm the robustness of our observations but also reveal two factors that contribute to the difference in plasmon energy of EELS between the $\alpha/\beta'$ phases: unit cell volumes in a single quintuple layer and equivalent valence electrons. Finally, our findings are further supported by first-principles calculations and may have broader implications for other chalcogenides and transition metal materials.

# Acknowledgements

First and foremost, I would like to express my gratitude to my supervisor, Dr. Ye Zhu, for his support and guidance over the past three years and for introducing me to the fascinating field of electron microscopy. With his help, I was able to access state-of-the-art electron microscopy equipment and engage in exciting cutting-edge research. Thank you, teacher Zhu, for providing me with the opportunity to pursue my Ph.D., which is a unique and rewarding life experience.

Time flies, and the three years have been fleeting. In these short yet enriching years, I have gradually learned how to acquire high-quality electron microscopy data and analyze it effectively. However, the low-hanging apples I picked were all due to the following helps: 1. Stable and well-maintained electron microscopy systems. I am immensely grateful to the engineers Lu, Wei and Lai, Mark, Ka-Hei who have maintained and tweaked the various microscopes on a day-to-day basis. 2. Progressive guidance in electron microscopy. I would like to thank my supervisor Zhu, Ye again and Dr. Guo, Xu-Yun for their professional guidance and valuable advice, which have saved me from trial and error in my experiments. 3. High-quality samples. As my knowledge in organic sample preparation was limited, I want to express my gratitude to Professor Li, Han-Ying and his student Chen, Min from Zhejiang University. Their expertise in synthesizing polymer samples has allowed me to observe intriguing results. I would also like to thank Dr. Xu Chao, who not only provided me with exquisite two-dimensional (2D) $In_2Se_3$ samples and exclusive sample preparation knowledge, but also provided me with numerous interesting insights during our daily discussions and learning. 4. Support of First-principles calculation. I am thankful to Professor Luo, Xin and Dai, Min-Zhi from Sun Yat-Sen University. Their extensive computational experience has helped me understand the deeper physical implications of my experimental results. Additionally, I would like to express my gratitude to Dr. Che, Xiang-Li, Dr. Zhao, Guang-Ming, and Yao, Yun-Duo for their assistance.

I would like to thank the members of Dr. Zhu's lab and my office colleagues for making my graduate research life enjoyable. They are Guangming Zhao, Shanru Yan, Yunduo Yao, Xuyun Guo, Chao Xu, Xiangli Che, Zhihang Xu, Chen Yang, Yezhou Hu, Cenchen Zhong, Tiancheng Liu, Luwei Peng, Ruinan He, Haifa Qiu, and Xinyou Zhang.

Lastly, I want to express my deepest gratitude to my family, including my parents, sister, brother-in-law, uncle, and aunt, for their continuous support throughout the years, enabling me to complete my studies. I would like to express special thanks to my wife, Ren, Jiu-Ju, for her constant support and dedication.

# Table of contents

# List of Figures and Tables

# List of Abbreviations

| | |
|---|---|
| 2D | Two-dimensional |
| 4D-STEM | Four-dimensional scanning transmission electron microscope |
| ADF | Annular dark field |
| AFM | Atomic force microscope |
| CBED | Convergent beam electron diffraction |
| COM | Center of mass |
| CHT | Circular Hough transform |
| CVD | Chemical vapor deposition |
| DFT | Density function theory |
| DP | Diffraction pattern |
| EBSD | Electron backscatter diffraction |
| EDX | Energy dispersive X-ray spectroscopy |
| EELS | Electron energy-loss spectroscopy |
| EMPAD | Electron microscope pixel array detector |
| FET | Field-effect transistor |
| FFT | Fast Fourier transform |
| FIB | Focused ion beam |
| FOV | Field of view |
| FWHM | Full widths at half-maximum |
| HAADF | High-angle annular dark field |
| HDR | High dynamic range |
| LDA | Local density approximation |
| LED | Light-emitting diode |
| MAPS | Monolithic active pixel sensor |
| MOF | Metal organic framework |
| OFET | Organic field-effect transistor |

| | |
|---|---|
| P3HT | Poly(3-hexylthiophene) |
| PAW | Projector-augmented wave |
| PCL | Poly(ε-caprolactone) |
| PCA | Principal component analysis |
| PE | Polyethylene |
| POM | Polarized optical microscope |
| ROI | Region of interest |
| RT | Room temperature |
| SAED | Selected-area electron diffraction |
| SEM | Scanning electron microscope |
| TEM | Transmission electron microscope |
| TMD | Transition-metal dichalcogenide |
| VASP | Vienna ab initio simulation package |
| VEELS | Valence electron energy-loss spectroscopy |
| VTEC | Volume thermal expansion coefficient |
| XRD | X-ray diffraction |
| ZLP | Zero-loss peak |

# Chapter 1 Introduction

Polymers and two-dimensional (2D) materials are widely and potentially used in various fields due to their attractive physical and chemical properties. Extensive research and efforts have been invested in studying their structures, phases, and morphologies for their better performance. However, the direct observation of their structures, phases, and morphologies at nanoscale by conventional electron microscopy techniques remains challenging due to their sensitivity to the electron illumination dose [1-3]. Therefore, new methods are needed for studying the two materials. This thesis aims to quantitatively investigate the microstructure and distribution of phases in polymers by utilizing low-dose four-dimensional scanning transmission electron microscope (4D-STEM), and distribution of phases of $\alpha / \beta'$ indium selenide ($In_2Se_3$) at the nanoscale by low-dose electron energy-loss spectroscopy (EELS).

This chapter introduces the application of transmission electron microscope (TEM) in detecting the structure of polymers and reviews its advantages, limitations, and advancements. The interaction between the electron beam and materials, which determines what can be observed and how materials are damaged, is also discussed. This part serves as the foundation for our quantitative work on the degradation of polyethylene (PE), poly(ε-caprolactone) (PCL), and Poly(3-hexylthiophene) (P3HT) under electron beam in Chapter 2. Additionally, we review the hierarchical structures of polymeric spherulites ranging from micro to nano scales, and the developing 4D-STEM technique for polymer science. This discussion lays the groundwork for our findings on structures in polymer spherulites, which are elaborated in Chapter 3. Finally, we further discuss and quantify the plasmon energy by valence electron energy-loss spectroscopy (VEELS) for identification of the polymorphs of $In_2Se_3$. Chapter 4 provides details regarding these discussions and findings.

## 1.1 TEM for Polymers research

Polymer materials are ubiquitous and have become one of the cornerstones of modern society due to their low cost, light weight, good performance, and diverse functionality. In particular, in the field of organic electronics, polymers play a crucial role and are revolutionizing the current usage scenario and product performance in subdivision fields such as light-emitting diodes (LEDs), field-effect transistors (FETs), and solar cells. TEM has made significant contributions to the advancement of polymer science and engineering due to its unmatched resolution and elemental analysis capability.

As early as 1959, TEM was utilized to elucidate the nucleation mechanism for the formation of Nylon-6 spherulites [4]. In the 21 century, TEM revealed the new structures within a terpolymer [8] and the self-assembly of crystalline nanotubes from amphiphilic copolymers [9]. However, observation of morphology and structure at the nanoscale is still challenging owing to the inevitable electron beam damage. Thus, the structural analysis for the better understanding the properties of polymers are always scarce.

### 1.1.1 Advantages and limitations of TEM/STEM

In conventional microscopy technologies, TEM/STEM can have sub-angstrom resolution benefiting from advanced aberration correctors. Meanwhile, element distribution and a variety of local structural information including crystallinity [10-15], crystalline orientation [16], crystal structure [17-20], band structure [21-23], and radical groups [24,25], can be acquired simultaneously by TEM/STEM-based techniques such as electron diffraction, energy dispersive X-ray spectroscopy (EDX) and EELS.

Nevertheless, these advantages and application are not always feasible in polymer science, because of the two main challenges from the electron microscope: 1) low imaging contrast due to the low-atomic-number elements composing polymers; 2) sensitivity of polymers to ionizing radiation. In the TEM, the dose-limited resolution follows **Equation (1.1)**:

$$Cd = SNR/\sqrt{DQE\ f\ D_c} \tag{1.1}$$

where $C$ is the contrast, $d$ is the resolution, $SNR$ is the signal-to-noise ratio, $DQE$ is the quantum detection efficiency of the electron detectors, $f$ is the fraction of electrons contributing to the image, and $D_c$ is the critical electron dose used to evaluate the robustness of materials against electron beam [26-28] and equaling an accumulating electron dose after that the original intensity (diffraction or EEL peaks) reduces to its 1/e. Higher resolution and better contrast require the greater electron dose which conversely causes stronger electron beam damage. Unfortunately, the critical electron doses of the most polymers are only a few e/Å$^2$, which makes it extremely challenging to acquire atomic-resolution images.

### 1.1.2 Electron beam effects and their measurement

Therefore, the realistic tasks for investigating the intrinsic structures of dose-sensitive materials primarily involve monitoring and understanding the effects of the beam. The beam damage mainly includes knock-on damage, radiolysis, charging, and heating, as summarized in **Figure 1.1**. Atoms in the crystal lattice can be displaced to interstitial positions or even sputtered directly by the incident electron beam, so-called knock-on damage, when beam energies beyond a certain threshold energy [26]. This can induce defects, amorphization, atom diffusion and segregation, and phase change. Energy-momentum transfer from the electron beam through inelastic scattering causes excitation of atoms and electrons leading to either changes in bonding environment or thermal vibrations, namely the radiolysis and heating effects [26-33]. Under these beam damage, the intrinsic structural information of specimens can be covered by artefacts or even destroyed quickly [1,19,34,35].

The common methods for recording the beam effects include TEM/STEM images [1,36 ,37], SAED patterns [39-41], and EEL spectra [34,42-45]. TEM/STEM image analysis is straightforward for estimating and understanding the electron damage, such as that reported at metal organic framework (MOF) system [36,37] and perovskite-structure materials [38]. However, this method requires high electron dose (usually over 10000 e/Å$^2$) or high *DQE* exclusively belonging to single-electron detection cameras (still require dose over tens of e/Å$^2$). In comparison, the methods based on SAED patterns and EEL spectra can performed on an ultralow dose rate by increasing radiation area. SAED patterns can offer the quantizable information on crystalline and amorphous components, and EEL spectra can exhibit the signal of radical groups and bonding change in different electron loss-energy range.

In Chapter 2, we use quantitative SAED patterns and EEL spectra to reveal the beam effects on the three polymers. The two methods have been proven effective on other polymers by previous study [34, 39-44]. **Figure 1.2** gives two examples of beam effects on polymers through diffraction patterns (DPs) and EEL spectra [39,43]. **Figure 1.2a** demonstrate the SAED patterns of a P3HT/PCBM bulk heterojunction under electron dose of 0 and 50 e/Å$^2$. The diffraction ring of P3HT disappears while that of PCBM still holds. The quantitative intensity of their diffraction rings as functions of accumulated dose with different dose rates is shown in **Figure 1.2b-c** revealing a 15 times more stable beam damage path in PCBM than P3HT. **Figure 1.2d-e** show the rr-P3HT EEL spectra at different electron doses and its integrated EELS intensities in low energy-loss regions as a function of electron dose. A decrease in peak intensities and a shift in peak positions toward higher energies (from 2.6 eV to 3.2 eV) can be observed with dose increasing.

Although, the damages are recorded, yet how the polymers are damaged is obscure due to the lack of quantitative explanation to the damage process. To understand how the different electron beam effects impact polymers, more unambiguous results, more detailed analysis, and slower damage rate are required.

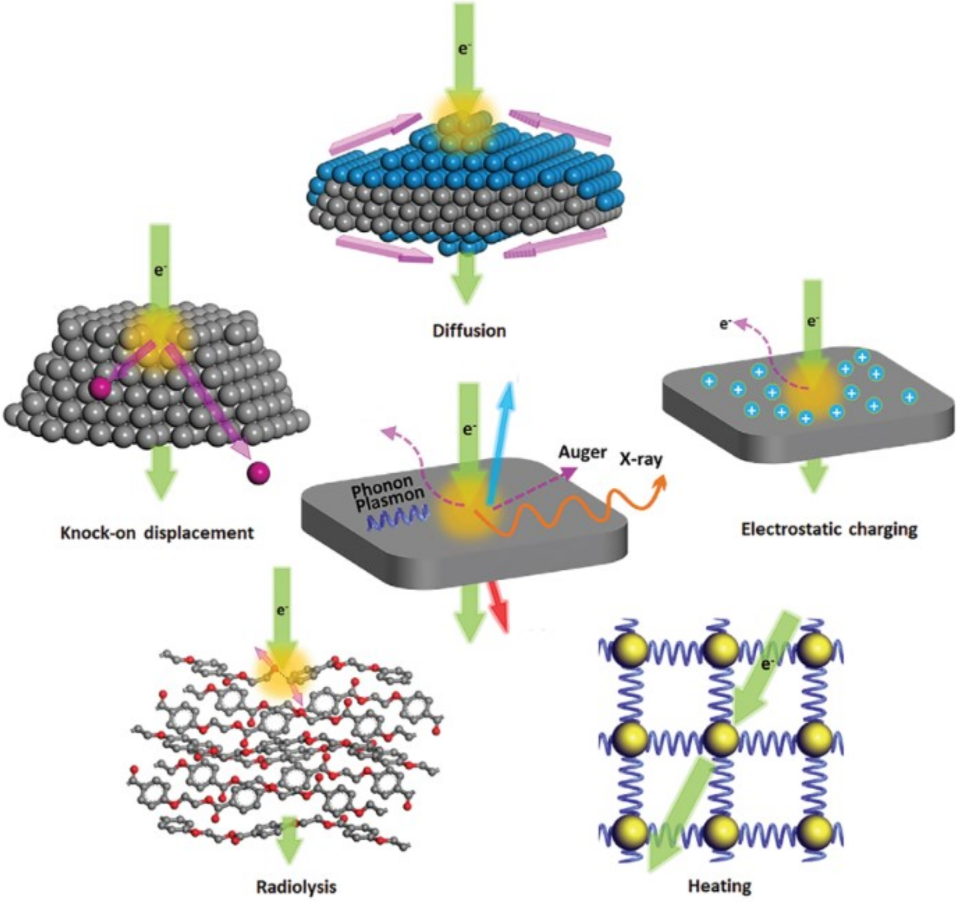

**Figure 1.1.** Schematic demonstration of the primary inelastic scattering interactions between a high-energy electron beam and a specimen. The electron beam effects usually include atom movement, knock-on displacement, radiolysis, heating, and charging which can change the pristine structure of samples to some extent, and other consequent signals mainly contain plasmon, auger electrons, and X-ray. (reproduced from [1])

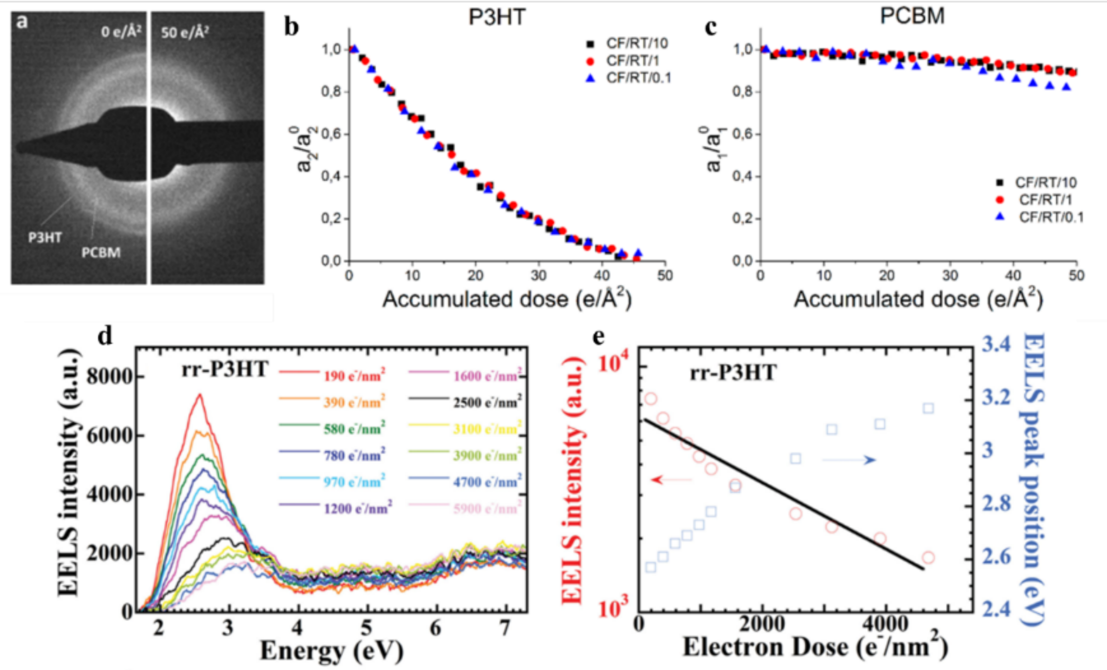

**Figure 1.2.** The beam damage can be recorded quantitatively by Selected-area electron diffraction (SAED) and EELS. (a) SAED patterns before and after exposure to 50 e/Å$^2$. (b, c) Fading of relative diffraction intensity as a function of electron dose for components of P3HT (b) and PCBM (c). (d) EEL spectra at various radiation dose. (e) integrated EELS intensities as a function of electron dose [39,43]. (reproduced from [39] and [43])

### 1.1.3 Strategies against electrons damage

There are several methods for acquiring better data and mitigating electron damage. As expressed in the **Equation (1.1)**, high detection efficiency, better contrast, and greater critical dose can improve the final resolution. High detection efficiency has been achieved in detectors coupled with direct-detection and electron counting technologies [46-48], while contrast can be improved by using phase imaging mode such as ptychography and holography [49,50,51]. These technologies enable acquiring the high-quality results under lower electron dose.

Strategies for increasing critical dose $D_c$ includes lowering temperature, adjusting voltage of electron beam, changing dose rate, surface coating, and changing sample preparation. Lowering the sample temperature diminishes radiolysis and heating effects resulting in a higher critical dose $D_c$ due to the suppression of thermal vibration and electronic excitations at low temperatures [27,28,33,40,52]. Increasing accelerating voltage results in a greater inelastic scattering mean free path, thus lowering the radiolysis effect in most polymers [28,33,40,52]. Additionally, an ultrafast (down to femtosecond) pulsed-beam approach reveals a new path to decrease beam damage [44,53,54]. Specimen coating using carbon, metal or metal oxide as the protecting layer is effective to minimize the surface sputtering [27,28]. Finally, it is noted that oxygen-free and water-free sample preparation and the addition of antioxidants can also effectively decrease beam damage [34,35,39], because of depressed radiolysis effects from fewer free radical.

In our work, we prepared PE, PCL, and P3HT thin film for electron degradation research, since they are not only widely used but also representative in atomic structure. PE is one of the simplest polymers (Figure 1.3a) which can be consider as a model for understanding principal interactions between electron and polymer main chains. PCL with a simple sidechain and low sidechain density (Figure 1.3b) have a very similar crystal model to PE, which is thus used as a comparison of PE. As for P3HT, a popular low band gap polymer donor with applications in organic photovoltaics, is composed of π chains and long sidechains (Figure 1.3c) and thus have a different crystal model to PE, which is used to evaluate the effect of π chains and π stacking. we used the low-temperature method to observe a higher critical dose on PE, PCL, and P3HT via quantitative SAED patterns and EEL spectra in both low-loss and core-loss ranges. This allowed us to demonstrate more details including crystalline and amorphous components and chemical bonding evolution in their beam degradation processes, which further helped to illustrate the underlying damage mechanism. This aspect is elaborated in Chapter 2.

## 1.2 4D-STEM for Polymers research

As stated in the previous chapter, one method to lower the dose is by using the electron diffraction due to its larger illuminated area. However, classical SAED, which acquires global information from an area of hundreds of nanometers, loses local information at the nanoscale. With advancements over the past decade, the new generation of cameras with high dynamic range (HDR) and high acquisition speed, such as electron microscope pixel array detector (EMPAD) [46,47] and monolithic active pixel sensors (MAPS) [48], have given researchers power to quickly acquire the accurate and precise signal.

HDR detectors allow researchers to get better results while exposing samples to lower doses, significantly reducing damage to samples. Specifically, based on the direct detection of single electron and high-speed acquisition in EMPAD, we can acquire a sharp diffraction pattern within an accumulated electron dose of 0.4 $e/Å^2$ by using an electron probe with a current of ~0.5 pA and a full width at half maximum (FWHM) of ~10nm. This dose is low enough for polymer measurements even at room temperature and does not sacrifice spatial resolution, which is still better than 10nm and unmatched by other techniques.

In addition to the superior detection capabilities, a high-speed camera enables the acquisition of 4D datasets including the two dimensions in real space and two dimensions in reciprocal space ($x \times y \times k_x \times k_y$), as illustrated in **Figure 1.3**. Although, the quantitative analysis of these datasets is complicated and resource-intensive, it allows for the mapping and reconstruction of local information within diffraction patterns, including orientation, strain, and degree of crystallinity. Panova et al. reported the visualization of crystalline nanostructure and orientation of organic molecular thin film based on the 4D-STEM technology [55,56], which expand the fundamental understanding of the polymer structure model.

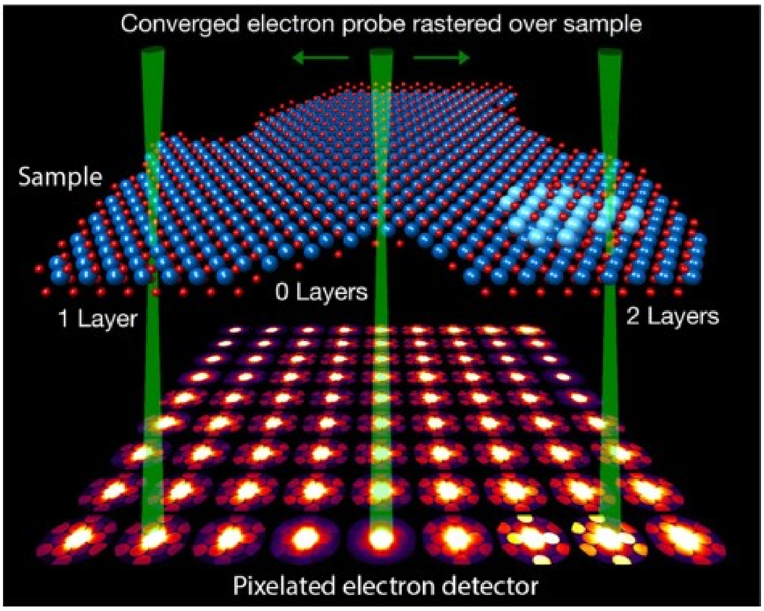

**Figure 1.3.** Experimental 4D-STEM measurement of a dichalcogenide 2D material where the diffraction patterns are recorded in each scanning position. (reproduced from [57])

Moreover, the scanning region of interest (ROI) can span over ten micrometers enabling the observation of complex hierarchical structures on polymers and quantitative analysis of structure and phases. Therefore, this technique can provide more intricate details and structural identification that cannot be obtained through other methods.

## 1.3 Polymeric structure

Although polymers are used ubiquitously in various fields, their properties have not been fully exploited due to a lack of knowledge about their formation mechanisms and microstructures [1,2]. One reason for this is the extreme challenge of probing the structures of semi-crystalline polymers at the nanoscale. Among these, polymeric spherulites are particularly intriguing due to their widespread use and intricate microstructures that remain poorly understood. However, with the use of our 4D-STEM system, the microstructures of polymeric spherulites can now be reconstruct.

Polymers composed of varying ratios of amorphous and crystalline components are extremely beam-sensitive, which hinders the detection of intrinsic phases. It thus remains unclear whether a semi-crystalline polymer has a uniform structure or is inhomogeneous with crystallinity varying spatially. Thanks to an understanding of polymer damage and our low-dose 4D-STEM system, optimized conditions without artefacts can be established for studying the phase distribution of polymers.

### 1.2.1 Degree of crystallinity and structure model

Polymers can be classified as crystalline and semi-crystalline by the arrangement (random or ordered) of their long polymeric chains, which are made up of numerous repeating units called monomers. However, it is difficult to explicitly define a degree of crystallinity due to a lack of quantifiable references. Usually, the relative degree of crystallinity is more common used and there is a simple method for estimating it by superficial results. From a morphological perspective, the ordered arrangement of long chains generates regular shapes and smooth surfaces, while the semi-crystalline polymers composed of crystalline and amorphous components can produce various morphology, such as one-dimensional (fibers), two-dimensional (lamellae), and three-dimensional (spherulites, dendrites, and shish kebab structures) structures [2,3,30]. These microstructures in semi-crystalline polymers result from their crystallizing process driven by the complex intermolecular interaction, hydrogen bonds, and covalent bonds [2,3].

Furthermore, many physical properties of polymers such as mechanical, optical, and electronic properties are determined by their degree of crystallinity and crystallizing process. Crystalline and amorphous polymers often have respective advantages and disadvantages. For example, different crystallization processes can affect the efficiency of organic photovoltaics of P3HT solar cells [58], while the crystallinity of polymeric dielectrics can improve the performance of organic field-effect transistors (OFET) [10]. The degree of crystallinity can also influence the transparency resulting from the different refractive indexes in crystalline and amorphous regions. Therefore, it is necessary to understand the degree of crystallinity and how the crystalline regions are distributed in order to further push the limits of polymer applications. More fundamentally, comprehending the polymer crystallization will pave the way for understanding the intrinsic structure of protein due to their similar folding behaviors [2].

Based on the polymeric morphology and crystallizing process, there are three classical structure models: fringed micelle (two-phase) model, folded-chain model, and switchboard model as shown in **Figure 1.4**. (a) In the fringed micelle model, each chain meanders through crystalline and amorphous regions binding the whole mass together. (b) For polymeric single crystal, the folded-chain model is defined well because of no amorphous region there; however, it is not suitable for semi-crystalline polymers. (c) The third model provides a general explanation for the arrangement of long molecular chains, which must either reenter the crystal or go elsewhere. However, each model can only explain partial experiments and there is no explicit boundary between them.

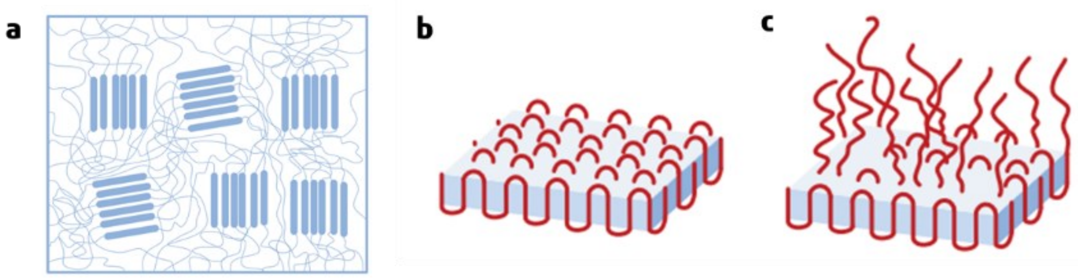

**Figure 1.4.** Schematic illustration of three classical structure models for polymers, (a) the fringed micelle model, (b) the folded-chain model, and (c) the switchboard model. (reproduced from [59])

### 1.2.2 Microscale ordering of polymer spherulites

As the crystals grow to a microscale, polymeric crystallizing products can form different morphology such as lamellae, spherulites, fibers, and shish kebab depending on factors such as the crystallization condition and the rigidity of polymer molecules [2,3,30]. Among these morphologies, spherulites are the most common and possess complex hierarchical structures which results in unique optical features, such as Maltese crosses and extinction bonds (see **Figure 1.6** and **Figure 1.7**). **Figure 1.5** shows a schematic illustration of the construction of spherulite thin film structure from crystal structure to macroscopic order by folded-chain lamellas. The curve and folding of long chain of monomers form the crystalline lamellae, and the myriad lamellae stack and splay into a spherulite. Despite being named spherulites, their structure can deviate from a perfect sphere. Especially at the surface limit, as observed in solution-cast thin films on silicon wafers through evaporative crystallization [11-13], spherulites with circular symmetry and thin thickness are formed.

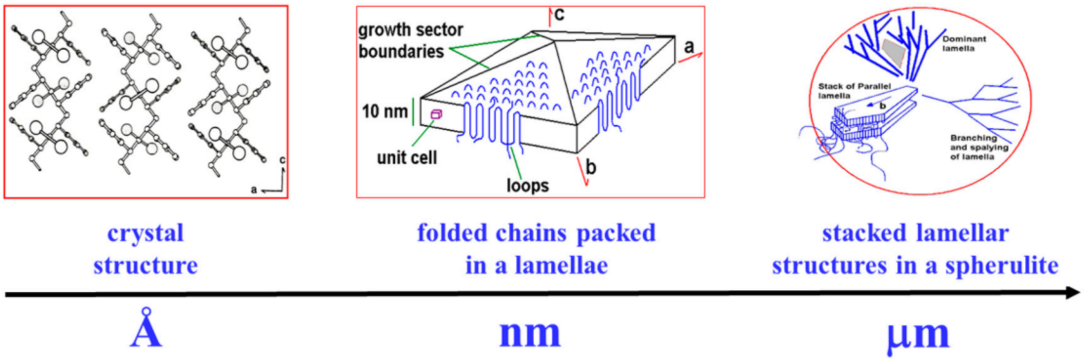

**Figure 1.5.** Schematic illustration of the construction of the microstructure of spherulites from crystal structure to macroscopic ordering spherulite thin film stacked by nanoscale folder-chain lamellae. (reproduced from [11])

Moreover, based on the underlying orientation and stacking mode of the lamellae, the organization of spherulite thin films can be mainly classified into six situations as shown in **Figure 1.7**. More spherulite morphologies can be formed by adjusting the processes and radial growth axis [12,14,15]. As a consequence, spherulite thin films can have a rather complex microscale structure.

In most spherulites, they have a banded Maltese cross pattern when observed under a polarized optical microscope (POM). The Maltese cross pattern is attributed to the fact that crystals within a spherulite all have a same crystallographic orientation radially pointing outside and circular symmetry around their cores. The schematic diagram in **Figure 1.6** demonstrates the origin. For the polymer spherulites illuminated by linear polarized light ($\boldsymbol{I_0}$) through the polarizer (P), $\boldsymbol{I_0}$ can be decomposed orthogonally into two orthometric linear polarized light with a phase difference, and their magnitude depends on the angle between $\boldsymbol{I_0}$ and polymer crystal axes. The emergent light is an elliptical polarized light, and when it subsequently passes through an analyzing polarizer (A), its component parallel to A is recorded with intensity as expressed in **Equation (1.2)**:

$$I_t = |\boldsymbol{I_0}| \sin^2 2\gamma \sin^2\left(\frac{\pi d}{\lambda}(n_b - n_a)\right) \tag{1.2}$$

where $\gamma$ is the azimuthal angle between $\boldsymbol{I_0}$ and crystal axis, d is the sample thickness (light path), and $\lambda$ is the wavelength of light. In the vertical and horizontal direction of spherulites, the emergent light is a linear polarized light (no decomposition) parallel to P and finally is blocked by the analyzing polarizer resulting in darkness in POM images. On the other hand, lamellae twist often occurs in the splay of spherulites and may expose indicatrix projections with equal refractive index. Therefore, there is a series of periodic extinction rings as shown in **Figure 1.6** and **Figure 1.7**. However, the exact growth direction and twisting axis is still unable to be derived from the POM results because the optical indicatrix in ab plane is almost circular and isotropy ($n_a$=1.514. $n_b$=1.519, $n_c$=1.575 for $C_{36}H_{74}$). Although, the growth direction is often indirectly determined by morphology or equivalent to the twisting axis, b axis in lamellae [3], the orientation relation in spherulites is still not established.

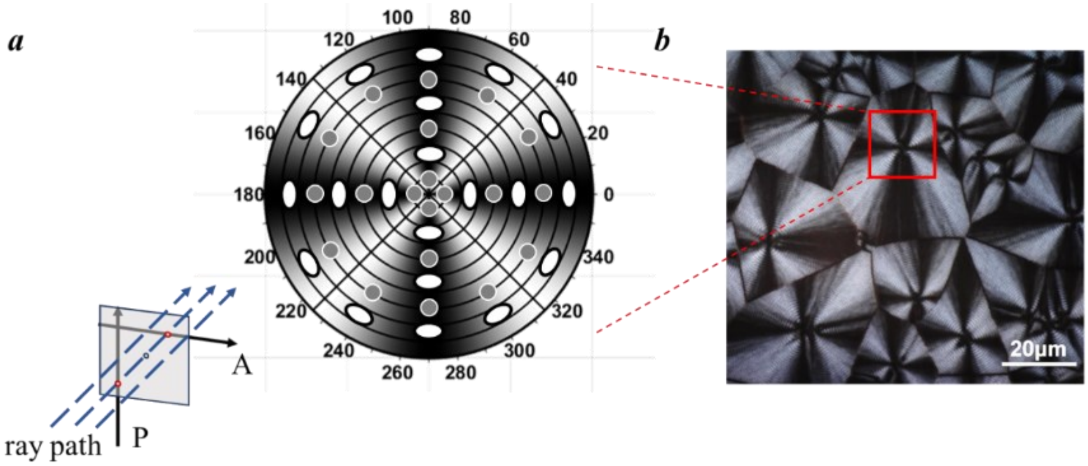

**Figure 1.6.** (a) Schematic diagram of the Maltese cross pattern and extinction banded pattern exhibited by birefringent spherulites. The ellipses and circles are the local indicatrix which respectively lead to a bright and dark contrast. (b) A POM image of PE spherulites, where each spherulite showing a banded Maltese cross pattern.

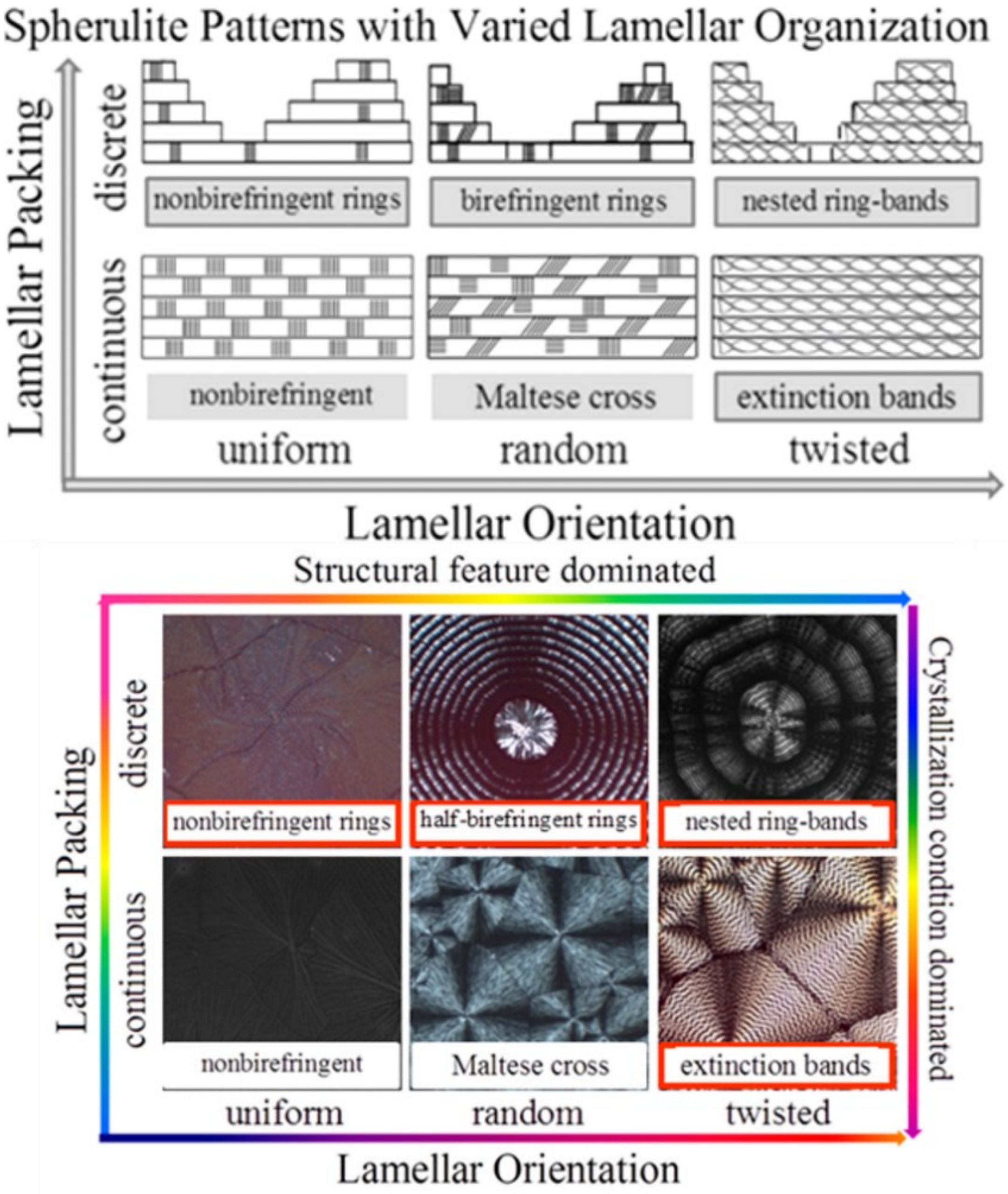

**Figure 1.7.** Schematic diagram of the main cross-sectional radial lamellar organization for polymer spherulite thin films, and the polarized light microscopy images for the six kinds of spherulite thin films. (reproduced from [12])

However, there is no effective characterization to directly reveal the structure of spherulites. Common techniques such as atomic force microscope (AFM), scanning electron microscope (SEM) are helpless to directly reveal the microstructures, while POM, Raman spectroscopy, and electron backscatter diffraction (EBSD) of SEM are resolution-limited (around one micrometer). Additionally, all these methods are hard to quantitatively map the crystallinity distribution in semi-crystalline polymeric spherulites. Thus, it is necessary to study the semi-crystalline polymeric spherulites by the 4D-STEM systems.

In Chapter 3, we aim to elucidate the microscale ordering in PE and PCL spherulites using our self-developed 4D-STEM technology. Due to the surface confinement, our spherulites are essentially local single crystal without grains stacking in thickness, which is also evidenced by the single-crystal-liked diffraction patterns (**Figure 3.2**). By analyzing 4D datasets of diffraction patterns, we determined local orientation based on characteristic diffraction directions and quantified local degree of crystallinity by utilizing intensity ratios between ordered and disordered diffraction signals. Our evidence-based orientation map and phase map of spherulites explicitly reveal different microstructures and inhomogeneous crystallinity in PE and PCL samples.

## 1.4 Quantitative plasmon for $In_2Se_3$ phase identification

For another dose-sensitive material, 2D $In_2Se_3$, it has emerged as a promising research area due to its superior electrical and optical performance as well as its reduced dimension. However, distinguishing the competing polymorphs of $In_2Se_3$ at the nanoscale for better performance is still challenging due to the subtle differences in crystal structure, dose-induced defects prone to occur once dose exceeds 30000 $e/Å^2$, and the advanced proficiency required in TEM. Thus, the conventional TEM/STEM imaging is inadequate in this case. A potential method is using the distinct plasmon energies in EEL spectra due to its high resolution, relatively low dose, and independence of orientation.

### 1.4.1 Phase mixture in $In_2Se_3$

Polymorphism in 2D materials forms an exciting research frontier for exploring new phases with exotic functionalities at reduced dimensionality and for manipulating these 2D functionalities through controlled phase switching for novel device applications. The most prominent examplea are 2D metal chalcogenides [60,61], in which the medium electronegativity of chalcogen elements (S, Se and Te) leads to competing ionic and covalent bonding, further giving rise to polymorphs with distinct bonding configurations [60]. This manifests as the well-known 2H, 3R, 1T and 1T′ phases in transition-metal dichalcogenides (TMDs) [62-65], and more recently as the $\alpha$ and $\beta'$ phases in 2D $In_2Se_3$.

Among the chalcogenide semiconductors in the $III_2$-$VI_3$ family, $In_2Se_3$ is polymorphic with many phases reported ($\alpha$', $\alpha$, $\beta$', $\beta$, $\gamma$, $\delta$, $\kappa$) [66-71]. The two room-temperature phases, $\alpha$- and $\beta'$-$In_2Se_3$, and the high-temperature $\beta$ phase have the 2D layered structure consisting of [Se-In-Se-In-Se] quintuple layers with several possible stacking orders (2H, 3R, 1T) [72-75]. Their structures are explicitly demonstrated by HAADF images and atomic models in **Figure 1.8**, including plane structures of $\alpha/\beta'$ phases, stacking structures of $\alpha 2H$, $\alpha 3R$, $\beta' 2H$, $\beta' 3R$ phases, and the coordination environment of $\alpha/\beta'$ phases. Within each quintuple layer, $\beta'$- and $\beta$-$In_2Se_3$ have all the

In atoms octahedrally coordinated by Se atoms, while $\alpha$-$In_2Se_3$ has only one layer of In atoms octahedrally coordinated and the other In layer with tetrahedral coordination [72,76,77].

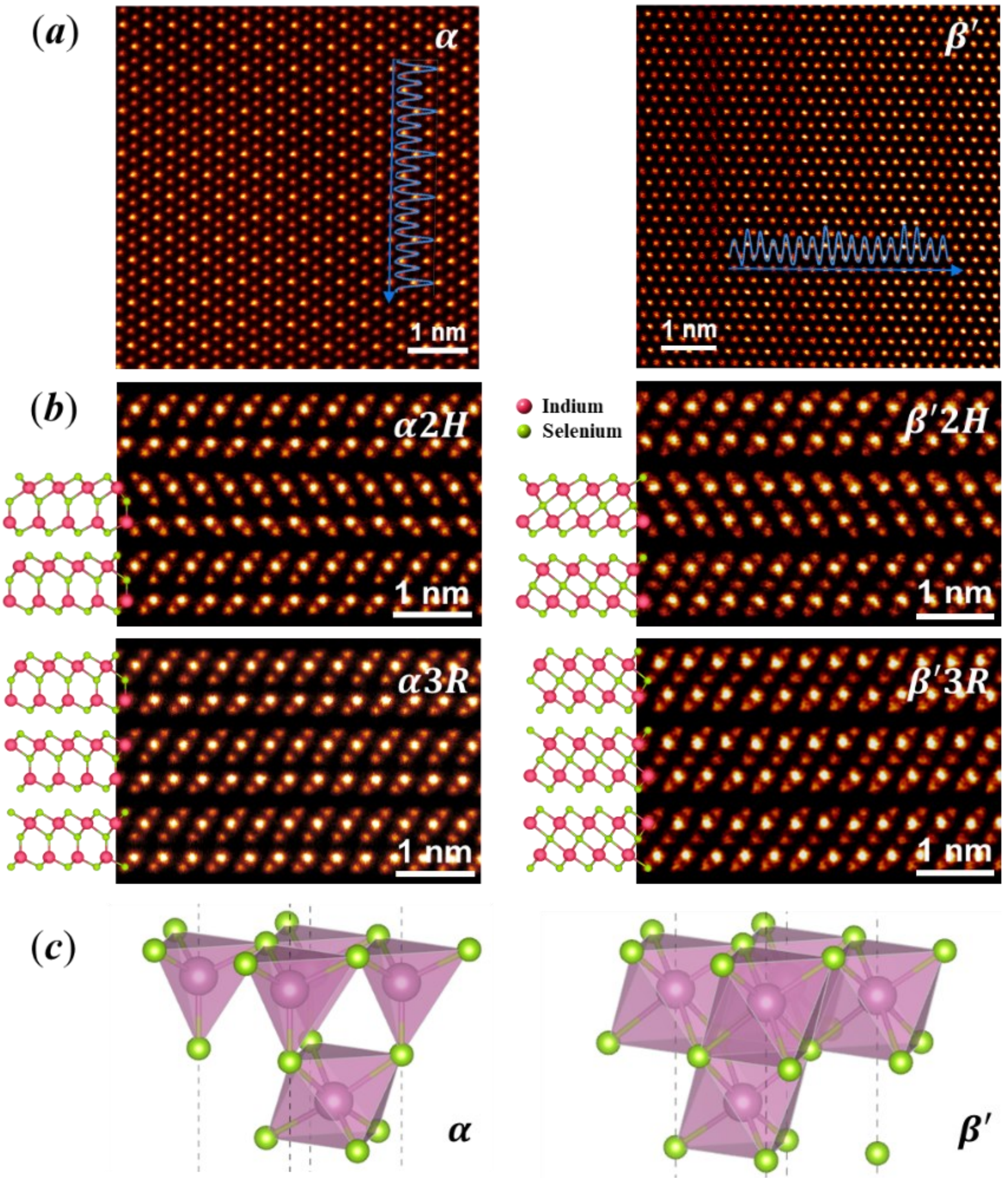

**Figure 1.8.** (a) HAADF images of multiple layer $\alpha/\beta'$ $In_2Se_3$ along <0001> zone axis. (b) Atomic models (red for Indium, green for Selenium) and HAADF images of four $In_2Se_3$ along <11$\bar{2}$0> zone axis. (c) The single-quintuple-layer 3D atom model of and coordination environments.

More excitingly, $\alpha$-$In_2Se_3$ exhibits 2D ferroelectricity that is currently under intensive investigation [71,78-83], while $\beta$'-$In_2Se_3$ possesses a 2D antiferroelectric superstructure that distinguishes it from the high-temperature paraelectric $\beta$ phase [86]. The rich polymorphism makes $In_2Se_3$ a fascinating system for exploring both the fundamental ferroelectric physics at the 2D limit and ultrathin electronic device applications [86-88], as some recent demonstration of optoelectronics, pyroelectricity, and ferroelectric field-effect transistors [89-91]. At the same time, phase changes between these phases can be induced by several approaches. For instance, temperature in the range of 220-290 °C can transform the $\alpha$-$In_2Se_3$ into $\beta$- $In_2Se_3$ [75,86], and a reversible phase transition of $\alpha \leftrightarrow \beta'$ is achieved through applying strain and electrical field [92,93]. These phase controllable strategies also pave paths for developing the phase-switch devices [79,80,82,83,91,93,94-96].

On the other hand, with similar stability of polymorphs, $In_2Se_3$ has been reported to possess intermixed phases on the nanometer level [72,93,97], as the example shown in **Figure 1.9**, making single-phase synthesis challenging. The phase mixture can not only deteriorate the theoretical performance of these devices but also hinder our understanding to its physical properties and devices mechanism.

Resolving the 2D polymorphs is thus of particular importance both for understanding the phase switching mechanism such as the nucleation of the second phase and for evaluating the purity of the samples. Conventional characterization such as X-ray diffraction (XRD) and Raman spectroscopy do not have sufficient resolution to detect nanoscale intergrowth of polymorphs. Atomic-resolution TEM/STEM can identify various polymorphs on the unit cell level but requires them to be on the zone axis which can be difficult to achieve for nanoscale second phases. Additionally, atomic-resolution TEM/STEM requires high electron dose which can induce obvious defects and structural damage for samples of intermixed phases once dose is over 30000 e/Å$^2$. The examples of interfacial defects are shown in **Figure 1.9c** and **Figure A.3(a-c)** with accumulating dose of ~48000 and ~32000 e/Å$^2$ respectively. A potential method is using the plasmon in EEL spectra.

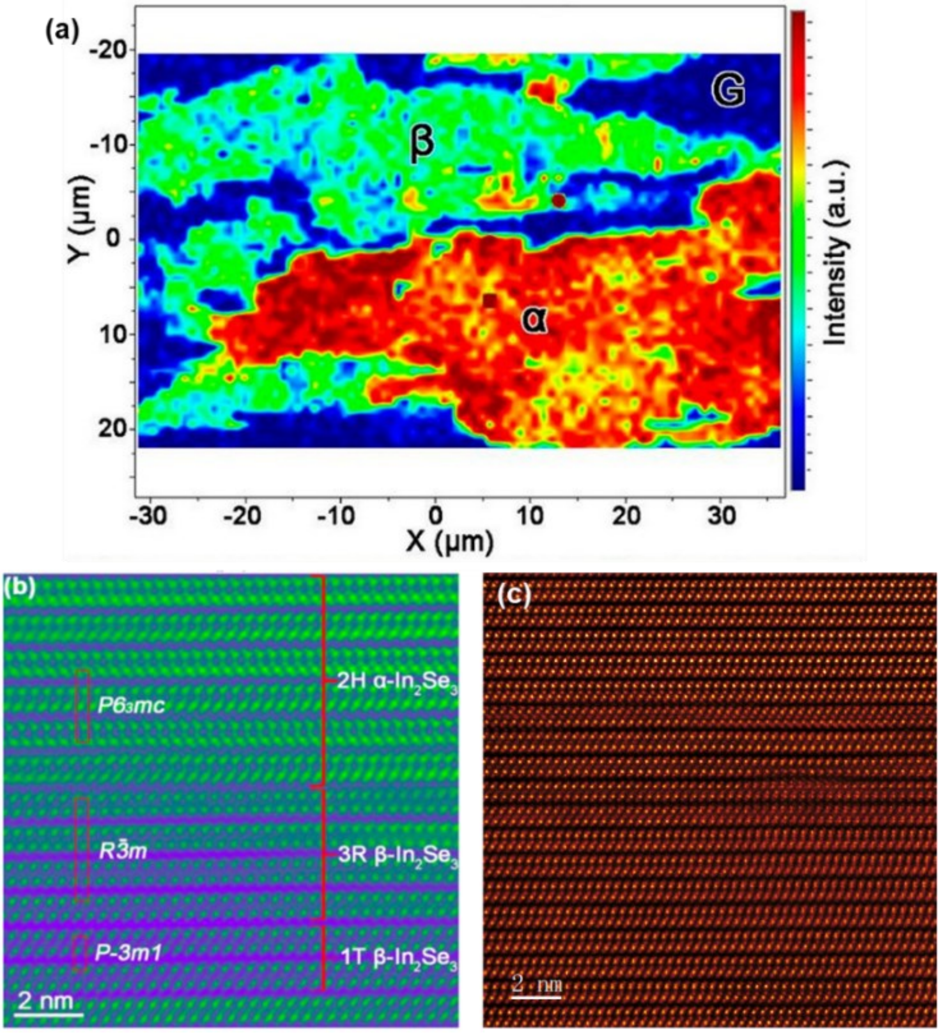

**Figure 1.9.** Phase mixture and interfacial defects of $In_2Se_3$. (a) Raman mapping of plane $\alpha$-$\beta$ mixed $In_2Se_3$. (b) HAADF image of $\alpha$-$\beta$ mixed $In_2Se_3$ in cross-section (c) HAADF image of interfacial defects in cross-sectional intergrowing $In_2Se_3$ with an acquiring dose of ~48000 e/Å$^2$. ((a), (b) reproduced from [72])

### 1.4.2 Plasmon in EELS

A plasmon is a quantum of plasma oscillation (also known as plasma resonance) and is a collective electron oscillation that occurs when a beam electron interacts with the weakly bound electrons. The plasmon signal usually occurs in various metal and non-metal materials, even where no evident free electrons, and is the strongest signal except the zero-loss peak (ZLP), which make the spectrum relatively featureless due to its high intensity, as shown in the example of EEL spectrum of $\alpha 3R$ $In_2Se_3$ in **Figure 1.10**.

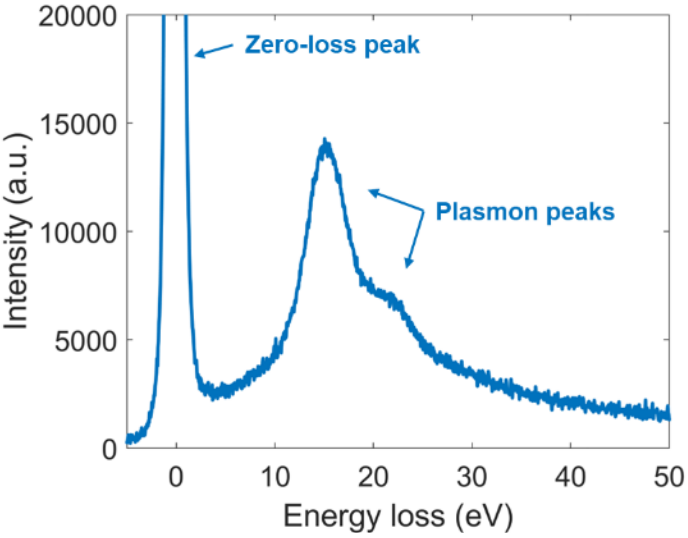

**Figure 1.10.** EEL spectrum of $\alpha 3R$ $In_2Se_3$ in the energy range of -5 to 50 eV, only showing the zero-loss peak and two plasmon peaks.

For a long time, plasmon signals are used as a chemical fingerprinting based on differences in their shapes with some degree of statistical certainty [29]. However, differences in the sample preparation and experimental parameters could lead to a slight change in the shapes and position which thus require much experience for accurate chemical fingerprinting. Moreover, the plasmon as a pseudoparticle have a known energy $E_p$ following the **Equation (1.3)** [29,98]:

$$E_p(T) = \hbar\sqrt{\frac{n(T)e^2}{\epsilon_0 m_{eff}}} = \hbar\sqrt{\frac{n_0}{V(T)}\frac{e^2}{\epsilon_0 m_{eff}}} \qquad (1.3)$$

where $\hbar$ is reduced Plank constant, $e$ is the electron charge, $m_{eff}$ is the effective mass of electrons, $\epsilon_0$ is the vacuum permittivity, and *n(T)* is the valence electrons density equaling the valence electrons over the volume $n_0/V(T)$. Based on the negative correlation between $E_p$ and volume *V(T)*, the plasmon signal can be used to measure the local volume change induced by stress or thermal gradient, and thus the temperature can be derived by the relation between volume and temperature as a thermometer for nanoscale [99-103].

However, using plasmon to distinguish between polymorphs is rare. One reason is that the differences between polymorphs in terms of crystal structure and atom arrangement are often subtle, requiring quantitative analysis and sensitive detection methods. Additionally, unknown disturbances during multiple measurements can negatively impact the precision of measurements, necessitating meticulous experimental preparation and in-situ observations to mitigate their effects. As a result, despite its strong signal, the application of plasmon is limited for phase identification.

### 1.4.3 Quantitative Plasmon for phase identification of $In_2Se_3$

As stated in previous chapters, there is an urgent need for effectively identify and locate the phases of $In_2Se_3$. Commonly used techniques like Raman spectroscopy (see **Figure 1.9a**) and XRD are limited in spacing resolution. TEM/STEM imaging can distinguish the $\beta'$ phase from $\alpha/\beta$ phases on the <0001> zone axis by its superstructure [86] or by the intensities of atomic columns [93] as shown in **Figure 1.8a** which has been used to identify the large-area mixture of $\alpha$ and $\beta'$ [93]. Moreover, the differences in stacking structures along <$11\bar{2}0$> zone axes can directly reveal the phases as shown in **Figure 1.8b,** where atomic distortions occur in the quintuple layers and stacking order is obvious on multiple-layer samples. However, TEM/STEM for unambiguously imaging the atomic structure requires not only high dose (> $10^4$ e/Å$^2$) which can induce surface/interface defects but also reasonable orientation which may not be achievable especially for nanoscale intergrowth of second phases.

In contrast, valence EELS (VEELS), which mainly involves the plasmon signal, offers several advantages for local phase identification. These include high resolution, a broad field of view (ranging from nanoscale to microscale), low-dose acquisition (8000 e/Å$^2$ is sufficient), and independence of orientation. In VEEL spectra, the shape of the plasmon signal contains information about the dielectric function of the samples, primarily originating from the material's composition and structure. However, in the case of 2D $In_2Se_3$ polymorphs, the plasmon shapes are very similar, making it difficult to differentiate them based solely on shape analysis. Therefore, it becomes necessary to quantify the plasmon energies, which can provide information about the local volumes and the equivalent valence electron density n(T). Furthermore, considering the small difference in unit cell volumes between $\alpha$ and $\beta/\beta'$ phases, it is theoretically predicted that a plasmon difference exists between $\alpha$ and $\beta/\beta'$, based on **Equation** (1.3).

In Chapter 4, we performed the measurements of Raman spectra, XRD, and EELS to determine the phases, unite cell volumes, and plasmon energy positions, with careful cleaning process to minimize the effect of contamination. Moreover, *in situ* XRD and *in situ* EELS experiments explicitly reveal the differences in volume and plasmon energy position among these phases, thus further exploring the underlying reason, a subtle distinction in single-quintuple-layer valence electrons. More importantly, EELS maps covering the $\alpha/\beta'$ $In_2Se_3$ on the cross-section and 2D plane clearly present the distribution of phases identical to the acquiring HAADF images. Thus, plasmon-energy mapping emerges as an effective technique with relative independence of sample orientation for phase identification, particularly for materials containing nanoscale phase mixtures.

## 1.5 Thesis Outline

Chapter 2 of this thesis focuses on the degradation of polymer spherulites under the illumination of electron beam by quantitative diffraction and EELS, while Chapter 3 examines the microstructure of polymer spherulites using low-dose 4D-STEM. Finally, Chapter 4 discusses the phase identification of $In_2Se_3$ by quantifying plasmon energies.

In Chapter 2, the quantitative methods for electron diffraction and EELS reveal detailed beam effects in PE, PCL, and P3HT spherulites at room temperature and cryogenic condition, including both structure and chemical bonding evolution. Moreover, quantification of crystalline and amorphous components clearly identifies different effects of surface sputtering from the knock-on effect and amorphization from radiolysis, and provides evidence that both effects can be suppressed effectively by low temperature. The effects of amorphization and surface sputtering on PE and PCL are respectively dominant in the initial stage and subsequent stage. On the other hand, P3HT exhibits an intriguing two-stage damage process with side-chain ordering destroyed prior to π-stacking ordering at cryogenic conditions, which is caused by the fully suppressed amorphization.

In Chapter 3, we resolve the microscale ordering in PE and PCL spherulites using our self-developed 4D-STEM technology with advantages such as high resolution, the ability to quantify diffraction information, and low dose. The structure of spherulites was elucidated by evidence-based orientation maps, including growth fronts, rotation axis and how they are composed of lamellae. Additionally, the map of degree of crystallinity further present distinct spherulite structures on PE and PCL, deepening the understanding of spherulite formation mechanism.

In Chapter 4 of our study, we present the methodology and implications of quantifying the plasmon signal in the phase identification of $In_2Se_3$ polymorphs. We investigate underlying reasons for observed plasmon energy differences through *in situ* EELS and *in situ* XRD experiments. The results are in agreement with first-principles calculations, providing a new perspective on the phase change phenomena for similar 2D transition metal chalcogenides.

# Chapter 2 Quantitative beam degradation of PE, PCL, and P3HT

## 2.1 Introduction

The TEM identification of nanoscale structures and phases in polymers is hindered by the sensitivity of polymers to electron doses, thereby presenting a challenge for further optimization of polymeric performance. In this chapter, we present a comprehensive quantitative analysis of electron degradation in three polymeric spherulite films (PE, PCL, and P3HT) by using diffraction patterns and EEL spectra for optimizing electron probe and minimizing artifacts. This understanding also paves the way for studying the hierarchical structure of polymer spherulites in Chapter 3. To quantitatively reveal the structure and phase evolution under the influence of a calibrated electron dose, we adopt the established low-dose technique of selected area electron diffraction (SAED) and utilize curve modeling to analyze both crystalline and amorphous components. This contrasts with previous studies that considered only the crystalline components and ignored the amorphous parts [40], or treated them as a single entity [34-35,39]. Moreover, we use EELS to probe changes in chemical bonding, which further helps to elucidate the underlying damage mechanism induced by electron exposure. The measurements are conducted at both room temperature and cryogenic temperature (~98K), enabling a comparison that clearly demonstrates the effectiveness of cryo-protection in preventing beam effects on the studied polymers.

## 2.2 Methods

### 2.2.1 Materials

PE (Mw ~ 110 kg/mol, 20 mg, density ~ 0.95 g/cm$^2$, from Alfa Aesar) was initially dissolved in 1 ml decalin (from Sigma-Aldrich) at 180 °C for 3 h to ensure complete dissolution. Then PE films were spin-coated on silicon wafers with 300 nm $SiO_2$ on the surface, at 4000 rpm for 60 s. All the items used in spin coating including the solution, wafer substrates, glass droppers, and the spin-coating disks were pre-heated at 180 °C for at least 5 min to prevent uncontrollable rapid crystallization. PCL (80 mg, Mw ~ 14 kg/mol, Mn ~ 10 kg/mol, from Sigma-Aldrich) was dissolved in 1 ml m-xylene (from TCI) at RT for 1 h and subsequently spin-coated on wafers at 4000 rpm for 30 s. P3HT (6 mg, Mw ~ 58 kg/mol, regioregularity > 90%, from Rieke Metals Inc.) was dissolved in 1 ml toluene (from Ourchem) at 80 °C for 4 h and then spin-coated on wafers at 4000 rpm for 60 s. In order to increase the crystallinity of P3HT thin film, it was annealed under $CS_2$ vapor at 40 °C.

All three thin films were transferred onto TEM grids: thin films with underlying wafers were immersed in hydrofluoric acid aqueous solution to etch the $SiO_2$ interlayers away. Owing to the chemical inertness between common polymers and hydrofluoric acid, the thin films can keep their raw condition. Thin films floating on the solution surface were then picked up by TEM grids.

The thin films of three polymers are flat with a thickness ~150 nm (PE), 200 nm (PCL), and 15 nm (P3HT) respectively measured by a profilometer (DEKTAX TX, BRUKER). The optical images shown in **Figure 2.1a, c** demonstrate the flat periphery of single spherulite thin film, convex nuclei, and obvious domain boundary. Furthermore, these films all show obvious Maltese crosses in polarized optical microscopy which usually represents a spherulite structure, see **Figure 2.1b, d, e, and Figure 1.6a**. Notably, the polarized optical image of PE in **Figure 1.6a** shows obvious Maltese crosses and textures of extinction bands same as the typical extinction bands shown in **Figure 1.5** which is caused by the lamellae twist and is discussed in Chapter 3.

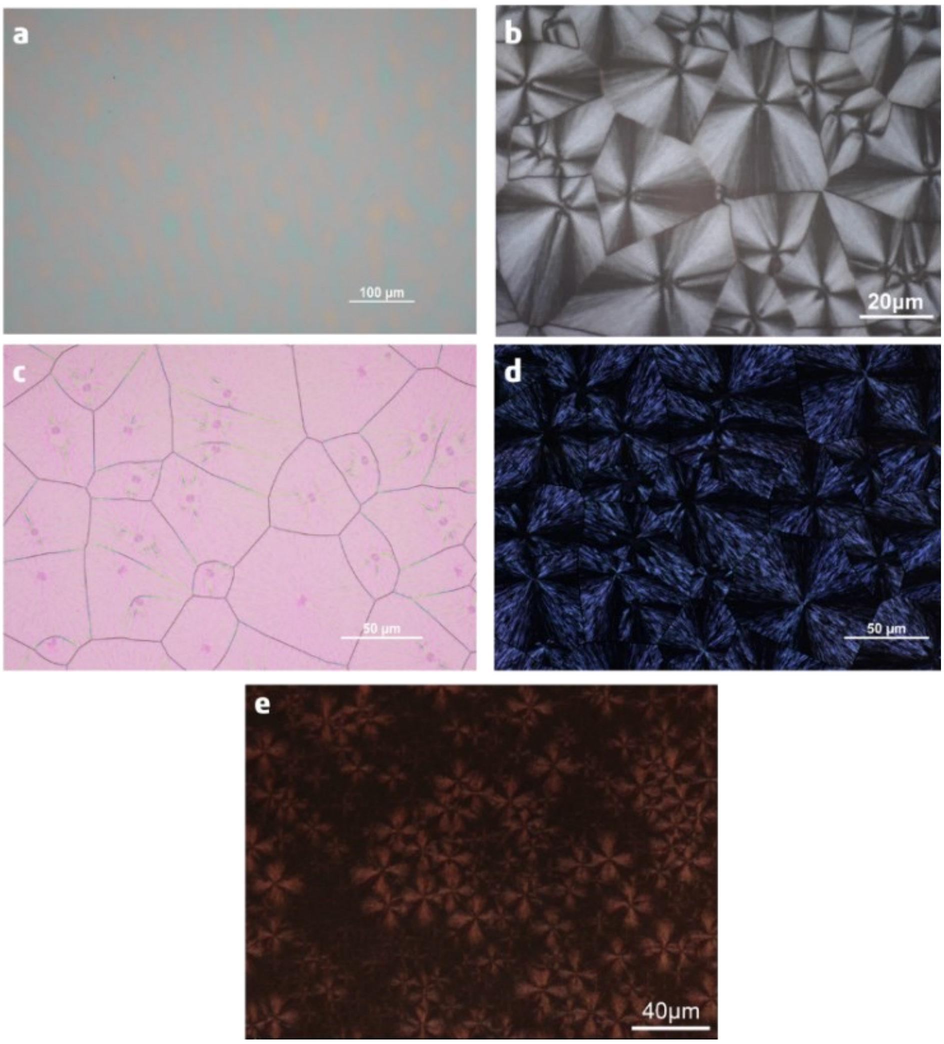

**Figure 2.1.** (a, c) Optical microscopy images of PE and PCL thin films and (b, d, e) polarized optical microscopy images of PE, PCL, and P3HT thin films.

### 2.2.2 TEM Operation

Time-series SAED patterns were performed on a JEOL JEM-2100F microscope operated at 200 kV. In TEM mode, the electron beam (beam current ~2.2 nA) was fully spread at 2K magnification, with an irradiation diameter ~12μm to achieve a low-dose condition with a moderate dose rate ~1.2 e/(Å$^2$·s). The exposure time for each selected area electron diffraction (SAED) pattern was 0.3 s, and acquisition intervals were 0.7 s for PE and P3HT, and 0.3-1.2 s for PCL, and the recording camera was Gatan Orius SC 1000A. Considering the way to acquire diffraction image and testing delay, the first frame has been irradiation, so we set the dose as half of the dose difference between contiguous frames. For cryogenic observation, the polymer samples were loaded into a liquid-nitrogen cooling holder (Gatan, model 636) to lower temperature down to 98 K. The system was stabilized for over 40 min after filling the liquid nitrogen, in order to minimize vibration caused by liquid nitrogen evaporation.

Time-series EELS was carried out using a Gatan Enfina spectrometer with the energy dispersion of 0.05 eV/channel in STEM mode, with the 13 mrad convergence angle and 21 mrad collection angle. In this mode, typical electron beam parameters are like below: the beam current ~ 28.5pA, dwell time 2 μs, scanning pixels 256*256, frame size ~62.7 nm.

During the measurement, we used an irradiation area of over 450 μm$^2$, which not only decreases the dose rate to the unit area but also ensures a high thermal conductivity, due to the short distance to the copper grid (the size of holes is ~ 40 μm), to minimize the potential heating effect of the electron beam on the samples. Based on our estimates, the temperature rise is only a few K for all three polymers, and the detailed derivation is discussed in **Appendix A.1**. Furthermore, the heating expansion has very limited effects on the shifts of diffraction positions compared to those caused by electron beam damage, due to the small thermal expansion coefficient. This can be roughly observed by the pristine diffraction position at room temperature and cryogenic temperature (98 K).

### 2.2.3 Curve Fitting

Typical SAED patterns like the images taken from a PE film in **Figure 2.2a**. The pristine diffraction pattern (electron dose of 0.6 e/$Å^2$) shows sharp arcs corresponding to 110, 200 and 020 diffraction instead of points which results from polycrystalline structure. However, it is hard to intuitively distinguish the relative position in time-series diffraction patterns. Thus, we primarily transfer the 2D diffraction patterns into 1D spectra based on a MATLAB script that transform Cartesian coordinates to polar coordinates and collapse the angle dimension. Consequently, we obtain the radial-averaged intensity profiles of diffraction patterns, and two examples of profiles under electron dose of 0.6 and 8.0 e/$Å^2$ within limited reciprocal range (1.5 to 3.2 $nm^{-1}$) is shown in **Figure 2.2b, c.**

To further analyze the structure evolutions in time-series diffraction patterns, we model the curves by using least-squares fitting [39]. As illustrated in **Figure 2.2b, c**, by subtracting a power-law background and a constant for residual dark counts, the remaining diffraction signals can be adequately fitted with three Gaussians ($R^2 \geq 99.5\%$): two for 110 and 200 diffraction and one for the signal from the amorphous phase. The total diffraction intensity can be described by the **Equation (2.1)**.

$$I = a_1 e^{-\frac{(x-b_1)^2}{2{c_1}^2}} + a_2 e^{-\frac{(x-b_2)^2}{2{c_2}^2}} + a_3 e^{-\frac{(x-b_3)^2}{2{c_3}^2}} + dx^{-\gamma} + e \qquad (2.1)$$

Besides the peak position indicated by $b_i$, intensity of each diffraction peak can also be derived from the area of the fitted Gaussian, which reflects the corresponding ordering for crystalline peaks or disordering for the amorphous peaks. As 110 and 200 are the dominating diffraction peaks, we take the sum of two peak intensity $I_{110}$ and $I_{200}$ as the total crystal diffraction intensity $I_{cryst}$ without considering other minor diffraction such as 020. Then the sum of $I_{cryst}$ and $I_{amorphous}$ is just the total background-subtracted intensity in **Equation (2.1)**.

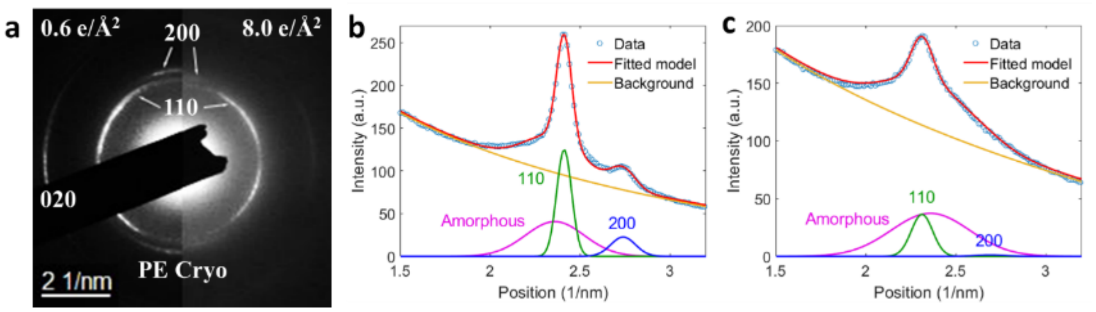

**Figure 2.2.** (a) SAED patterns on the same PE film at 98 K (cryo) with the dose 0.6 (left) and 8.0 (right) e/Å$^2$, respectively. (b, c) Intensity profiles from radial averaging on SAED patterns in (a), with the dose (b) 0.6 and (c) 8.0 e/Å$^2$, respectively. Gaussian fitting is used to measure quantitatively the position and intensity changes of 110 (green) and 200 (blue) diffraction, as well as the amorphous peak (magenta).

## 2.3 Degradation of PE under electron beam

PE as one of the most widely used polymer have a simple crystal structure due to no side chain, see **Figure 2.5h**, and thus have a comprehensible diffraction pattern composed mainly by the {110}, {200}, and {020} diffraction arcs, see **Figure 2.2a**. Thus, we firstly take PE as the example to illustrate the degradation process under electron beam, and then discuss PCL and P3HT.

### 2.3.1 Changes in PE diffraction patterns

The fragility of PE spherulites at RT when subjected to high-energy electron beams is evidenced by the after-exposure image in **Figure 2.2a** right half: with the accumulation of a mere 8 e/Å$^2$ dose, the {110} diffraction ring becomes fainter and diffused, while the 200 diffraction becomes nearly invisible, indicating a decline in lattice ordering upon exposure. Furthermore, diffraction rings also show reduced radii compared to the pristine diffraction pattern, suggesting an increase in lattice spacing caused by the electron beam. By employing the method introduced in Chapter 2.2.3, the changes in amorphous and crystalline components and the positional change of three main diffraction families are revealed.

**Figure 2.3a-c** depict the variations of $I_{cryst}$ and $I_{amorphous}$ of PE spherulites with increasing electron dose. Electron exposure causes a monotonic decrease in both $I_{cryst}$ and $I_{amorphous}$ at both RT (red symbols) and 98 K (blue symbols). Initially, the decrease in $I_{cryst}$ is fast and subsequently becomes slower until zero intensity (**Figure 2.3b**). Results from least-squares curve fitting on the measured intensity indicate that the variations of $I_{cryst}$ are well-described by exponential decay. In contrast, $I_{amorphous}$ exhibits an initial rise followed by a linear intensity drop at both temperatures (**Figure 2.3c**).

The initial rise in $I_{amorphous}$ coincides with the fast decay of $I_{cryst}$, reflecting the radiolysis effect - PE amorphization is a well-known consequence of electron beam exposure [27,42].

**Table 1.** The critical doses of crystalline components in e/Å$^2$, and their 95% confidence intervals of PE, PCL, and P3HT at RT and 98 K derived from the exponential decay of $I_{cryst}$. The / is for no record.

| Condition | PE | PCL | P3HT |
|---|---|---|---|
| RT | 1.1 (0.5-1.6) | 1.9 (1.1-2.7) | 7.5 (7.0-8.0) |
| Reported @ RT | 2-6[28] | / | 8-36[22.26.29] |
| 98 K | 9.2 (8.6-9.9) | 19.8 (18.2-21.3) | 16.3 (14.5-18.0) |
| Reported @ Cryo | 6.7-8.2[23] | / | 90-188[22,26] |

On the other hand, surface sputtering from the knock-on damage of the electron beam could also contribute to the decrease of $I_{cryst}$. To quantitatively evaluate the crystal radiation sensitivity, the critical dose $D_c$ is introduced. In this thesis, it is the accumulated dose at which the normalized $I_{cryst}$ drops to *1/e* (~37%) as that reported [1,27,28,44]. Results show that the $D_c$ are about 9.3 e/Å$^2$ at 98 K but only about 1.1 e/Å$^2$ at RT, and the $D_c$ of three polymers are listed in **Table 1**, which are comparable to previous reports [34,35,39,40,65,105]. The very low critical dose at RT also indicates the necessity of cryo-protection to achieve reliable structure information from pristine PE samples.

It is important to note that the concept of critical dose only describes the dependence of beam effects on the accumulated electron dose without considering the dose rate effect [1,27]. In experimental studies on similar polymer films [39,40,106,107], the dose rate effect was found to cause only a minor effect. However, in this thesis, our dose rate of approximately 1.2 e/(Å$^2$·s) is moderate and recommended for revealing the degradation process at cryogenic conditions. Therefore, we have not included any details about the effect of dose rate on the degradation of polymers.

The amorphous component of PE is observed to be relatively more stable than the crystalline component. The intensity of $I_{amorphous}$ begins to decrease appreciably only when $I_{cryst}$ approaches zero. Consequently, the diffraction patterns of PE become dominated by the amorphous halo at the late stage of beam exposure, as shown in the inset of **Figure 2.3c**. The linear decrease of $I_{amorphous}$ at this stage further supports the notion that surface sputtering is the predominant damage process. It has been reported that radiolysis beam effects, such as amorphization, generally lead to the exponential decay of $I_{cryst}$, whereas surface sputtering causes the linear decay [1,27], which suggests that the different decay behavior between $I_{cryst}$ (exponential) and $I_{amorphous}$ (linear) is rationalized.

The fitted slopes of $I_{amorphous}$ demonstrate that the intensity drop is slowed down by approximately 7 times when lowering the temperature from RT to 98 K, similar to the reduction rate of the critical dose measured from $I_{cryst}$. This finding implies that cryo-protection is equally effective in prohibiting surface sputtering on PE in addition to the above-mentioned radiolysis effect.

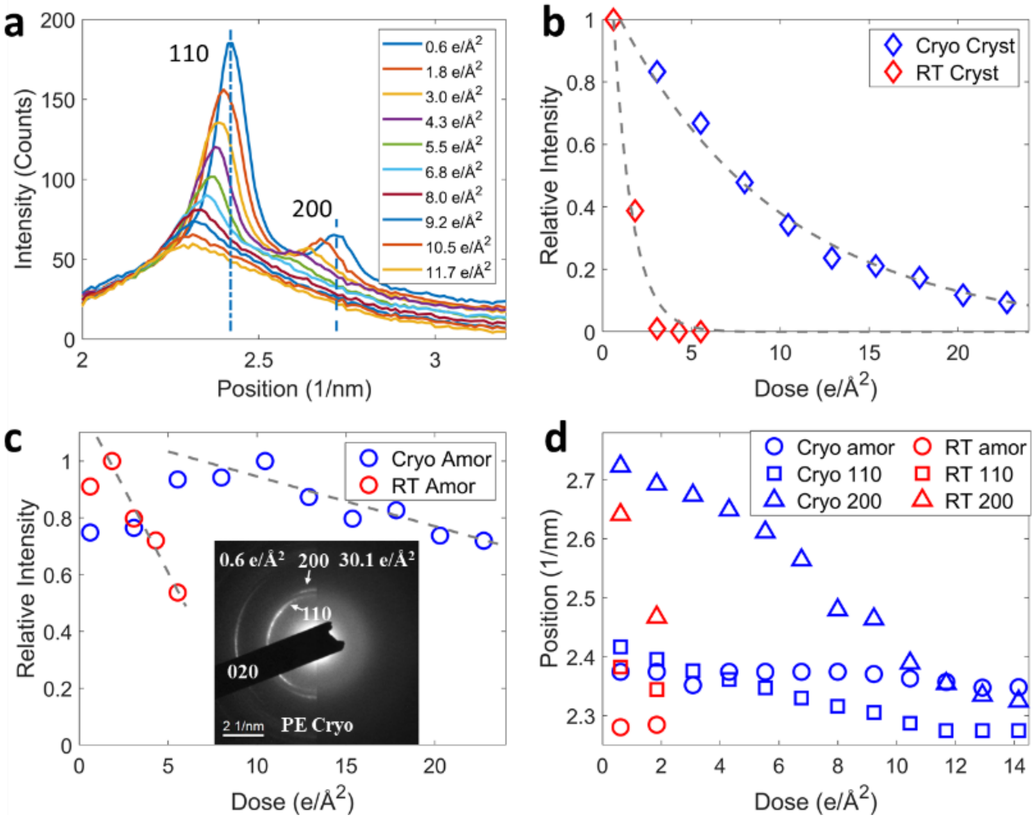

**Figure 2.3.** (a) Radial-averaged intensity profiles of SAED patterns from PE at 98K with varying electron doses. Profiles are shifted vertically with an incremental value for clear visualization. (b, c) Relative intensity of (b) $I_{cryst}$, and (c) $I_{amorphous}$ as functions of accumulated electron dose for PE at 98 K (blue) and RT (red), respectively. The exponential and linear decay is indicated by the fitted dashed lines. The intensity is determined from the area of the fitted Gaussians on radial-averaged diffraction peaks, normalized by the maximal intensity of the entire series. Inset in (c) shows SAED patterns on the same PE film at 98 K (cryo) with the dose 0.6 (left) and 30.1 (right) e/Å$^2$ respectively, demonstrating the amorphization process. (d) Peak positions of PE 110 (square), 200 (triangle), and amorphous (circle) diffraction with increasing electron dose, at 98 K (blue) and RT (red), respectively. Error bars smaller than the size of marks are not shown.

Besides intensity variation, we also analyze the change of diffraction peak positions observed in **Figure 2.2a** and **2.3a**, which reflects lattice spacing variations upon the beam exposure. As plotted in **Figure 2.3d**, the 110 diffraction peak shifts linearly from 2.42 nm$^{-1}$ to 2.27 nm$^{-1}$ at 98 K after accumulating 14.1 e/Å$^2$ electron dose, corresponding to the increase of lattice spacing $d_{110}$ from 4.13 Å to 4.41 Å, ~6.6%

expansion. Meanwhile, the 200 diffraction peak exhibits even more dramatic shifts from 2.72 $nm^{-1}$ to 2.37 $nm^{-1}$, equivalent to a ~14.7% expansion from 3.68 Å to 4.22 Å. However, due to its quicker intensity drop, the fitting on 200 diffraction eventually merges into the amorphous peak (**Figure 2.3d**), and after 14.8 e/$Å^2$, the intensity of 200 diffraction is set to zero. Meanwhile, the amorphous diffraction peak shows negligible shift during the same observation, indicating that the expansion is for the crystal lattice only and thus should not be caused by heating from the electron beam. Indeed, after raising the temperature by 200 K to RT, both 200 and 110 diffraction peaks shift only slightly as shown in **Figure 2.3d** (red triangles and squares), which cannot account for the observed large expansion at 98 K and further exclude the effect of beam heating. RT measurement on peak position variations also displays the same trends, only with fewer data points due to much faster intensity decay. We note that lattice expansion from beam effects has been reported in PE and attributed to radiolysis damage and the subsequent crosslinking between polymer chains [40]. Indeed, the detected lattice expansion in **Figure 2.3d** coincides with the increase of $I_{amorphous}$ in terms of accumulated dose and thus the amorphization process from radiolysis. On the other hand, our study suggests a different radiolysis mechanism from the crosslinking model in Ref 40, as will be discussed in detail below.

### 2.3.2 Changes in PE EEL spectra

Besides diffraction-based structural analysis, further insights can be gained by examining the change in chemical bonding using EELS (electron energy-loss spectroscopy). As depicted in **Figure 2.4a**, the characteristic energy-loss signal from PE is typically observed in the range of 8-11 eV [108]. The red spectrum represents the pristine PE signal, with an intensity of ~30 e/Å$^2$. With the prolonged beam exposure, the PE signal decreases (blue spectrum), indicating the loss of PE material.

Interestingly, electron beam exposure also leads to an increase in intensity within 3-7 eV, consistent with previous studies on radiation damage to PE using EELS and optical absorption spectroscopy [43,108,109]. This signal is ascribed to the formation of polyenyl groups: Due to the stronger polarity of C-H bonds in comparison to covalent C-C bonds, C-H bonds are more susceptible to breaking under the beam radiation effect. This C-H bond scission results in the generation of alkyl radicals (**Figure 2.5a**) that can migrate along the polymer chain via hydrogen hopping [110-112]. When two alkyl radicals encounter each other, they can combine to form unsaturated bonds (**Figure 2.5b**). This process can generate various polyenyl groups, such as dienyl and trienyl chromophores [113], as illustrated in **Figure** 2.**5b-f**.

These polyenyl groups exhibit characteristic energy-loss signals in the 3-7 eV range [43], as indicated by the number of unsaturated bonds in **Figure 2.4a**. They are responsible for the observed increase in signal intensity in beam-exposed PE. Quantitative curve fitting analysis in **Figure 2.4c** further confirms that both the decrease in PE signal and the increase in chromophore signal follow an exponential trend, confirming their origin as a result of the radiolysis from the electron beam effect [1,27].

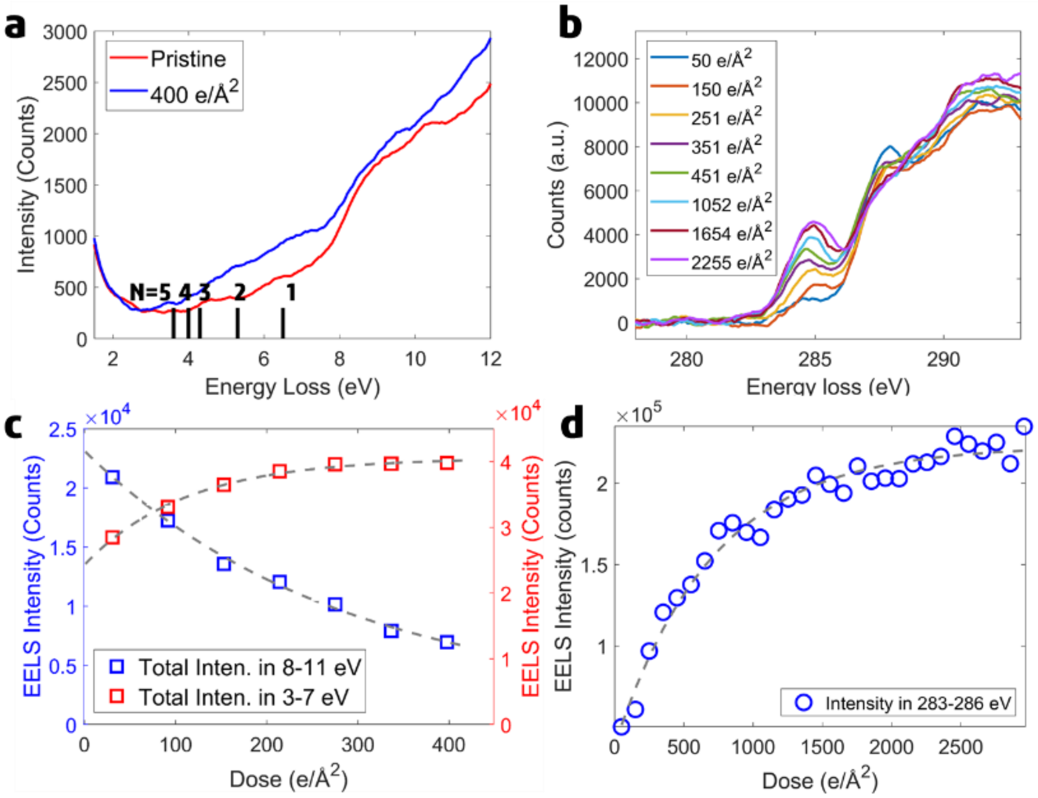

**Figure 2.4.** (a) Comparison of low loss EEL spectra from PE before and after beam exposure at 98 K. The vertical black lines indicate the energy loss associated with polyenyl groups containing *N* unsaturated bonds. (b) The core loss EEL spectra of PE at the carbon K-edge under different beam irradiation with dose rate 100.2 e/Å$^2$. (c) Decrease of PE signal in 8-11 eV (blue) and increase of polyenyl groups signal in 3-7 eV (red) calculated from the data in (a), both following the exponential functions. (d) The intensity from 283-286 eV in (b) with accumulated electron dose, following an exponential increase as the fitted dashed lines. Error bars smaller than the size of marks are not shown.

Furthermore, the core loss spectrums of PE under different beam irradiation, as shown in **Figure 2.4b**, also support these conclusions. The signal at 285 eV is attribute to a 1s-$\pi^*$ (C=C) transition [42,44,45], which is absent in the pristine PE spectra, while its intensity from in the range of 283-286 eV increases exponentially with the accumulation of electron dose, confirming an increase in unsaturated bonds (**Figure 2.4d**). The second peak/shoulder at 287.5 eV, related to the C-H bond, decreases in intensity and broadens, indicating the destruction of the pristine -$CH_2$- backbone.

It is important to note that the EELS measurements in this study were performed in scanning TEM mode, which differs significantly from continuous illumination for SAED. The ZLP is basically constant even dose accumulated to 200 e/Å$^2$. Due to the longer relaxation time between beam illuminations at the same spot (approximately 0.15 seconds), the scanning mode used for EELS may provide better sample stability compared to continuous illumination for SAED, thus leading to a higher critical dose. Thus, the effect of sample sputtering on EELS analysis in STEM mode can be excluded.

The radiolysis process, involving bond scission and the formation of short chains and groups, can also lead to the amorphization observed in SAED. The identified C-H bond scission and subsequent generation of polyenyl groups provide a plausible explanation for the observed lattice expansion in beam-exposed PE.: As illustrated in **Figure 2.5g**, the formation of unsaturated C=C bonds requires adjacent C-H bonds to rotate (e.g., from $H_{1,2}$ to $H_5$ in **Figure 2.5g**) towards the direction close to the {110} normal in the PE structure (**Figure 2.5h**). This rotation increases the distance (from $D_1$ to $D_2$) between the two ending hydrogen atoms $H_5$ and $H_6$. Increasing the number of C=C bonds through radiolysis will lead to the creation of more protruding hydrogen atoms, causing swelling of the polymer chains along the {110} and {200} normal. This, in turn, pushes apart the neighboring PE chains, resulting in the expanded $d_{110}$ observed in the PE structure (**Figure 2.3d**). The trans-polybutadiene crystal, which contains one C=C bond in the repeating unit (-$CH_2$-CH=CH-$CH_2$-), indeed exhibits a larger interchain spacing (4.56-4.60 Å) [114,115] compared to pristine PE without C=C bonds (~4.4 Å) [116,117], thus supporting the proposed mechanism for the observed lattice expansion.

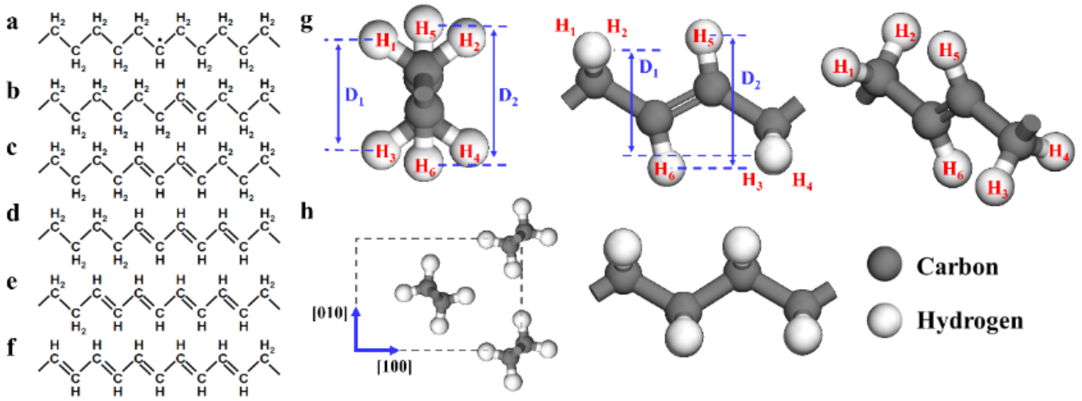

**Figure 2.5.** (a-f) Schematic drawing of the (a) alkyl radical and (b) allyl, (c) dienyl, (d) trienyl, (e) tetraenyl, and (f) pentaenyl groups. (g) Atomic model of the segment of an allyl group to illustrate the effect of C=C bonding on the positions of hydrogen atoms. The six hydrogen atoms are labeled as $H_i$ (i = 1-6) with the projected spacing marked as $D_1$ and $D_2$. (h) Crystal structure and atomic model of the PE repeating unit.

### 2.3.3 Anisotropy expansion in PE and PCL

Notably, there is an anisotropy expansion in PE and PCL under beam irradiation. As shown in **Figure 2.3d** and **Figure 2.7d**, the position shift of {110} and {200} diffraction at PE and PCL are disproportional. To verify the anisotropy expansion, the positions of {020} are also analyzed. Although the {020} diffraction in PE and PCL is weak (intensity less than one-sixth of those of {200} and {110}) and fade quickly, its position can be still extracted to check whether the expansions in three directions match together. **Figure 2.6** present the radial average profiles between 2.5-5.5 $nm^{-1}$ and position of {020} diffraction of PE and PCL at different accumulated dose. After 9.2 $e/Å^2$ and 12.0 $e/Å^2$, the {020} diffraction totally merge into the background, see **Figure 2.6a, b**, which is slightly quicker than the other two diffraction due to its small signal-noise ratio. The position of {020} diffraction and the neighboring amorphous ring can still be extracted, see **Figure 2.6b, d**.

The positions of {200}, {020}, and {110} diffraction of PE and PCL at two doses are listed in **Table 3**. At cryogenic condition, after PE accumulating 10.5 e/Å$^2$, the position of 200 and 020 are from 2.72 to 2.39 nm$^{-1}$ and 4.02 to 3.92 nm$^{-1}$, and then get a calculated 110 diffraction position from 2.43 to 2.30 nm$^{-1}$, namely a 5.7% expansion similar to measured 5.2% expansion. The positions have a good consistency and relevance in geometry which confirm the anisotropy expansion and proves the good fitting in our study.

The anisotropy expansion is no reported, and it could be caused by the different sensitivity of crystal planes. Due to the low symmetry in PE crystal structure and oriented polycrystalline composition whose diffraction is presented in the arc but ring, they imply the crystal planes should have different damage paces, and an anisotropy expansion could occur. Exactly, in the crystal growth of chain-folding PE, there is a preference for {110} and {100} growth face, as the lozenge-shaped and truncated-lozenge-shaped PE single crystal [2,118,119], while in the lamella, it can be a more complicated model but still include {110} and {100} growth face [120,121]. Considering the preparation process, high molecular weight, and thickness in PE (see Chapter 2.2.1), a chain-folding and preferential growth should occur [2,121]. Thus, when exposed to electron beam these planes present discrepant sensitivity, and an anisotropy expansion occurs.

**Table 3.** The fitting position of 200, 020, and 110 diffractions and their expansion ratio for PE and PCL under initial dose (0.6 and 0.9 e/Å$^2$) and 10.5 and 10.1 e/Å$^2$ at 98K condition. All error of position is below 0.01 nm$^{-1}$.

| Sample | Diffraction | Position (1/nm) at 0.6 e/Å$^2$ | Position (1/nm) at 10.5 e/Å$^2$ | Expansion ratio (%) |
|---|---|---|---|---|
| PE | 200 | 2.72 | 2.39 | 13.8 |
| | 020 | 4.02 | 3.92 | 2.6 |
| | 110 | 2.42 | 2.29 | 6.1 |
| | | at 0.9 e/Å$^2$ | at 10.1 e/Å$^2$ | |
| PCL | 200 | 2.71 | 2.58 | 5.0 |
| | 020 | 3.97 | 3.95 | 0.5 |
| | 110 | 2.41 | 2.37 | 1.7 |

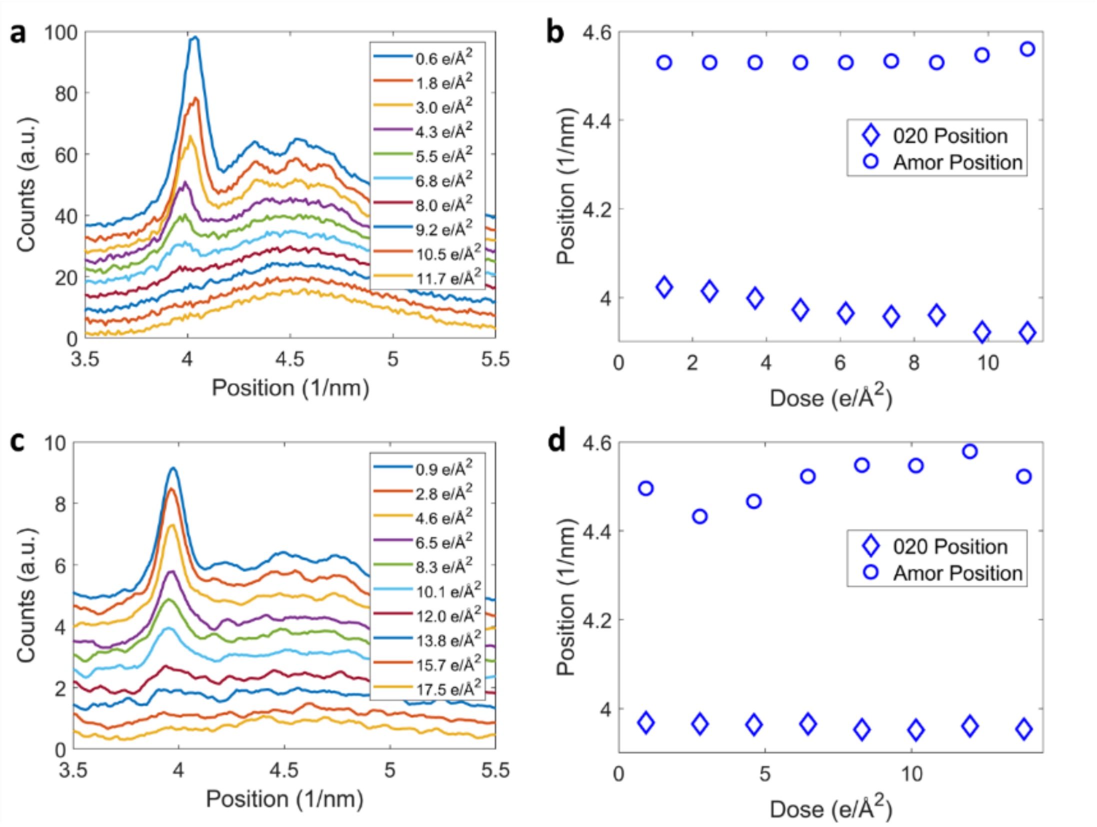

**Figure 2.6.** (a, c) The radial average profiles of PE (a) and PCL (c) (020) diffraction under accumulating dose. (b, d) The position of PE (b) and PCL (d) (020) diffraction and their near amorphous background under different accumulating dose. Error bars smaller than the size of marks are not shown.

## 2.4 Degradation of PCL under electron beam

Owing to the similar crystal structure to PE, the degradation of PCL is remarkably close to that observed in PE spherulite films. **Figure 2.7** and **Figure 2.8** presents the detected beam effects on PCL films by SAED patterns and EEL spectra.

### 2.4.1 Changes in PCL diffraction patterns

SAED of PCL is also dominated by {110} and {200} diffraction (**Figure 2.7a**), but with more prominent preferential orientation like single crystals as seen in the inset of **Figure 2.7c**. With accumulating more electron dose, both diffraction signals become weaker and shift towards the central beam. Curve modeling on the radial averaged SAED profiles illustrates these trends quantitatively: as displayed in **Figure 2.7b, c** for both temperatures the decay of $I_{cryst}$ in PCL is exponential with a faster initial drop that matches the increase of $I_{amorphous}$ at the early stage (**Figure 2.7c**), a sign of amorphization owing to the radiolysis damage. This is further evidenced by the amorphous halo that dominates the diffraction pattern at the final stage of beam exposure (inset of **Figure 2.7c**). The amorphization becomes considerably slower at 98 K, proving again the effectiveness of cryo-protection. On the other hand, the linear decrease of $I_{amorphous}$ at the late stage still demonstrates surface sputtering as the dominating beam effect when $I_{cryst}$ approaches zero. At both temperatures, beam effects on PCL appear to be slower than on PE, as reflected by the higher critical doses derived for PCL (**Table** 2).

**Figure 2.7d** shows the shift of 110 PCL diffraction from 2.41 to 2.31 nm$^{-1}$ after accumulating 26.7 e/Å$^2$ dose at 98 K, with a more rapid shift at RT. This corresponds to the increase of lattice spacing $d_{110}$ from 4.15 Å to 4.33 Å, ~4.3% expansion that is smaller than PE films. A larger shift is again observed for 200 diffraction, which shifts from 2.71 to 2.43 nm$^{-1}$ at 98 K corresponding to ~11.5% lattice expansion of $d_{200}$ (from 3.69 Å to 4.4.07 Å) after accumulating 17.5 e/Å$^2$ dose. The amorphous diffraction peak still shows negligible shift, excluding the heating effect as the cause of lattice expansion.

### 2.4.2 Changes in PCL EEL spectra

EELS on the exposed PCL (**Figure 2.8a, b**) also exhibits the exponentially enhanced signals in the range of 3-7 eV and 283-286eV (**Figure 2.8c, d**), corresponding to the formation of polyenyl groups and C=C band from the radiolysis beam effect, which is presumably responsible for the observed amorphization and lattice expansion similar to PE films. Meanwhile, for PCL, the calculated 110 diffraction position is from 2.40 to 2.36 1/nm, a 1.7% expansion same as the measured 1.7% expansion. All these observations are in notable agreement with results from PE films, suggesting the same damage mechanism in both materials, presumably owing to their similar crystal structure, polymer backbone structure, as well as sample thicknesses.

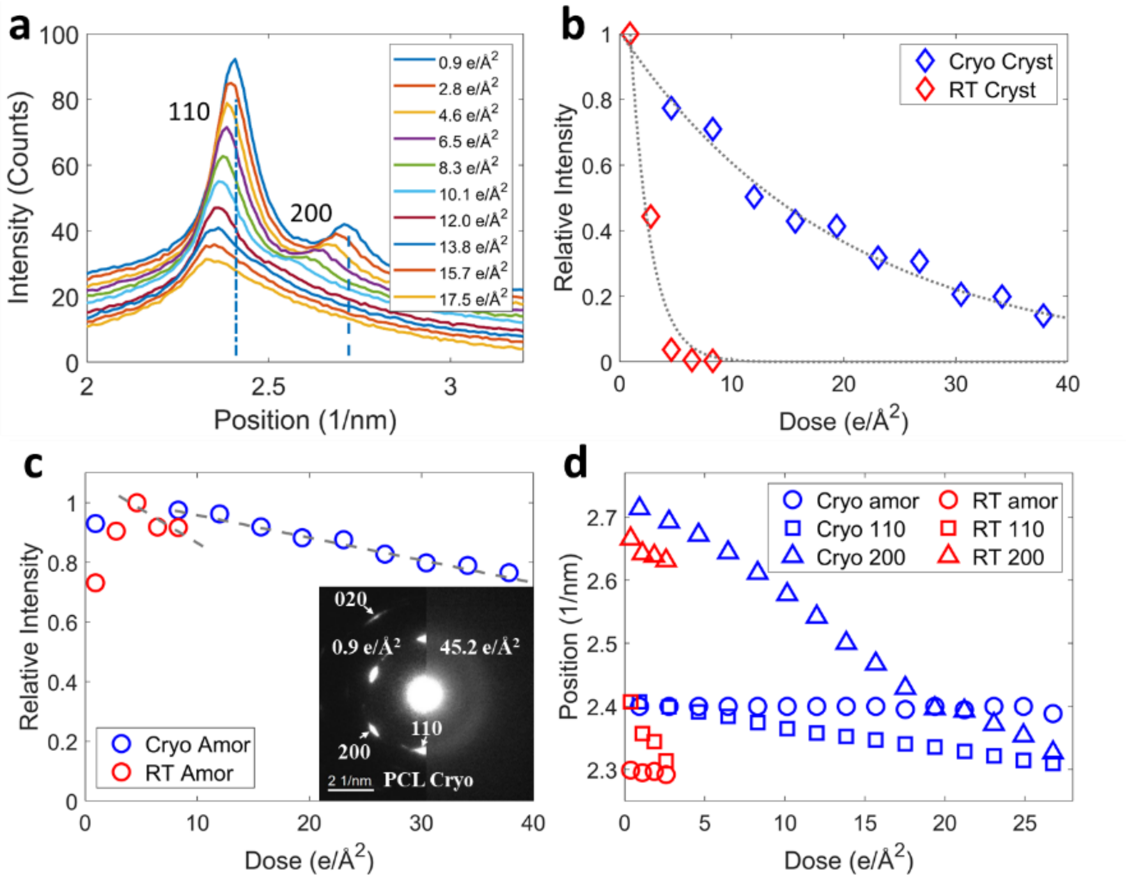

**Figure 2.7.** (a) Radial-averaged intensity profiles of SAED patterns from PCL at 98K under different electron doses. Profiles are shifted vertically with an incremental constant in sequence. (b, c) The relative intensity of (b) $I_{cryst}$, and (c) $I_{amorphous}$ as functions of accumulated electron dose for PCL at 98 K (blue) and RT (red), respectively. The exponential and linear decay is indicated by the fitted dashed lines. Inset in (c) shows SAED patterns on the same PCL film at 98 K (cryo) with the dose 0.9 (left) and 45.2 (right) e/Å$^2$ respectively, illustrating the amorphization process. (d) Peak positions of PCL 110 (square), 200 (triangle), and amorphous (circle) diffraction with increasing electron dose, at 98 K (blue) and RT (red), respectively. Error bars smaller than the size of marks are not shown.

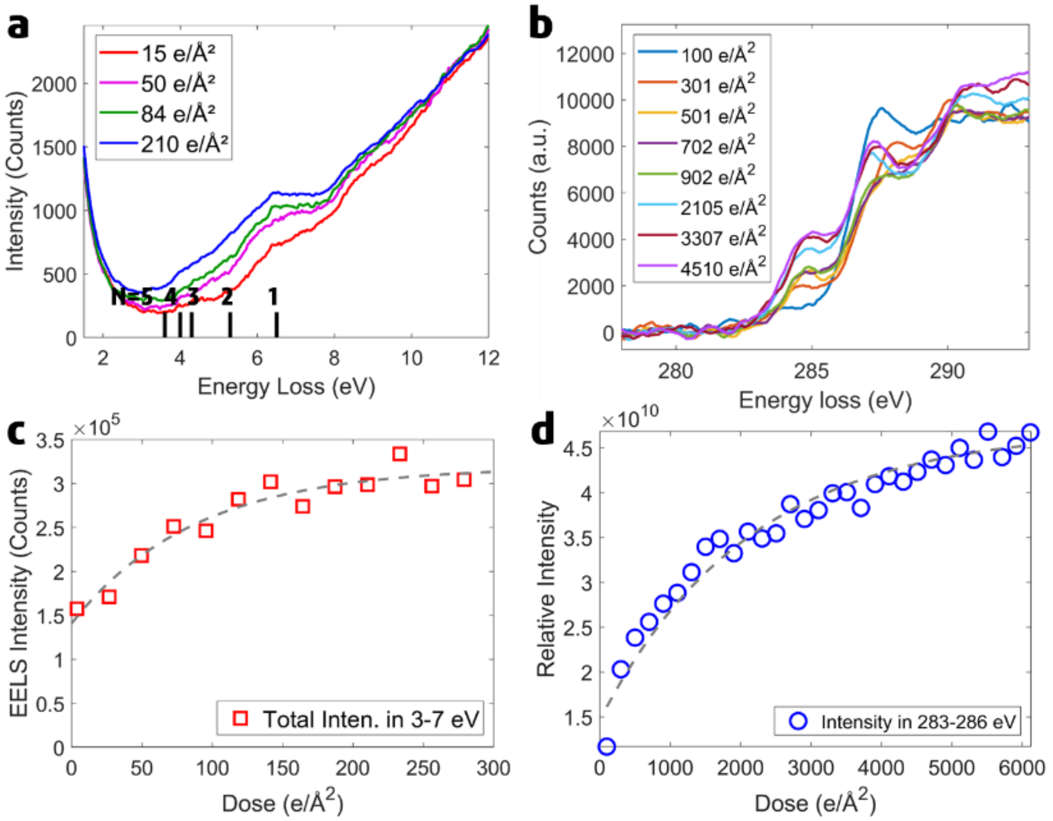

**Figure 2.8.** (a) Comparison of low loss EEL spectra from PCL under various electron doses at 98 K. The vertical black lines indicate the energy loss associated with polyenyl groups containing *N* unsaturated bonds. (b) The core loss EEL spectrums of PCL at the carbon K-edge under different beam irradiation with dose rate 200.4 e/Å$^2$. (c) Increase of polyenyl group signal (3-7 eV measured from EELS series in (a)) with increasing electron dose on PCL at 98 K, which follows an exponential function. (d) The intensity from 283-286 eV in (b) with accumulated electron dose, following an exponential increase as the fitted dashed lines. Error bars smaller than the size of marks are not shown.

## 2.5 Degradation of P3HT under electron beam

P3HT films, which possess conjugated $\pi$ bonding, display distinct degradation behavior in contrast to PE and PCL, demonstrating the complexity of beam effects in organic solids. It is noted primarily that the crystal structure of P3HT should be the *Form-II* structure [122-124] ($a$ = 13.5 Å, $b$ = 9.1 Å, $c$ = 7.9 Å, $\gamma$=69.3°) due to $CS_2$ vapor annealing (see Chapter 2.2.1) as reported in the previous literature [125-127]. This structure has an important feature that the normal of (320) crystal plane is along the $\pi$-stacking direction and $c$ axis is along the backbone direction, and this orientation distinctly impact the observed diffraction patterns. As shown in **Figure 2.9a, c**, the main diffraction rings are $002_{\text{II}}$ and $320_{\text{II}}$ is in 2.57 and 2.67 $\text{nm}^{-1}$ at 98 K in agreement with the expected position, revealing a prominent *Form-II* structure. Moreover, the mobility measurement indicates that the backbone direction and the $\pi$-stacking direction should be primarily in plane [128-130], evidencing the *Form-II* structure again.

### 2.5.1 Changes in P3HT diffraction patterns

Interestingly, in P3HT, after accumulating an electron dose of 20.3 e/$\text{Å}^2$, $002_{\text{II}}$ diffraction becomes much fainter compared to $320_{\text{II}}$ diffraction, as revealed by the radial-averaged SAED profiles in **Figure 2.9c.** Furthermore, the associated diffraction intensity derived from Gaussian modeling demonstrates the rapid decay of $002_{\text{II}}$ diffraction at the early stage of beam exposure, whereas the $320_{\text{II}}$ diffraction peak remains relatively stable. Upon the extinction of $002_{\text{II}}$ diffraction, the decay of $320_{\text{II}}$

diffraction starts with an intensity plateau separating the exponential decay of the two diffraction signals. Since $002_{II}$ diffraction reflects the ordering of the side chains, while $320_{II}$ represents the π-stacking ordering, this two-stage decay process suggests that the electron beam preferentially alters the side chains first, while the π-conjugated polythiophene backbone is more resilient to electron irradiation. This discovery of a two-stage beam effect in P3HT was not previously reported.

In contrast to 98 K measurements, RT measurements on P3HT do not show the two-stage decay due to the absence of $002_{II}$ diffraction, even in the first SAED pattern, as shown in **Figure 2.9b, d**. This indicates the presence of degradation that eliminates $002_{II}$ diffraction at a low electron dose of 0.6 e/Å2. With further beam exposure at RT, diffused diffraction halos reflecting the amorphization process emerge. This restricts us to using the decay of $320_{II}$ diffraction to derive the critical dose of P3HT at RT, while the critical dose at 98 K is derived from the decay of $002_{II}$ diffraction, both values are presented in **Table 2**. The higher critical dose for P3HT can be attributed to the presence of the conjugated π-electron system and the absence of C-H bonds in its backbone compared to PE and PCL [1,43], which also explains the damage to the side chains (consisting of C-H bonds) before the π-conjugated backbones. However, our P3HT critical dose is considerably lower than previous reports [34,39], which could be due to the smaller film thickness (~15 nm vs. ~90 nm [34]) and the potentially different polymorphs (*Form-II* vs. *Form-I*).

In addition to revealing the two-stage damage process, **Figure 2.9e** also demonstrates the preferential suppression of radiolysis effect in P3HT thin films at cryogenic temperature: When $I_{cryst}$ approaches zero at ~50 e/Å$^2$ dose (**Figure 2.9e**), $I_{amorphous}$ also becomes negligible at 98 K (**Figure 2.9f**), in contrast to the considerable $I_{amorphous}$ observed at RT when $I_{cryst}$ drops to zero. As a result, no amorphous diffraction halo forms in P3HT at 98 K, indicating the suppressed amorphization process. Moreover, as shown in **Figure 2.9f**, $I_{amorphous}$ decreases monotonically at 98 K without any increasing stage, in contrast to the initially rising $I_{amorphous}$ at RT (red circles) as well as for PE and PCL spherulite films (**Figure 2.4c** and **2.7c**). This implies that the surface sputtering effect dominates from the beginning of beam exposure, presumably due to the preferential suppression of radiolysis at cryogenic temperature. The reasons for different damage path of $I_{amorphous}$ at RT and 98K shown in **Figure 2.9f** could include the probability of sputtering and thickness of samples and is discussed in **Appendix A.2**.

Further, the peak position analysis shown in **Figure 2.9g** also illustrates that only at RT we can observe a shift of $320_{II}$ diffraction from 2.67 to 2.55 nm$^{-1}$ after accumulating 16.0 e/Å$^2$ dose, whereas no shift can be consistently detected at 98 K. As lattice expansion is attributed to the radiolysis beam effect, this provides further evidence of the preferentially suppressed radiolysis in P3HT at cryogenic condition. The inelastic mean free path of electrons is about 100-200 nm in common polymers at RT [131,132] and increases further with decreasing temperature. [133] Thus at 98 K, the inelastic mean free path should be substantially larger than the thickness of P3HT films (~15 nm), explaining the suppressed inelastic scattering and the radiolysis effect. On the other hand, the effect of cryo-protection on surface sputtering appears to be limited in P3HT, as reflected by the similar decay rates at the two temperatures for both $I_{cryst}$ and $I_{amorphous}$ (**Figure 2.9e, f**).

### 2.5.2 Changes in P3HT EEL spectra

**Figure 2.9h** presents the characteristic EELS signal corresponding to the interband transitions in P3HT at 98 K , where the edge onset from the pristine sample (after accumulating 4 e/Å$^2$ dose) matches its bandgap energy ~1.7 eV [42,134]. With increasing electron dose, the signal intensity within the range of 1.5 to 3.5 eV decreases linearly (**Figure 2.9i**), which is characteristic of surface sputtering [1,27] and also consistent with the suppression of the radiolysis effect at this low temperature. Additionally, a shift of the EELS edge onset towards higher energies, from 1.73 to 2.14 eV after accumulating 119 e/Å$^2$ dose, is also observed (**Figure 2.9h, i**). Both the intensity drops, and energy shifts are in accordance with the previous EELS study on P3HT [134]. Moreover, the signal within the range of 3-7 eV remains constant throughout the whole process of beam exposure, indicating the absence of polyenyl group formation and hence a distinct damage mechanism from PE and PCL films.

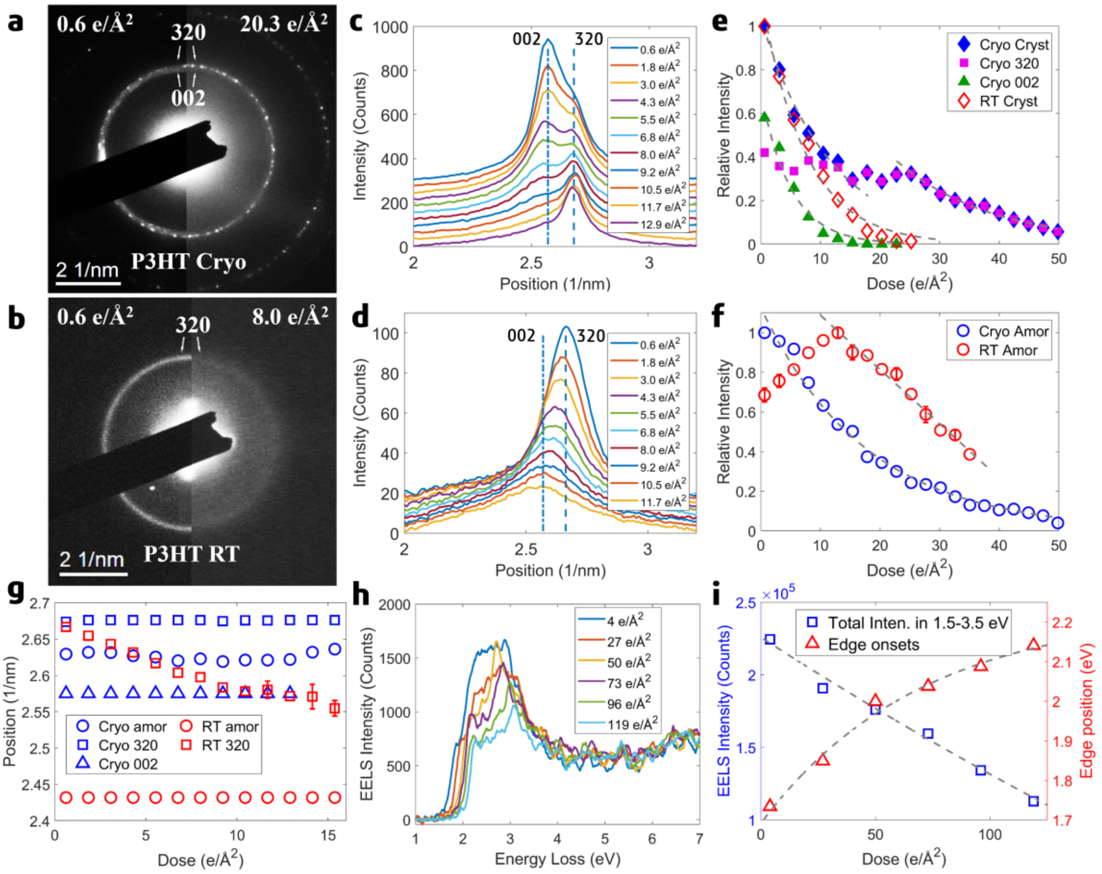

**Figure 2.9.** (a-d) SAED patterns and the corresponding radial-averaged intensity profiles from P3HT films under different electron doses at (a, c) 98 K and (b, d) RT, respectively. Profiles are shifted vertically with an incremental constant in sequence. (e) $I_{cryst}$ and (f) $I_{amorphous}$ as functions of accumulated electron dose for P3HT at 98 K (blue) and RT (red), respectively. The exponential and linear decay is indicated by the fitted dashed lines. (g) Peak positions of $320_{\mathrm{II}}$ (square) and amorphous (circle) diffraction under the increasing electron dose at 98 K (blue) and RT (red), respectively, and peak position of $002_{\mathrm{II}}$ diffraction (blue triangle) at 98 K. (h) Comparison of background-subtracted EEL spectra under different electron doses at 98 K. (i) Change of P3HT integrated EELS intensity in the range of 1.5 to 3.5 eV (blue square), and shift of the EELS edge onset (red triangle) with increasing electron dose at 98 K. The exponential and linear decay is indicated by the fitted dashed lines. Error bars smaller than the size of marks are not shown.

## 2.6 Conclusion

In summary, we have characterized the effects of high-energy electron beam on PE, PCL, and P3HT spherulite films at room and cryogenic temperatures, through analyzing quantitatively both SAED and EELS under different electron doses. By distinguishing signals from crystalline and amorphous phases, beam effects including surface sputtering from the knock-on effect and amorphization from radiolysis have been clearly identified, most of which can be suppressed effectively by cryo-protection.

For PE and PCL spherulites, beam effects are initially dominated by radiolysis, which leads to amorphization as well as lattice expansion. EELS analysis further unravels the formation of unsaturated polyenyl groups generated by radiolysis of C-H bonds, providing a feasible mechanism for both amorphization and lattice expansion processes. At the late stage, both PE and PCL appear to be largely amorphized, with the linear decrease of the amorphous phase owing to surface sputtering. Moreover, the quantification of diffraction position firstly reveals an anisotropic expansion due to the difference of crystal planes in beam sensitivity.

On the other hand, P3HT spherulites exhibit more complicated two-stage damage process at cryogenic temperature, with the sidechain ordering preferentially damaged before the π-stacking ordering. The suppressed radiolysis effect in P3HT at cryogenic temperature is also identified, which can be attributed to both cryo-protection and ultrathin film thickness compared to the inelastic mean free path.

At last, the unraveled damage mechanisms in this work have demonstrated the power of our quantitative analysis on understanding the detailed beam effects on structure and chemical bonding of organic solids, which should offer valuable guidance for optimizing TEM imaging conditions under the controlled electron dose, to achieve pristine sample information with minimized artefacts.

# Chapter 3 Microstructures of PE and PCL

## 3.1 Introduction

The investigation of structures and morphologies of polymers is a topic of great significance, owing to their inherent link with performance and application. It is known that the local orientation and crystallinity can affect the properties [10-16], and local structure variation and domain switch are also expected [136, 136]. Chapter 2 of this study has shed light on the underlying mechanism of beam damage on polyethylene (PE) and polycaprolactone (PCL). Building upon this understanding, in this chapter, we present an optimized low-dose 4D-STEM technique for study the polymeric spherulite thin films, using a dose of approximately 0.4 e/Å$^2$ for each acquisition. This optimized approach enables the preservation of pristine components while facilitating nanoscale detection of microstructures.

By leveraging analytical algorithms, we can selectively extract a plethora of local intrinsic information contained within 4D diffraction arrays. Consequently, microstructures in PE and PCL spherulite thin films are explicitly demonstrated. For PE, there was a growth direction along [1-10] crystal direction and a twist approximately around the crystallographic b axis in the lamellae within the spherulites. In the polar angle direction, the orientation is continuous with general circular symmetry. For PCL, lamellae twist was not observed in POM and TEM, but a growth direction along the [1-10] crystal direction still occurred. In the polar angle direction, local amorphous phases were observed which causes the separated radial pattern in HAADF images. Moreover, changes in degree of crystallinity are also presented with an increased ratio of amorphous from cores to peripheries in both PE and PCL.

By delving into these pristine structures, our comprehension of polymer materials is significantly deepened, augmenting the exploration of their potential applications.

## 3.2 Methods

### 3.2.1 Materials

The research on microscale ordering employs the same samples of PE and PCL spherulite thin films used in the research of polymer degradation, with a thickness of approximately 140 nm and 200 nm respectively. All preparation methods and raw materials are consistent, as discussed in Chapter 2.2.1, unless otherwise specified.

### 3.2.2 TEM Operation

**4D-STEM datasets acquisition**: Datasets were acquired either on a ThermoFisher Scientific Spectra 300 equipped with an EMPAD, operated at 300 kV, or a JEOL JEM ARM 200CF microscope equipped with a OneView camera, operated at 200 kV.

As discussed in Chapter 2, it is known that the crystal structures of PE and PCL can be significantly damaged within a few e/Å$^2$. At room temperature, the damage occurs at approximately 1 and 2 e/Å$^2$ for PE and PCL, respectively. At cryogenic conditions, the damage thresholds are higher, around 9 and 20 e/Å$^2$ for PE and PCL, respectively.

To ensure the acquisition of pristine and intrinsic diffraction patterns, the electron dose applied to the samples should be kept as low as possible while still yielding recognizable diffraction patterns. In the study, we use a typical electron probe nearly parallel with a convergent angle 0.1mrad and a current of ~ 0.5 pA as counted by the EMPDA. This electron probe is estimated to illuminated region with a diameter of ~ 10 nm [135], thus a dose rate of approximately 400 e/ ($Å^2$ s). For each diffraction pattern, the dwell time is typically 1 ms, thus an accumulating dose ~0.4 e/$Å^2$ which is low enough to preserve the intrinsic crystal structure and enable the multiple acquisition for same regions. Furthermore, it's worth noting that the scanning steps in the presented results were chosen to be larger than 10 nm. This was done to avoid probe overlap during the scanning process which can significantly increase beam damage. Moreover, to reduce the beam damage from the sample searching, the region for 4D-STEM acquisitions only endure one ultralow dose exposure (> 0.011 e/$Å^2$) of HAADF acquisition for sample confirmation.

### 3.2.3 Orientation Reconstruction

The steps of data processing of 4D diffraction patterns are shown in **Figure 3.1**, and six diffraction patterns in the labelled position (square) of **Figure 3.1e** are shown in **Figure 3.2**. These orientation of (1-10) crystal plane, namely the normal direction of (1-10) crystal plane, in diffraction patterns is similar to our reconstructed result proving the success of orientation reconstruction.

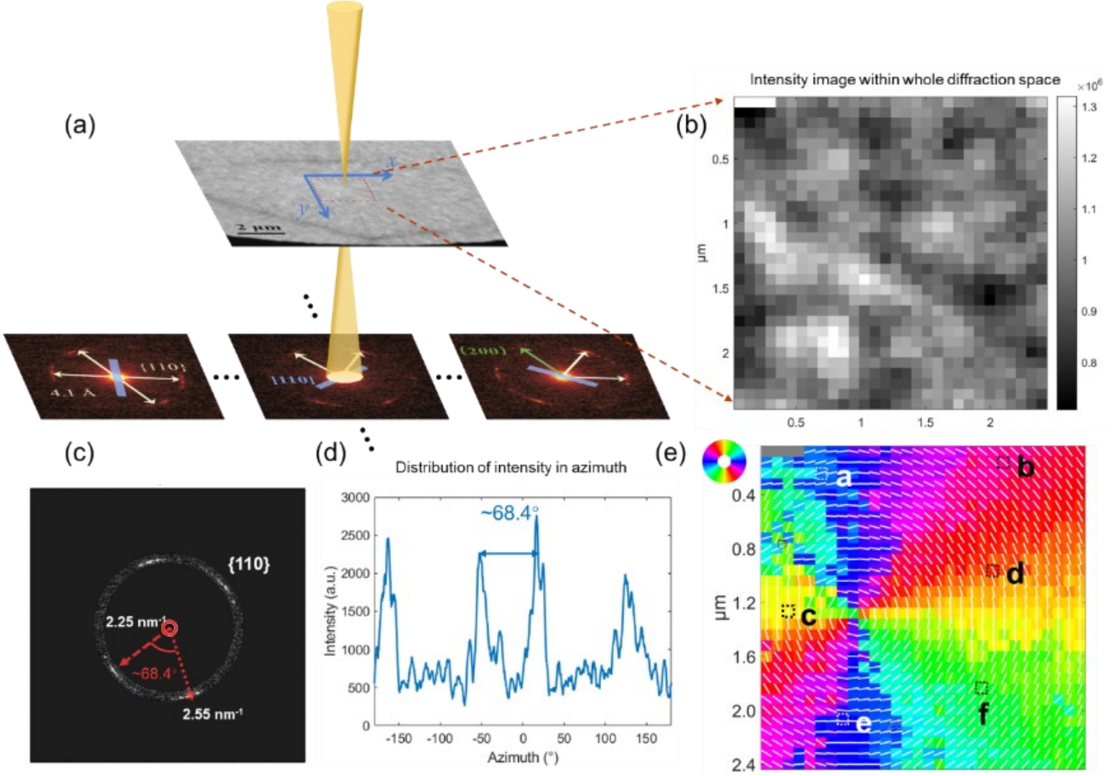

**Figure 3.1.** Schematic demonstration of the data processing steps for orientation reconstruction. (a) Schematic diagram of acquisition of 4D datasets. The selected ROI of a PE spherulite thin film is scanned by raster array of electron probe, where a diffraction pattern is recorded at each scanning position to make the diffraction containing the locally spatial information. (b) Intensity image of the scanning region in (a) over whole recorded diffraction space. (c) Masked diffraction pattern to exclude other signal where only {110} diffraction arcs/points are considered for orientation. (d) Transformed 1D diffraction profile of (c) for locating the azimuth of diffraction arcs/points. (e) Reconstructed orientation map of (1-10) crystal plane depending on the datasets acquired in (a), where the diffraction patterns of six positions (square) shown in **Figure 3.2** is consistent to our orientation map. The color wheel shows the relationship between polar angles and colors.

Here are the specific steps of the data acquiring and processing:

1. Selection of Region of Interest (ROI): A region of interest with minimal preliminary exposure is chosen, as shown in **Figure 3.1a**. It is crucial to zero the scanning rotation to ensure that the coordinates correspond to those of the scanning system.

**2.** Simultaneous Acquisition of Diffraction Patterns and Intensity Image: Diffraction patterns are acquired simultaneously while generating the intensity image of the scanning region, as depicted in **Figure 3.1b**. This setup helps monitor the electron damage condition and avoid destroying characteristic regions.

**3.** Postprocessing Scripts:

**(3.1)** Alignment Script: An alignment script is used to correct the shift of the diffraction center with a precision higher than one pixel. This script employs a custom-coded center of mass (COM) algorithm and a Circular Hough Transform (CHT) based algorithm to identify central transmission points in the diffraction patterns.

**(3.2)** Quick Mask Extraction Script: This script extracts the desired diffraction ring such as the {110}, {200}, and {020} diffraction family. GPU acceleration is utilized to perform matrix calculations and transform the coordinates from Cartesian to polar coordinates, compressing the 2D images into 1D azimuthal profiles, as shown in **Figure 3.1c, d**.

**(3.3)** Orientation Estimation Script: This script identifies the orientation based on various factors, including symmetry, chirality (for example, in the {110} diffraction points of PE, the (1-10) direction is always 111.6° away from the (110) direction and 68.4° away from the (-110) direction), diffraction point intensity. The polar angle of orientation is calculated by local maxima algorithms, and COM algorithms (the latter is mainly employed to determine the exact azimuth for arc-like diffraction patterns).

The algorithm of orientation reconstruction is feasible for the datasets from two TEM, especially robust for datasets acquiring from EMPAD. The reasons are the high SNR and small probe size which makes diffraction patterns close to that of single crystal.

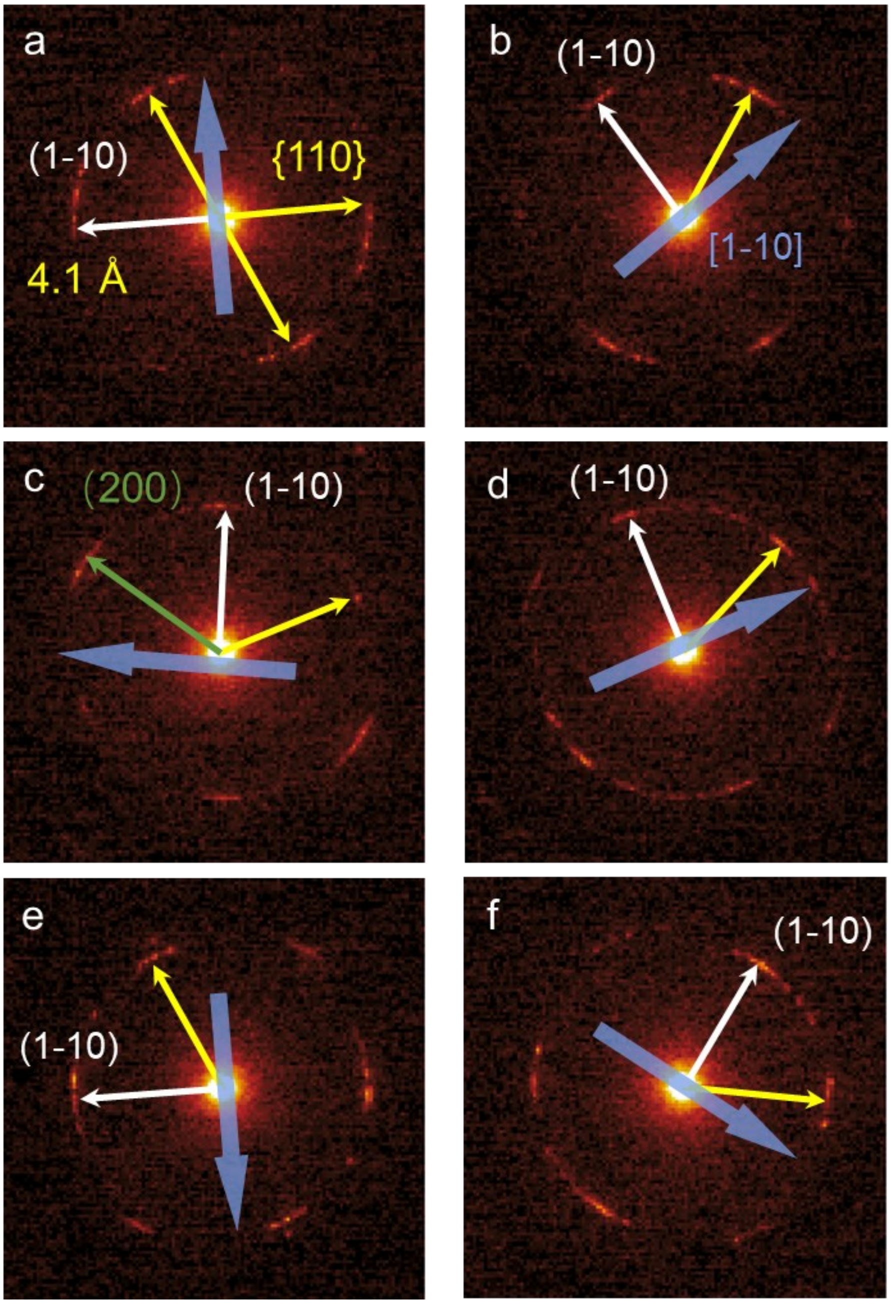

**Figure 3.2.** Diffraction patterns from the position of labelled in **Figure 3.1e**. Yellow arrows for the {110} crystal planes, white arrows for (1-10) crystal plane, green arrows for (200) crystal plane, and blue arrows for the [1-10] crystal direction.

### 3.2.4 Phase Reconstruction

The reconstruction of the phase, mainly for the amorphous and crystalline phases, in polymeric spherulite thin films follows some similar processing steps as the orientation reconstruction. The difference is from the postprocess. The phase reconstruction averages the reciprocal azimuth direction and converts the 2D diffraction patterns into profiles of radial distance (here it is distance of reciprocal in unit of 1/nm), thus compressing the 4D datasets into 3D datasets, same as the script discussed in Chapter 2 for time-series diffraction patterns. Moreover, the algorithms based on GPU-accelerated principal component analysis (PCA) and model-based least-square fitting were used to solve the radial-averaged intensity profiles of DPs for more quickly identifying the crystalline and amorphous phases.

## 3.3 Orientation map

As shown in **Figure 1.5**, **Figure 2.1**, **Figure 3.3**, the POM image of PE and PCL exhibit Maltese crosses and extinction bands despite low contrast in **Figure 3.3a** due to the thin thickness (short light path) and local concavity. The presence of Maltese crosses indicates a rotation of the crystal structure around the core of the spherulites in these thin films. Additionally, the extinction bands observed suggest a twisting or screw dislocation of the polymeric lamellae binds within the spherulites.

**Figure 3.4** presents their STEM HAADF images at low magnification, showing their individual textures. The HAADF image of PE (**Figure 3.4a**) reveals a series of concentric rings around the spherulite cores, alternating between dark and bright regions, extending until the boundaries. The neighboring spherulites can be clearly distinguished by the presence of obvious boundaries. On the other hand, the HAADF image of PCL (**Figure 3.4b**) exhibits radially irradiating beams of alternating brightness, without the presence of concentric rings. These distinct textures observed in the HAADF images suggest possible differences in microstructure between PE and PCL, despite their similar crystal structure.

However, it is important to note that the STEM images alone cannot directly indicate the local structural variations within the spherulites. Additionally, AFM results indicate no surface periodic fluctuations, and thus the textures are not caused by the variation of thickness. Hence, to gain insights into the local changes occurring within the spherulites, 4D-STEM is employed for a comprehensive examination within a whole spherulite.

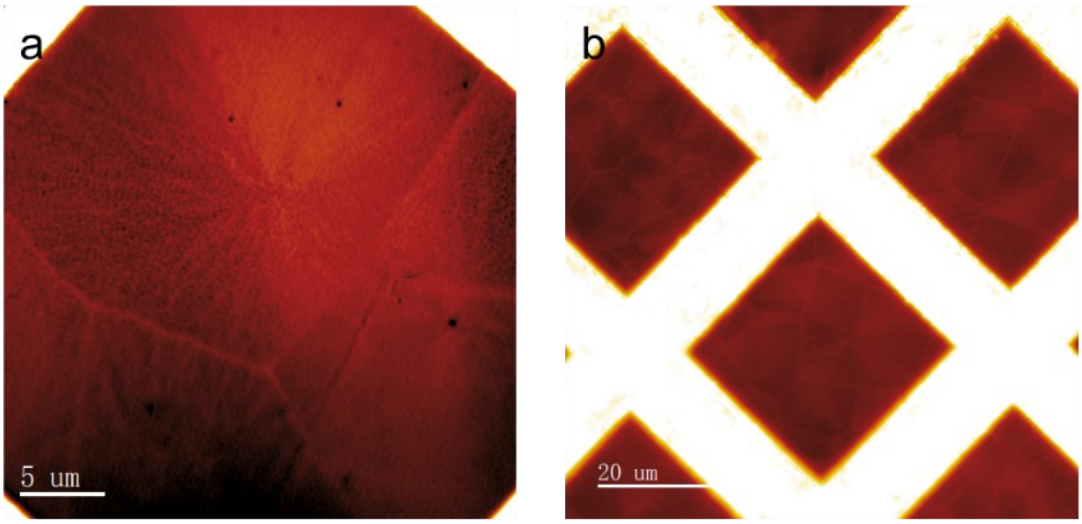

**Figure 3.3.** Polarized optical microscopy images of PE (a), PCL (b) on copper grids. Due to the unevenness of thin films supported by grids, the contrast is low, but the texture of extinction bands of PE still can be observed in (a), and at a low magnification in (b), the Maltese crosses of spherulites are more considerable.

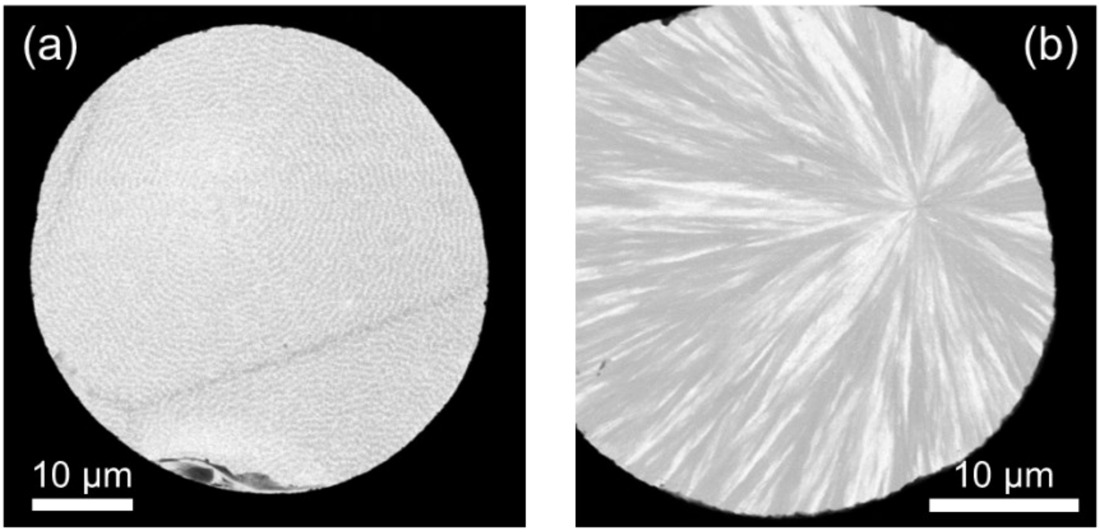

**Figure 3.4.** HAADF images of PE (a), PCL (b) on copper grids. The mass-thickness contrast shows the individual texture of PE and PCL. PE has a series of concentric rings around the core of spherulites, while PCL exhibits the radially diverging texture from the core of spherulites.

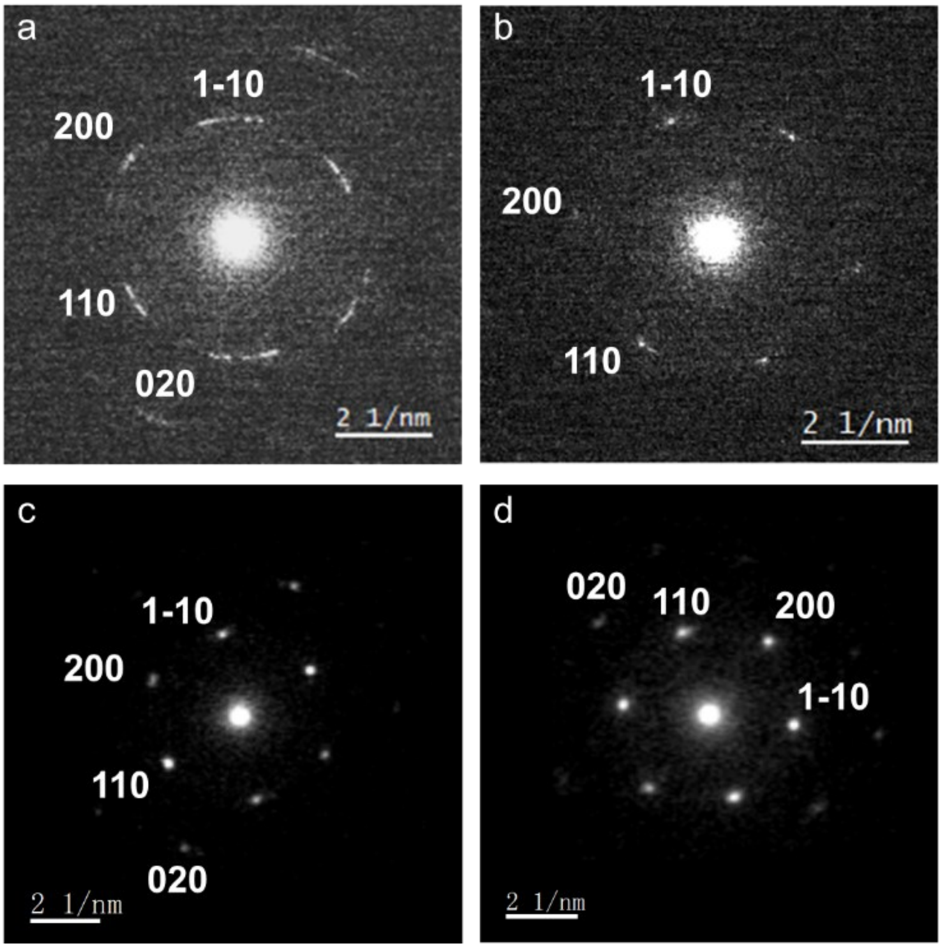

**Figure 3.5.** The typical CBED patterns of PE (a, c) and PCL (b, d) from 4D-STEM datasets with the comparable acquiring parameters, respectively acquired from Jeol ARM 200CF (a, b), and Spectra 300 (c, d).

Before discussing the PE orientation map, the quality of diffraction patterns as the cornerstone for quantitative analysis needs to be evaluated firstly. **Figure 3.5** showcases some typical electron diffraction patterns obtained from Jeol ARM 200CF (a, b) and Spectra 300 (c, d) instruments. It is important to note that although a convergent electron probe is used, the large disks typically seen in convergent beam electron diffraction (CBED) are not visible here. Instead, the diffraction patterns resemble SAED patterns due to the small convergent angle, making them easier to solve and quantify.

All the diffraction patterns exhibit distinctly crystalline diffraction points or arcs, with feeble visibility of amorphous signals. The distances between the (110) and (200) diffraction peaks align with the theoretical values, confirming a milder level of damage by our beam damage results in Chapter 2. Additionally, there is a significant reduction in noise, indicating the powerful single detection capability of the EMPAD. This reduction in noise is advantageous as it minimizes identification errors and reduces computational costs. Furthermore, the high-quality diffraction patterns without overlap or signal overflow enable the tracing of specific diffraction families. This allows for focused analysis without interference from diffused signals originating from other neighboring diffraction.

Besides, the beam damage from the 4D-STEM acquisition by Jeol ARM200CF is exhibits in a STEM image (**Figure A.1**) and discussed in Appendix A.3 revealing an inevitability of polymeric damage. In Chapter 3.4, more quantitative cases are discussed.

### 3.3.1 PE orientation map

In Chapter 3.2.3, the {110} diffraction family between 2.25-2.55 nm$^{-1}$, encompassing the whole angle is utilized to determine the local orientation within the sample. The {110} diffraction family is the dominant one within this range, thus without interference from other diffraction.

**Figure 3.1d** illustrates an example of the intensity distribution of the (110) diffraction in the polar angle. By analyzing the configuration of four {110} diffractions, the orientation of each position can be defined. Starting from the (110) diffraction, a clockwise rotation of approximately 111.6° corresponds to the (1-10) diffraction, while a counterclockwise rotation of approximately 68.4° corresponds to the (-110) diffraction, and vice versa. This allows for the differentiation of the (110) and (1-10) diffractions. The identification of (110) and (1-10) diffraction is enough because the other two diffractions are their symmetric counterparts.

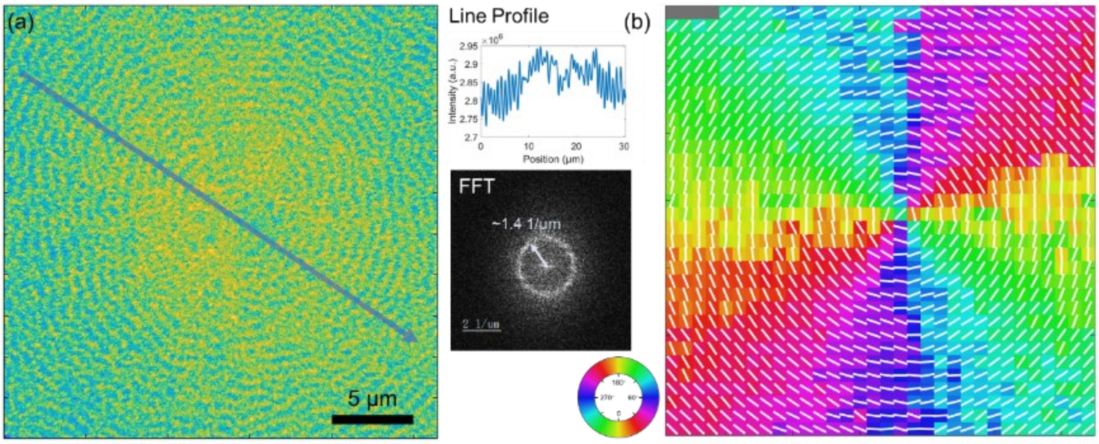

**Figure 3.6.** PE orientation map of the normal of the (1-10) crystal plane (b) and its HAADF image of detecting area (a). Inset of (a) shows the line profile of the blue line in (a), and the FFT of whole image (a), which uncover a spacing of extinction band of ~ 700 nm. The Orientation map show a centrosymmetric continuous structure whose circle of structure rotation is the same as the annular texture in its STEM image. Inset of (b) is the color wheel representing the relationship between angles and colors.

**Figure 3.6** presents the orientation map of the direction of the (1-10) crystal plane, accompanied by the STEM image of the detected area. The orientation maps based on the (200) and (110) diffraction points are discussed in Appendix A.4, which show a fantastic central helical symmetry. In **Figure 3.6a**, the STEM image exhibits a series of concentric bands with a spacing of around 700 nm, measured from the intensity profiles (inset in **Figure 3.6a**) along the blue line passing through the nucleus and the reciprocal ring in its FFT image (inset in **Figure 3.6a**). **Figure 3.6b** displays the orientation map by tracing polar angles of the normal of the (1-10) crystal plane at each position, depicted as white arrows in **Figure 3.2**. Note that the first four data points are disregarded due to probe drift, thus gray.

Since this result is sparse in pixel with a step of ~ 0.8 μm (larger than the spacing of extinction bands) acquired at Jeol ARM 200CF, the orientation cannot reveal the annual extinction band. However, the 32x32 diffraction array and a similar result shown in **Figure 3.1e** still reveal the general continuous center symmetry in PE spherulite thin films aligns with the annular texture observed in the STEM and POM images, where a continuous lattice deformation around the nucleus of spherulites occurs at a sub-micrometer scale.

Because the growth front always outwardly extends from the core to the periphery, the growth direction vertical to the growth front should point outside from the core, which is consistent with the implication of the center symmetry. The mapping of the [1-10] crystal direction in PE aligns with the growing model as shown in **Figure 3.7b.**

Thus, our observations indicate that the [1-10] crystal direction is the main growth direction in PE spherulites.

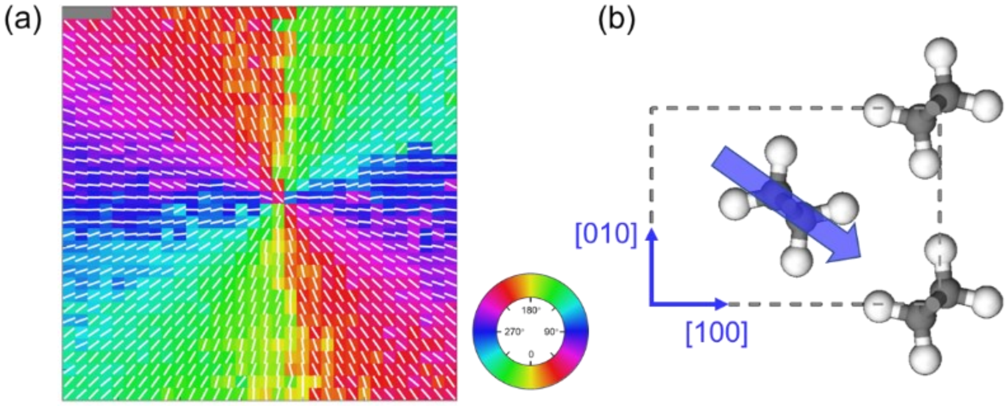

**Figure 3.7.** (a) Mapping of growth-direction map from the region in **Figure 3.6a**, showing radially diverging growth direction from the core. (b) Crystal structure of PE showing the direction of [1-10] (big blue arrow). Inset of (a) is the color wheel representing the relationship between angles and colors.

The radial growing style (from core to periphery) is matched with the reported and theoretical expectation [137-139]. However, if following the assumption that spherulite radial direction is the growth direction, the exact growth direction in spherulites is along the normal of {110}, little different to the reported that b axis is the growth direction [3,119,137].

One possible explanation for this discrepancy is that the together growth along both the normal of (110) and (1-10) is equivalent to a growth along the <1-10> crystal direction, as depicted in **Figure 3.8**. Once one of the <1-10> direction is suppressed by squeezing against adjacent each other, the lamellae could grow into a long strip along the other <1-10> direction. Furthermore, the folding mechanism may also play a role in this deviation. It is known that the folding direction in PE single crystals occurs along [1-10] or [110] [3,119,137], as illustrated in **Figure 3.8.** The {110} planes are energyfavored. During the growth of spherulites, chain folding for crystallization and the construction of crystals for spherulites occur simultaneously. Considering the spherulite as a combination of lamellae, the continuous chain folding extends outward, leading to the overall growth direction along the [1-10] crystal direction. However, these speculations do not have evidence, and the origin for the counterintuitive growth requires more research.

Nevertheless, our technology based on the 4D-STEM system have unveiled exclusive details, thereby posing a significant challenge to the widely accepted growth direction along the b-axis in spherulites, as inferred from the indicatrix [137]. These discoveries underscore the critical role of cutting-edge imaging techniques in elucidating novel perspectives and reevaluating preexisting knowledge within this domain of study.

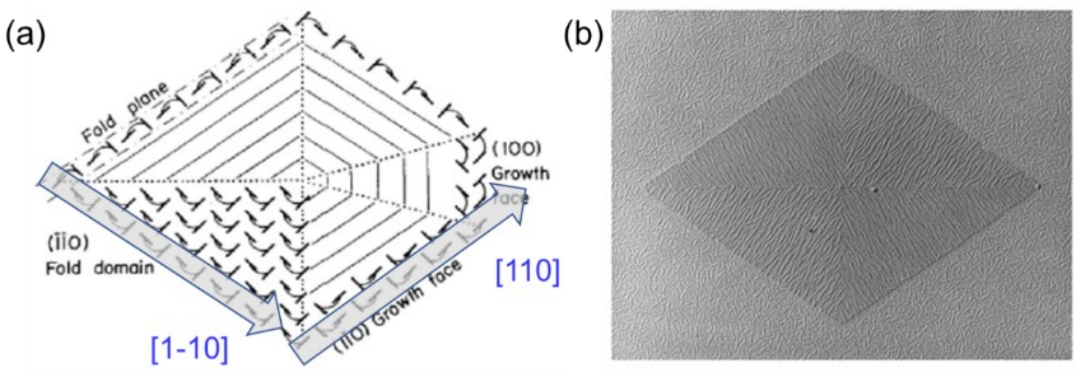

**Figure 3.8.** (a) Illustration of four sections of folding orientations in PE single crystals, reproduced from [3]. Gray arrow for the [1-10] crystal direction. (b) TEM image of PE thin film with surface decoration of paraffin for revealing the folding direction, reproduced from [119].

### 3.3.1 PCL orientation map

Reconstructing the orientation of PCL is achieved using a similar method to that employed for PE, owing to their similar crystal structures. **Figure 3.9** exhibits the

HADDF image for the acquiring region, and the orientation map of PCL spherulite thin films based on (1-10) diffraction and [1-10] crystal direction, which are acquired at Jeol ARM 200CF. The region analyzed corresponds to a part of the region depicted in **Figure 3.4b**, and the overlapped red lines in **Figure 3.9a, c** respectively represent the local orientation of the (1-10) diffraction and [1-10] crystal direction. A strong correlation is observed between regions of high HADDF contrast and regions where {110} diffraction is observable.

The orientation of (1-10) crystal plane in each position surrounds the nucleus and can form a series of concentric circles, albeit with some missing parts. Thus, the growth direction of PCL spherulites is still from the nucleus towards the periphery, consistent with the dendritic-like growth manner observed by Vincent via *in situ* AFM [140]. Their PCL spherulite thin films exhibit a similar dendritic-like morphology, In that growth mode, main branches are firstly grown and the gap between branches is then padded thus could be more random and amorphous.

Unlike PE, HAADF images of PCL do not exhibit any extinction bands, which is a major difference in morphology. Furthermore, both the HAADF image and the orientation map show a centrosymmetric radial structure composed of divergent strips radiating from the cores. In HAADF images, the contrast in the strips arise from the different mass thickness due to the collection angle being larger than 70 mrad, where no diffraction signal is captured. Considering the even thickness observed in PCL thin films tested by AFM, without significant fluctuations, the differences in contrast may arise from either inhomogeneous crystallinity or local tilting of the zone axis. The former is discussed in the next subchapter, while the latter requires more tests for confirmation.

In the orientation maps, the contrast in the strips mainly arises from weak or even absent diffraction intensity, making it challenging to identify orientations that include both crystalline and amorphous signals. To address this issue, the 4D diffraction patterns acquired while detecting single electrons need to be analyzed. **Figure 3.10** presents an ADF image and its corresponding orientation map acquired using the Spectra 300 instrument, using a 200x200 dataset with a 50 nm step size. The results obtained are similar to those acquired using the Jeol ARM 200CF, indicating that the regions without orientation represent an intrinsic feature of PCL spherulite thin films, but from the limitations of the detection capability.

Significantly, the orientation maps or growth direction map depicted in **Figure 3.9** and **Figure 3.10** exhibit a discernible inclination of some specific growth directions. This is evident from the non-random arrangement of bright and dark regions, which demonstrate a symmetrical pattern with prominent directions near the nucleus, as opposed to the uniform distribution of growth directions observed in **Figure 3.6** for PE spherulite thin films. **Figure 3.11** presents a histogram of growth directions, revealing three dominant directions. These directions correspond to polar angles of 16.8°, 82.2°, and 139.6°, with included angles measuring 65.4°, 57.2°, and 57.4° respectively. These angles bear resemblance to the angles between (110) and (200) (56.3°) and (110) and (-110) (67.4°). It should be noted that the distribution of the three dominant directions is not identical, but it can be caused by the deviation of the nucleus from the image center. Consequently, it can be inferred that the growth direction of PE spherulite thin films is predominantly determined by a specific crystal plane, such as {110} and {200}. Nonetheless, further experimentation is required to substantiate these findings and draw a definitive conclusion.

Consequently, the growth direction of PCL spherulites aligns with its [1-10] crystal direction, and the dendritic-like growth pattern leads to disruptions in the contrast of HAADF images and azimuthal orientation.

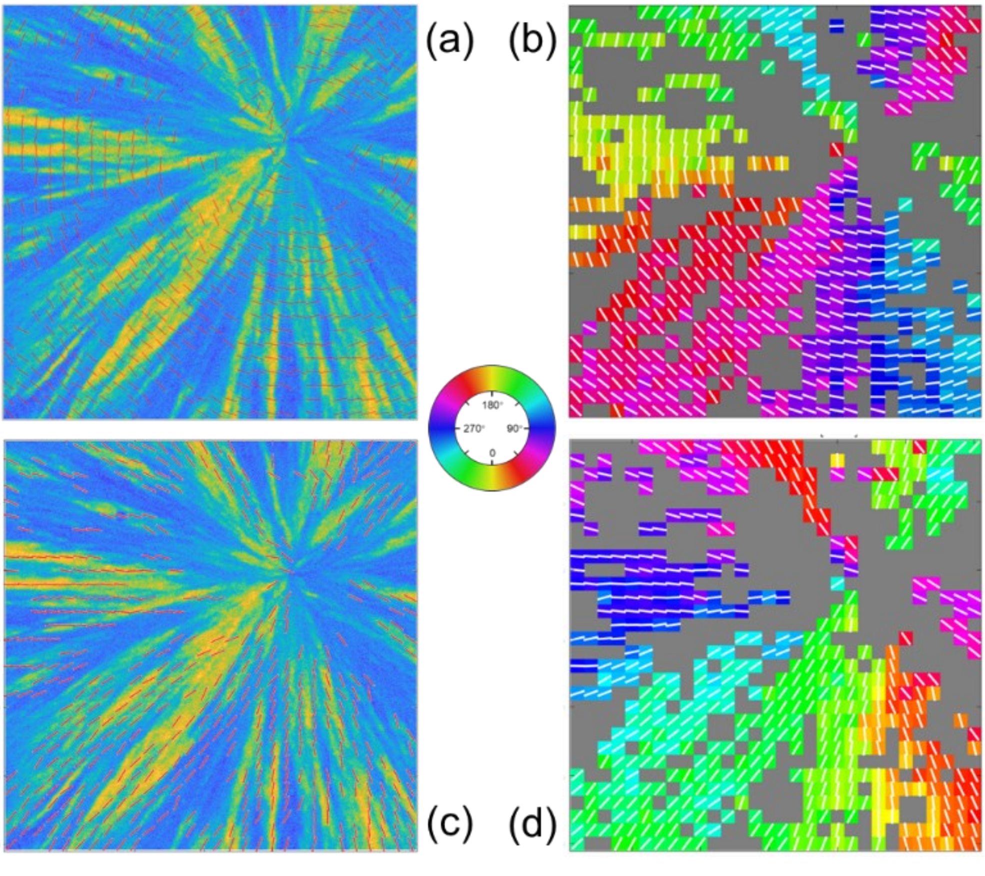

**Figure 3.9.** HAADF image of the detecting area of PCL (a, c) and its Orientation map of the normal of the (1-10) crystal plane (b) and the [1-10] crystal direction (d). Red short lines overlapped in (a) and (c) represent the local orientation from (b) and (f), showing a relevance between strong-scatter regions and {1-10} diffraction-observable regions. The orientation map shows a centrosymmetric discrete structure without extinction band. The color wheel representing the relationship between angles and colors. The blank positions represent that the diffraction is absent or missed due to technical reasons.

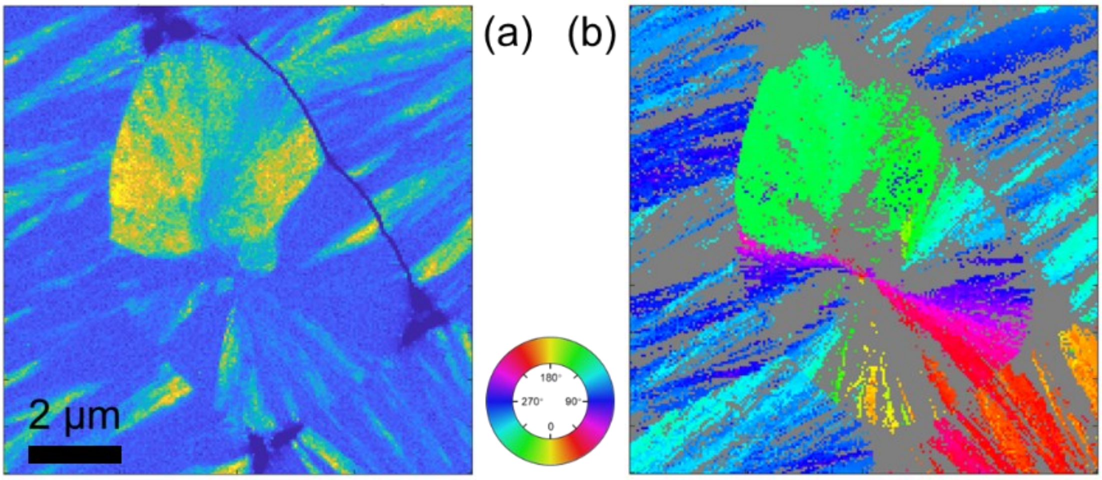

**Figure 3.10.** ADF image (a) and its orientation map (b) of a PCL spherulite acquired at a Spectra 300 showing a similar result to that in **Figure 3.8**.

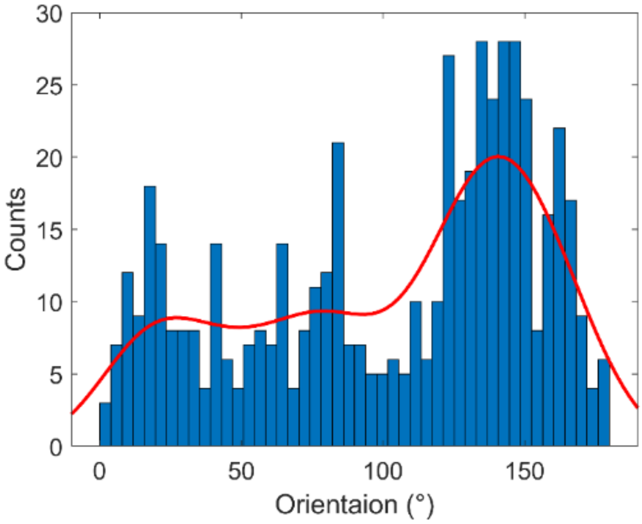

**Figure 3.11.** Distribution histogram of growth directions from **Figure 3.8d**.

## 3.4 Phase map

In Chapter 2, we extensively examined the electron-induced damage mechanisms in both crystalline and amorphous phases, which follow distinct pathways. Utilizing a similar approach, the differentiation between crystalline phases and the amorphous phase can be achieved by analyzing the diffraction patterns in 4D datasets. This involves transforming the 2D images into 1D profiles, as illustrated in **Figure 2.2**. The phase mappings of both PE and PCL were obtained using a Spectra 300 system equipped with a EMPAD at room temperature.

### 3.4.1 PE phase map

In order to validate the viability of phase identification, a region encompassing both electron-damaged PE and pristine intact PE was examined. The ADF image of this region is presented in **Figure 3.12**. This image was generated by summing the counts within a virtual aperture, defined by an inner radius of 2.5 mrad and an outer radius of 4 mrad. It exhibits a blurred region at the center, correlating to the damaged region. Furthermore, the radial-averaged intensity profiles derived from the complete set of diffraction patterns demonstrate mild damage, characterized by a weakening of the (200) peak and its partial overlap with the (110) peak. Meanwhile, the (020) peak, positioned around 4 $nm^{-1}$, remains unaffected. This observed electron damage aligns with the discussions presented in Chapter 2 and is equivalent to an approximate illuminated dose of ~0.3 e/Å$^2$ at room temperature, and a dose of ~3 e/Å$^2$ at 98K. This value is in accordance with our irradiated dose (~0.4 e/Å$^2$).

Furthermore, to quantify the components in local regions, the same methodology for estimating the phases was applied to each position. **Figure 3.13** displays the intensity distribution of the (110) crystalline component, (200) crystalline component, and amorphous components, and their overlapped image. From these images, the damaged region reveals a low crystalline intensity for both (110) and (200) and a high amorphous intensity, confirming the effectiveness of phase mapping. Moreover, the intensity mapping for crystalline intensity in **Figure 3.13a, b** presents a series of concentric ring, namely the extinction bands, resulting from the twisting of lamella.

In PE spherulites, there is no apparent separation between the amorphous and crystalline phases, although slight variations can occur due to the extinction band. However, an interesting result emerges, wherein different crystalline components such as (110), (200), and (020) exhibit different intensity maps, implying local structural changes. **Figure 3.14** presents the ADF image and the intensity maps of (110), (200), and (020) crystalline phases. The intensity maps of (110) and (200) display a concentric-ring texture, albeit with lower contrast for (200), while the intensity map of (020) exhibits a radial texture from the core extending across the entire region. These findings suggest that (110) and (200) possess a local tilt, or twist, while (020) remains fixed, which means a crystallographic rotation around the b axis.

To further substantiate this hypothesis, 4D datasets at same region were acquired through a tilting procedure in the low-dose mode, with a dose of approximately 0.1 e/Å$^2$, to mitigate multiple irradiating beam damage. The tilting angles, relative to the initial zone axis (the normal of the thin films), were applied in the x and y axes as follows: (15, 15), (-15, -15), (15, -15), and (-15, 15) in degrees, respectively. The intensity maps of the (020) and (110) crystal planes obtained from this tilting series are showcased in **Figure 3.15**.

Remarkably, in the tilting series, all the intensity maps of the (110) crystal planes exhibit a concentric-ring structure. This observation suggests the existence of concentric rings composed of (110) crystal planes that always align parallel to the beam direction. This pattern arises due to the interior continuous rotation along the radial direction. Conversely, the intensity maps of the (020) crystal plane consistently display contrast variations in accordance with the tilting rule. In different tilt configurations, the diffraction information from the (020) crystal plane disappears in different diagonal regions. This implies that the (020) planes are parallel to the normal of the thin films and remain unaffected by the crystal twist along the radial direction. These findings provide compelling evidence for a twist occurring around the crystallographic b axis. Importantly, our results demonstrate significant structural changes at a macroscopic scale, supporting the validity of our speculation.

Moreover, despite no separation of amorphous phase or crystalline phases, there is a decreased ratio of amorphous component to crystalline components from the core to the periphery and periodic fluctuation caused by the extinction bands, as shown in **Figure 3.16**. The trend is consistent to current accepted nucleation theory and other measurement.

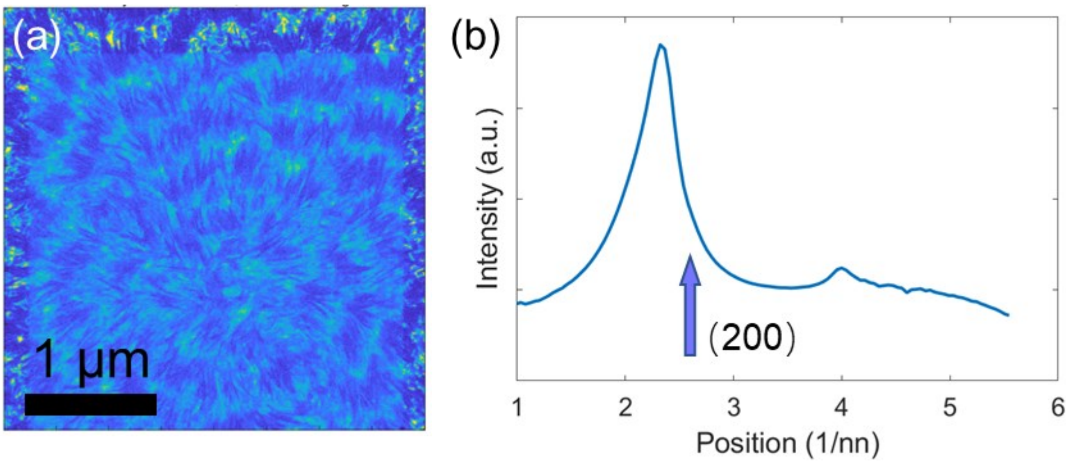

**Figure 3.12.** (a) ADF image of acquiring region. (b) Radial-averaged intensity profiles from the superposition of all diffraction patterns showing a mild electron damage.

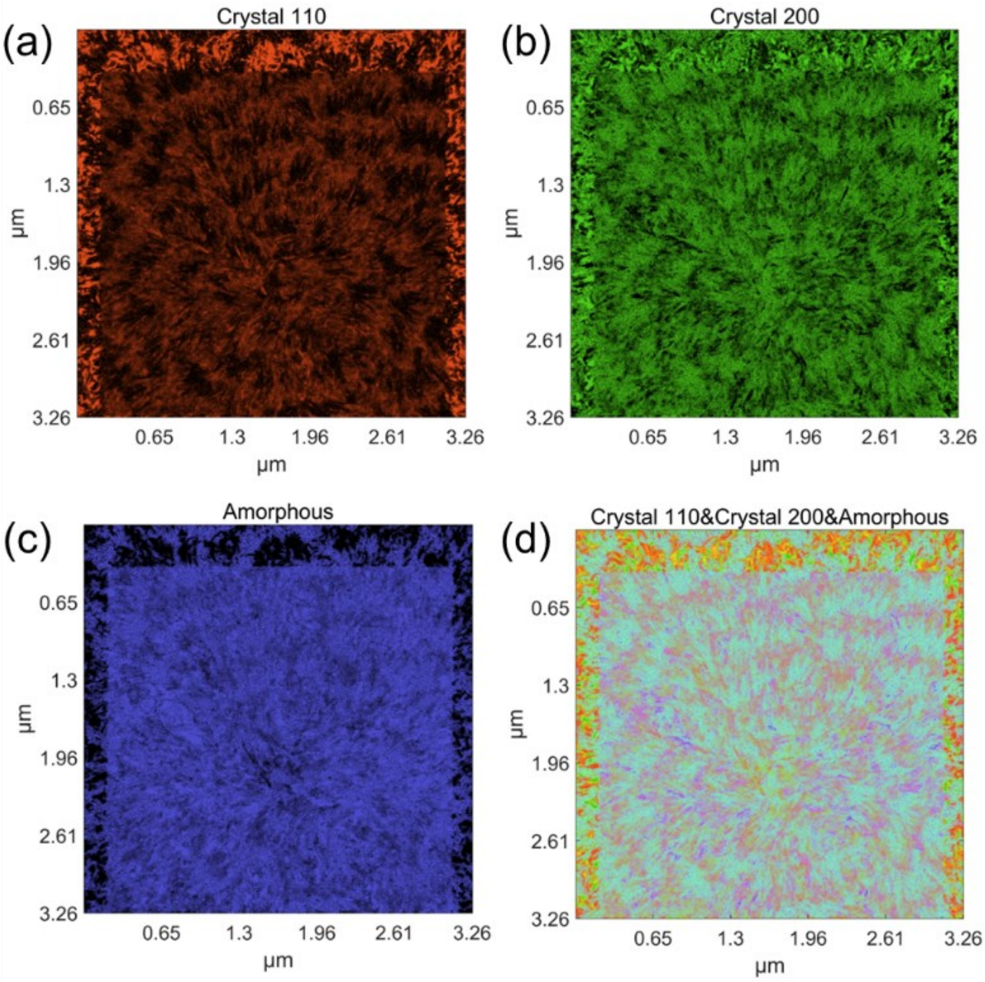

**Figure 3.13.** Intensity map of PE (110) crystalline component (a), (200) crystalline component (b), amorphous components, and their overlap (d). The margin is intact PE thus showing a high intensity in crystalline components, while the center is damaged showing a high amorphous intensity.

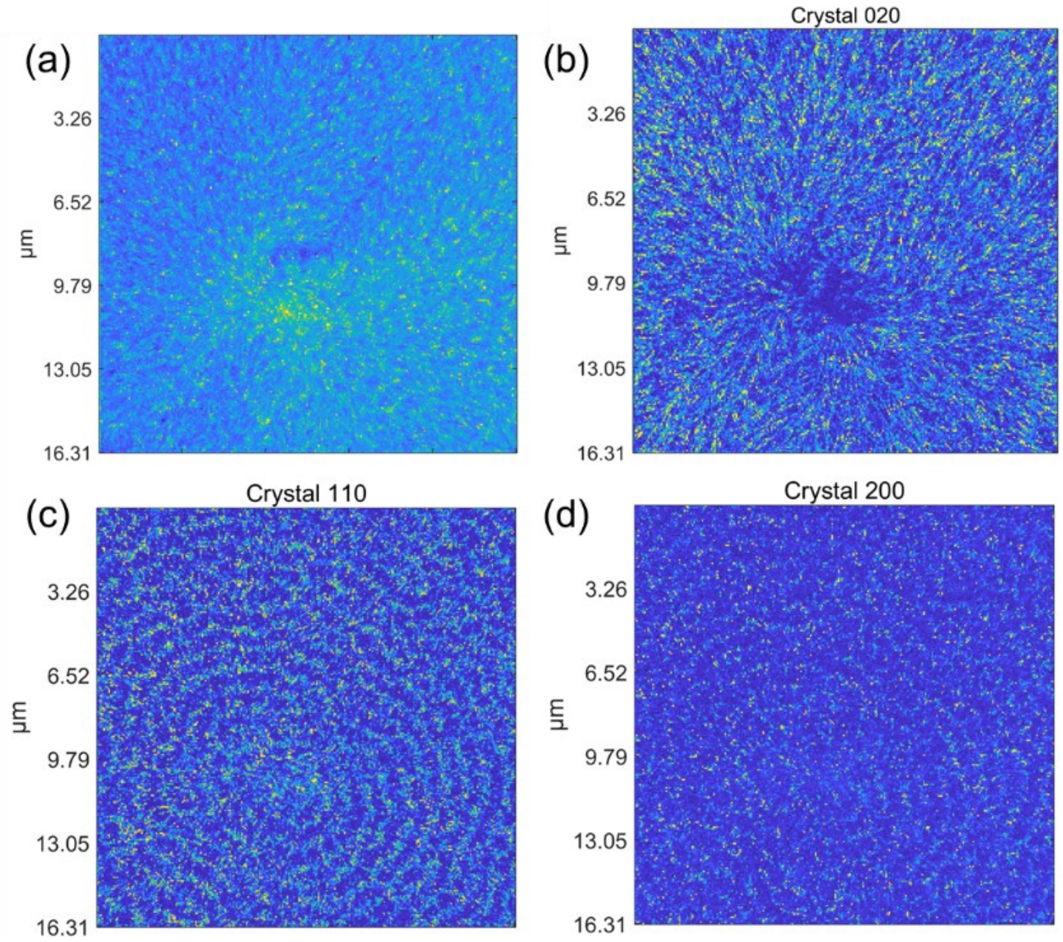

**Figure 3.14.** ADF images (a), and intensity map of (020) crystalline component (b), (110) crystalline component (c), and (200) crystalline components (d) at a zone axis of [001].

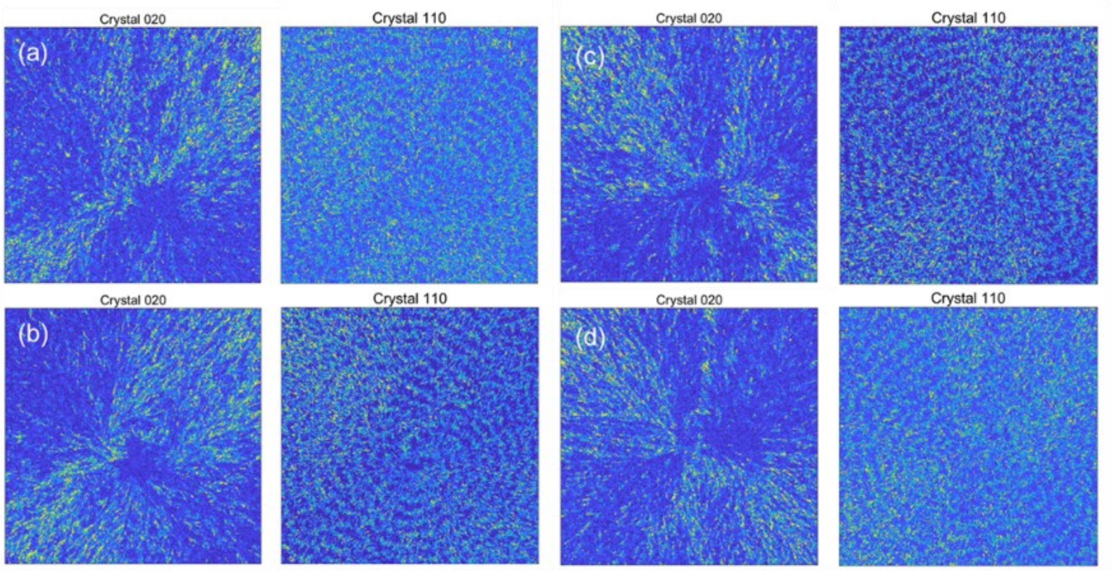

**Figure 3.15.** Intensity maps of (020) (Left) and (110) (Right) with tilting angles from (15, 15), (-15, -15), (15, -15), and (-15, 15) for (a-d) respectively.

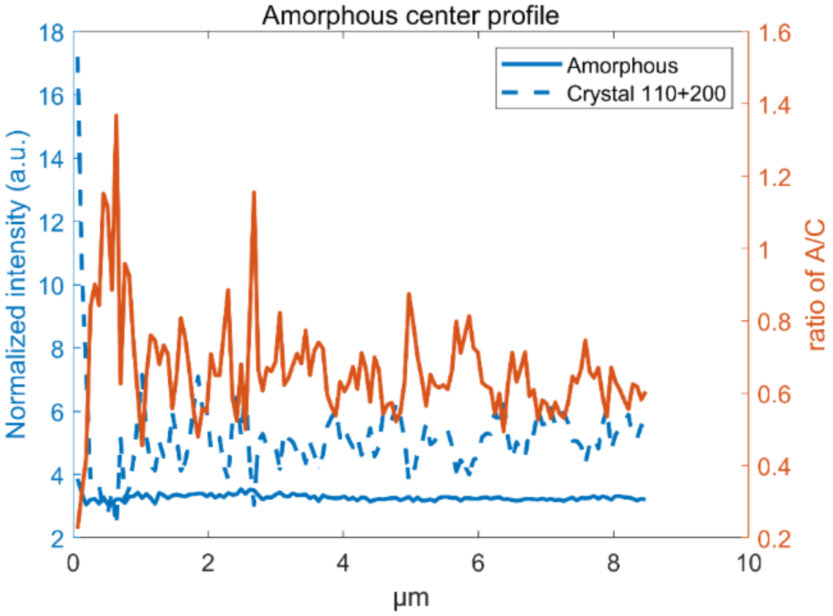

**Figure 3.16.** Intensity profiles of PE amorphous phase (blue solid line) and crystalline phases (blue dash line) composed of (110) and (200) and ratio profiles, and their ratio from core to peripheral obtained from the results in **Figure 3.14**.

### 3.4.2 PCL phase map

PCL spherulites possess a comparatively straightforward microstructure without local twist. This simple microstructure is evident in the phase maps, as illustrated in **Figure 3.17**, which clearly display distinct phase separation. Specifically, the intensity map of the amorphous phase is essentially complementary to those of the crystallographic (110) and (200) planes. Moreover, there is a notable decrease in the ratio of the amorphous component to the crystalline components from the core to the periphery of the spherulites, as depicted in **Figure 3.18**. These findings provide robust evidence for the existence of phase separation within PCL spherulites.

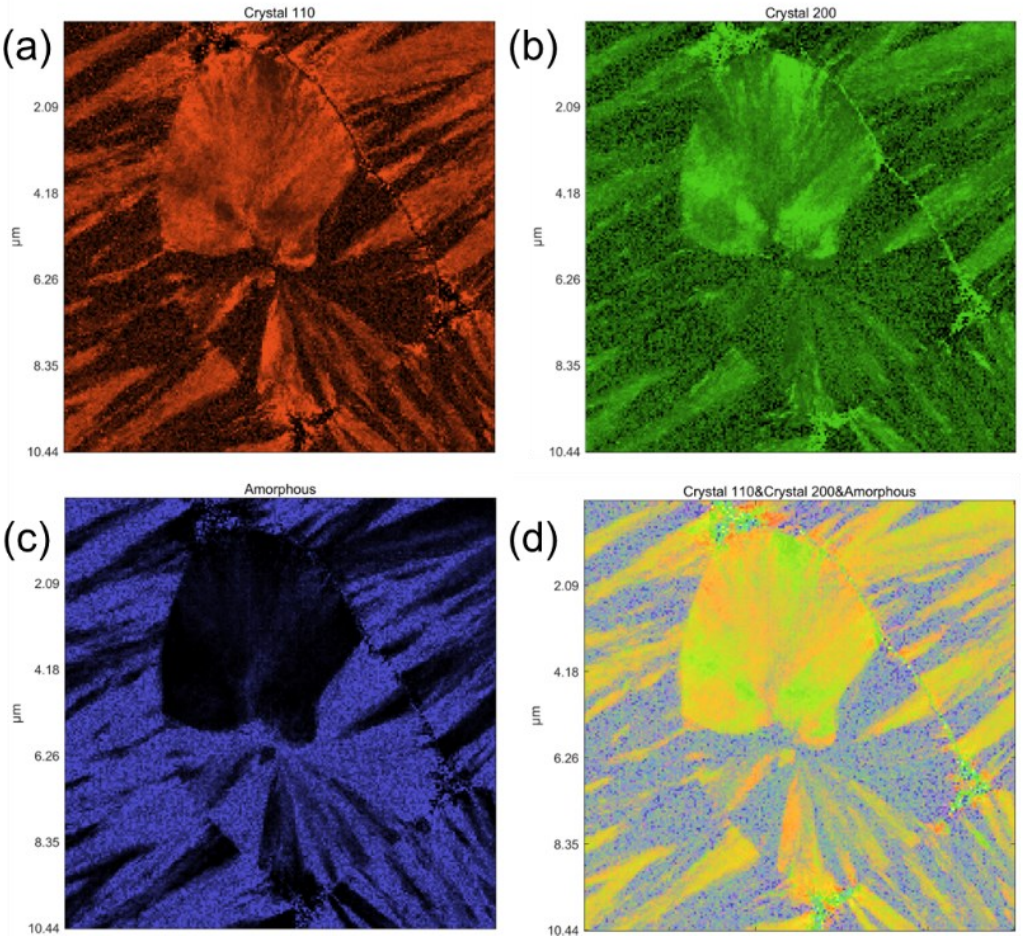

**Figure 3.17.** Intensity map of PCL (110) crystalline component (a), (200) crystalline component (b), amorphous components, and their overlap (d) which are acquired from the same region in **Figure 3.9**.

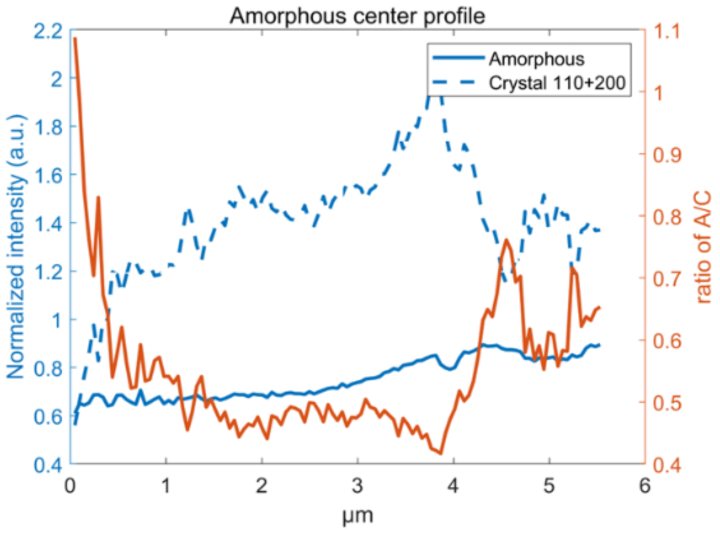

**Figure 3.18.** Intensity profiles of PCL amorphous phase (blue solid line) and crystalline phases (blue dash line) composed of (110) and (200) and ratio profiles, and their ratio from core to peripheral obtained from the results in **Figure 3.17**.

## 3.5 Conclusion

In summary, we have optimized the acquiring condition for 4D-STEM datasets which contains the information of orientation and phases with resolution down to ten nanometers. The microstructures with circular symmetry in PE and PCL are explicitly demonstrated.

PE shows lamellae twists around the crystallographic b axis, a growth direction along [1-10] in the radial direction, and a continuous orientation over the polar angle direction. Therefore, PE spherulites homogeneously extend outward from their cores with a twist of crystal structure. Although our PE samples are relatively homogeneous in degree of crystallinity, the mapping ability for crystalline and amorphous component can be confirmed by using beam irradiation regions.

PCL spherulites without local twist also have a growth direction along [1-10] outward, while in azimuths, a radial pattern is separate by amorphous gap resulting from the inhomogeneous crystallinity which is verified by phase mapping. Additionally, results for PCL and PE also uncover the increase of crystallinity from crystalline cores to peripheries same as the previous reported.

Hence, our recently developed technology utilizing the 4D-STEM system showcases great potential in uncovering local information. Additional research is also necessary to fully understand and exploit its capabilities.

# Chapter 4 Quantitative plasmon for 2D $In_2Se_3$ phase identification at nanoscale

## 4.1 Introduction

As stated in Chapter 1.4, 2D materials with competing polymorphs offer remarkable potential to switch the associated 2D functionalities for novel device applications. Probing their phase transition and competition mechanisms requires nanoscale characterization techniques that can sensitively detect the nucleation of secondary phases down to single-layer thickness.

In this chapter, we demonstrate nanoscale phase identification on 2D $In_2Se_3$ polymorphs, utilizing their distinct plasmon energies that can be distinguished by EEL spectra. *In situ* EELS experiments are conducted for excluding possible interferential factors, such as surface contamination, measurement conditions, and post-processing, which thus explicitly reveal the distinction between $\alpha/\beta'$ phases. Moreover, correlating with in situ X-ray diffraction, we further reveal a subtle difference in the valence electron density of $In_2Se_3$ polymorphs underpinned by their electronic structure. The characteristic plasmon energies and valence electron of $In_2Se_3$ polymorphs have been explicitly validated using first-principles calculations and can be attributed to their different band structures. The nanometer resolution and independence of orientation thus make plasmon-energy mapping a versatile technique for nanoscale phase identification on 2D materials.

## 4.2 Methods

### 4.2.1 Materials

**Plane TEM samples:** $\alpha$-$In_2Se_3$ thin flakes were exfoliated from bulk $\alpha$-$In_2Se_3$ (purchased from HQ Graphene) and $\beta'$-$In_2Se_3$ were obtained by annealing the exfoliated $\alpha$-$In_2Se_3$ thin flakes from 300°C to room temperature. The $In_2Se_3$ thin flakes were sonicated in high-purity ethanol and then the dispersed nanoflakes were dropped cast onto holey carbon-coated Cu grids or heating chips for TEM/EELS measurement.

**Cross-sectional TEM samples:** The cross-sectional samples were prepared from the exfoliated $In_2Se_3$ flakes by using a ThermoFisher Helios 5CX dual-beam focused ion beam/scanning electron microscope (FIB-SEM) followed by *ex situ* lift-out onto half Cu grids. The intergrowing $\alpha/\beta'$ $In_2Se_3$ were from flakes that was synthesized through chemical vapor deposition (CVD). The raw materials employed in the synthesis were Se and $In_2O_3$ powders, positioned in separate quartz boats within a dual temperature zone tube furnace. The Se source was placed upstream while maintaining a gas flow of 10% $H_2$/Ar with a flow rate of ~20 sccm. Subsequently, the Se and $In_2O_3$ powders were heated to 270 and 680 °C, respectively, and held for ~30 minutes, during which thin $In_2Se_3$ flakes were deposited onto mica substrates placed above the $In_2O_3$ powders. Following the deposition, the tube furnace was allowed to naturally cool down to room temperature. The observed mixture of phases is uncommon, warranting further investigation to identify the underlying causal factors.

**Plane $\alpha/\beta'$ mixed samples:** These samples were induced from $\alpha$2H-$In_2Se_3$ flakes by electron beam at cryogenic condition. The $\alpha$2H-$In_2Se_3$ is prepared as described above, and they were mounted on a liquid-nitrogen cooling holder (Gatan, model 636) to lower temperature down to 98 K for lowering the effects of electron beam. Until the holder stable, using a focused electron beam to illuminate the selected $\alpha$-$In_2Se_3$ about 2 min which can transfer the illuminated $\alpha$ phase into $\beta'$ phase. The phase transfer is confirmed by SAED (not shown in the thesis) and STEM images (see **Figure 4.4**).

**Samples for Raman spectra and XRD:** The samples for Raman spectra were prepared by mechanical exfoliation from bulk $In_2Se_3$ and tape transfer onto silicon substrates. The ground $In_2Se_3$ powder were used for XRD measurement.

### 4.2.2 Characterization

**Raman spectra** were acquired on a Witec alpha 300R confocal Raman microscopy with a 532 nm exciting laser. **X-ray diffraction**: XRD were performed on a Rigaku X-ray diffractometer (SmartLab 9kW) equipped with an Anton Paar TTK 600 low temperature chamber for temperature-change experiments. ***In situ* XRD**: The powders of 2H/3R $\alpha$-$In_2Se_3$ in vacuum are first heated up to 350 °C from 25 °C, and then back to 25 °C with a rate of 10 °C/min. The lattice parameters were calculated by Rietveld refinement using least square weighting model assisted with multi-peaks fitting based on the XRD data. The raw data subtracted background are exhibited in **Figure 4.7**.

**HAADF-STEM characterization** was performed on a ThermoFisher Scientific Spectra 300 equipped with an X-FEG/UltiMono electron source and a CEOS SCORR fifth-order probe corrector, operated at 300 kV. A convergence angle of 29.9 mrad, a collection angle of 45–200 mrad, and a dwell time of 2 μs were used for atomic-resolution HAADF-STEM imaging unless otherwise noted.

**EELS-STEM characterization** was conducted using either the ThermoFisher Scientific Spectra 300 operated at 300 kV equipped with a GIF Continuum K3 System or the JEOL JEM-2100F microscope operated at 200 kV equipped with a Gatan Enfina electron spectrometer. EEL spectra and mapping were acquired in STEM mode with an FWHM of ~0.9 eV in ZLP, using a convergence angle of 13 mrad and a collection angle of 9 mrad to optimize the probe conditions. EEL spectra were acquired with a dispersion of 0.05 eV/channel in the low-loss area. Prior to measurement, all samples were mildly cleaned using plasma cleaner and heated on a 60 °C hot plate over 30 minutes to eliminate the effects of carbon contamination. Furthermore, pretests of EELS carbon ionization edge were carried out to ensure no carbon deposition. EEL spectra and mapping in this work were acquired from the $In_2Se_3$ nanoflakes with similar thickness (~0.5 $\lambda$) calculated by the log-ratio method of inelastic scattering electron. Besides, to avoid effects of interfacial defects, EELS maps were acquired before atomic-resolution STEM images, and an electron probe of low current (~20pA) with a 0.05 s dwell time and 20% live time was used. For a 32x32 EELS map over a region of 20 $nm^2$, the accumulating dose is ~ 8000 e/$Å^2$ which cause only minor damage. This probe conditions helps minimize damage and avoid the interference from the interfacial defects.

***In situ* heating/cooling EELS-STEM experiments** were carried out on commercially available, calibrated MEMS-style TEM heating chips (Protochips Fusion) with $SiN_x$ substrates. Prior to acquirement, the holder was initially heated to 80 °C to eliminate contamination. During the experiments, the sample temperature was first increased to 350 °C and then back to 25 °C maintaining at a temperature change rate of 10 °C/min. Moreover, temperature loops between 25 °C and 200 °C for $\alpha$ phases and loops 25 °C and 350 °C for $\beta'$ phases were also conducted to exclude the effects of heating/cooling hysteresis and stress relaxation under phase changes shown in **Figure A2** and **A3**.

### 4.2.3 Data analysis

**Quantitative Analysis**: Raw spectra are firstly aligned in loss energy by ZLP, and a Fourier-log algorithm is executed to remove the ZLP and deconvolute the effect of underlying multiple scattering. Subsequently, spectra are fitted by least-square method with a Lorentz-peak model to quantify the maximum of plasmon peaks. An example of fitting EEL spectra from *in situ* experiments is shown in **Figure 4.1**, and its model is described by **Equation (4.1)**.

$$I = \frac{a_1 c_1^2}{(x-\epsilon_1)^2 + c_1^2} + \frac{a_2 c_2^2}{(x-\epsilon_2)^2 + c_2^2} + \frac{a_3 c_3^2}{(x-\epsilon_3)^2 + c_3^2} + dx + e \tag{4.1}$$

In **Equation (4.1)**, the first three terms represent the first and second plasmon peaks of $In_2Se_3$ and an alternative plasmon peak originating from $SiN_x$ substrates used in our *in situ* experiments. The latter two terms account for the background signal arising from dark noise, weak 4d-orbit ionization, and the tail of electron transition loss. It is important to note that between the ZLP and the plasmon peaks, there exist numerous signals that are difficult to define precisely, including interband transitions, core-level excitations, phonons, and other collective excitations. These signals impose challenges in establishing a reasonable modeling of the EEL spectra and are therefore excluded from our fitting model.

To enhance the accuracy of our fitting, we acquired EELS map to reduce the effect of shot noise (Poisson) from random distribution of scattering and detector noise (Gaussian), and EEL spectra of $SiN_x$ are also acquired as a reference to reduce the uncertainty of fitting. Due to the high intensity of $SiN_x$ signals, the second plasmon peak of $In_2Se_3$ is entirely masked with a large confidence interval in fitting results. Thus, the position of the second plasmon peak for in situ EELS measurement is not discussed in the thesis. Overall, our fitting approach yields robust results, with $R^2$ values larger than 98% for all the obtained results. Moreover, the errors shown in this chapter are the half widths of 95% confidence interval. It is also noted the plasmon peaks can affected mutually and their positions are linked to their intensity. So, we use maximum plasmon energy, namely the fitting peak position, to demonstrate the differences.

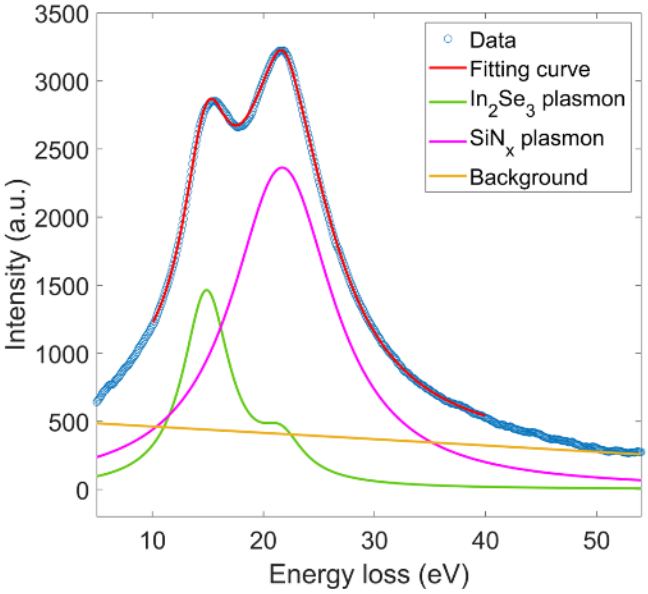

**Figure 4.1.** Curve fitting for a ZLP-deconvoluted valence EELS of $\alpha$2H $In_2Se_3$ on $SiN_x$ substrate with a fitting range from 10 to 40 eV.

### 4.2.4 First-principles calculation

The first-principles calculations in this work were conducted by Dai, Minzhi and Luo, Xin from Sun Yat-Sen University. Geometry relaxation and electronic properties calculations are performed using density function theory (DFT) within the local density approximation (LDA) for the exchange and correlation energy functional, as implemented in the Vienna ab initio simulation package (VASP). The projector-augmented wave (PAW) method is used to describe the interactions between ions and electrons of Indium ($4d^{10}5s^25p^1$) and Selenide ($4s^24p^4$) and the cutoff energy for plane-wave expansion is set to be 500 eV. The I-center k-point sampling grids are chosen as 9x9xl and 13x13x2 for geometry relaxation and self-consistent calculations respectively. The geometry of the $\alpha 2H$, $\alpha 3R$, $\beta 2H$, and $\beta 3R$ In2Se3 bulks have been fully optimized until the energy converge accuracy within $10^{-5}$ eV and the forces of all atoms decrease below 0.001eV/ Å. To get the energy loss function, we calculate the frequency dependent dielectric matrix after the electronic ground state has been determined.

## 4.3 Phases identification by plasmon energies

### 4.3.1 Verification of phases

**Figure 4.2** exhibits low-frequency Raman spectra, XRD, and valence EEL spectra along <0001> (solid lines) and <$11\bar{2}0$> (dot lines) to fully confirm the four phases of $In_2Se_3$ ($\alpha 2H$, $\alpha 3R$, $\beta' 2H$, and $\beta' 3R$ from top to bottom). **Figure 4.2a** shows characteristic Raman peaks as the labels [86,141], and **Figure 4.2b** demonstrates different symmetry and lattice parameters by XRD, where $\beta'$ phases exhibit a distinct peak splitting in $\{11\bar{2}0\}$. As demonstrated in **Figure 1.9**, STEM images explicitly reveal that α phases are composed of one six-coordinated Indium atom and one four-coordinated Indium atom, while $\beta'$ phases consist of two six-coordinated Indium atoms, exactly as their atomic models in **Figure 1.9b, c**. The results of STEM, Raman, and XRD are coherent and in congruence with the previous reports [72,76,86,86,93,142-144], which thus verify the phase of our samples with high phase purity.

Valence EEL spectra in the two zone axes reveal an uncommon dual-plasmon peak shape as demonstrated in **Figure 4.2c**, comprising two peaks around 15 eV and 21 eV with FWHM of ~ 6.7 and 7.9 eV. The spectra along <0001> show a bump at 3-12 eV relative to those along <$11\bar{2}0$>, corresponding to increased energy loss in the ultraviolet band. Additionally, one consistent phenomenon is observed in the optical property for $In_2Se_3$ that the stronger absorption coefficient occurs when the light polarization is along the <0001> direction relative to that vertical to the <0001> direction [145]. Noted due to the limitation of the EELS collecting aperture, when electron beam is along <0001>, the energy-loss electrons with k vectors parallel to the a*b* plane are cut off by the aperture while k vectors along c* are almost collected, and vice versa.

Moreover, there is a subtle shift in the maximums of first plasmon energy. **Table 1** list the first-plasmon energies which follows the trend of $\alpha 2H < \alpha 3R < \beta' 2H < \beta' 3R$ at both <0001> and <11$\bar{2}$0> directions. Although the shifts are small (~ 0.3 eV and ~ 0.15 eV between $\beta'$ and $\alpha$ at <0001> and <11$\bar{2}$0>), it is enough to identify and map phases. Thus, the distinction is the base for 2D $In_2Se_3$ phase identification at nanoscale.

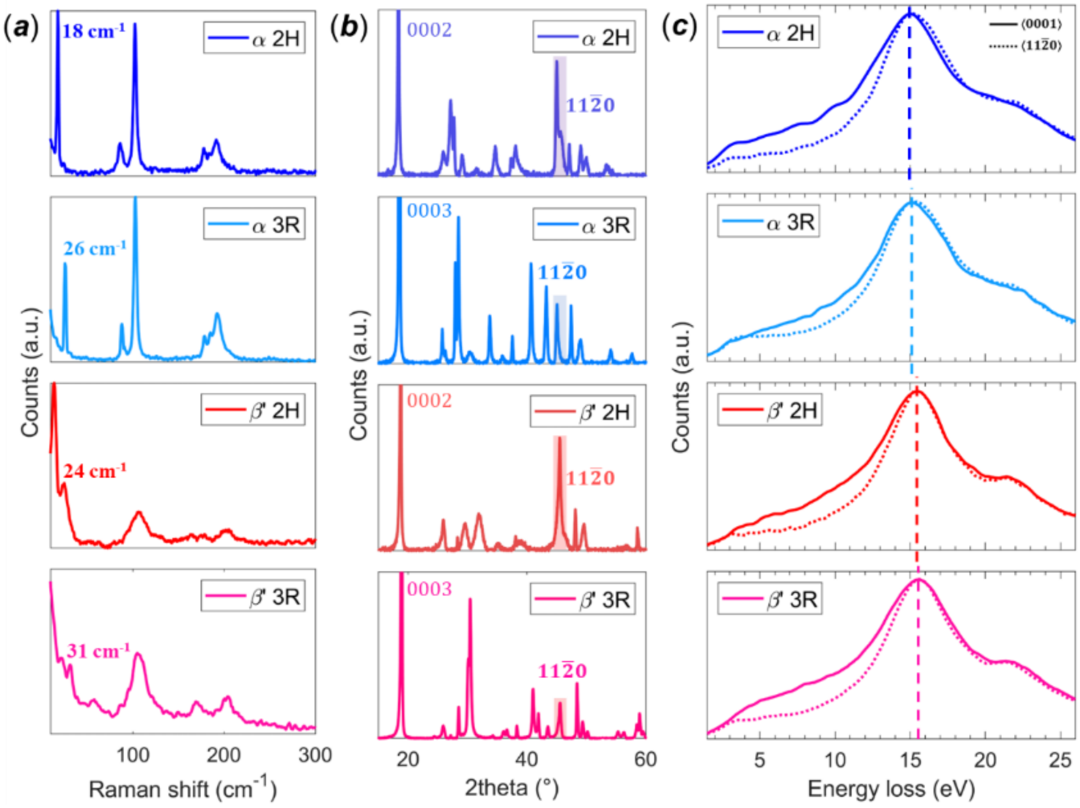

**Figure 4.2.** (a) Raman spectra for four $In_2Se_3$ with their characteristic low-frequency Raman shifts. (b) Powder X-ray diffraction of four $In_2Se_3$ at room temperature with labels of lattice planes, quintuple planes (0002)/ (0003) and in-plane $\{11\bar{2}0\}$; insets: the larger versions for $\{11\bar{2}0\}$ peaks. (c) Low loss EEL spectra of four $In_2Se_3$ along <0001> and $<11\bar{2}0>$ zone axes (solid and dot lines) with dash-dot lines for their plasmon energy.

**Table 4.** The first plasmon peak maximum energy position of the four phases of $In_2Se_3$ along <0001> and $<11\bar{2}0>$ zone axis at room temperature. Errors are the 95% confidence interval half widths.

| Energy (eV) | $\alpha 2H$ | $\alpha 3R$ | $\beta' 2H$ | $\beta' 3R$ |
|---|---|---|---|---|
| 1st along <0001> | 14.93(3) | 15.08(5) | 15.28(5) | 15.43(3) |
| 1st along $<11\bar{2}0>$ | 15.26(2) | 15.31(3) | 15.39(3) | 15.45(2) |

### 4.3.1 $In_2Se_3$ phase identification by EELS mapping

**Figure 4.3a** depicts a low-magnification STEM image of the intergrown $\alpha/\beta'$ $In_2Se_3$ sample, with a few $\beta'$ layers (the light belts) inserted in the $\alpha$ matrix and cross the whole sample. The slight strong HAADF intensity could result from the slight dense atoms arrangement in $\beta'$ phases whose volumes are listed in **Table 5**. In **Appendix A.3**, we discuss the STEM images of $\alpha/\beta'$ intergrowing samples acquired from different collection angles which offer further insights and support for this point.

**Figure 4.3b, c** exactly show the HAADF image and its comparison to the atomic model, providing a verification of the coexistence of the two phases. More importantly, EELS mapping acquired at 200kV in **Figure 4.3d** reveals a plateau of plasmon energy corresponding to the five-quintuple-layer region of $\beta'$ of ~ 5 nm width in **Figure 4.3c**, and the values of plasmon energies is close to that measured in single-phase samples. The atomically sharp $\alpha/\beta'$ interfaces become ~1.1 nm wide as revealed by the energy profile in Fig. 2(c), indicating the resolution of $E_p$ mapping to be ~1.1 nm that should be limited by the delocalization of the low-loss EELS signal [98,146,147]. The estimation of resolution of plasmon signal is further discussed in **Appendix A.4**. Although not comparable to TEM/STEM imaging, this resolution is still sufficient to detect the thinnest intergrowth, i.e., single-quintuple-layer $In_2Se_3$ (~1.0 nm wide), and another EELS mapping for two quintuple-layer $In_2Se_3$ is demonstrated in **Figure A.2**.

Besides cross-sectional $In_2Se_3$ phase identification at nanoscale, we have also conducted the phase identification of plasmon on plane $In_2Se_3$ samples for large FOV up ~ 280nm. **Figure 4.4** showcases the effective phase identification of $\alpha/\beta'$, where $\beta'$(2H) exhibits a stronger plasmon energy at a sub-micrometer scale. It is worth noting that the irregular shape of the β' phase is caused by the induced method described in Chapter 4.2.1. However, despite this irregular shape, it generally aligns with the irradiation area caused by a circular parallel electron beam. **Figure 4.4a, f** shows the irradiation area with an obvious surface damage, and **Figure 4.4e** presents a referenced image obtained by masking the characteristic superstructure satellite peaks in its Fourier transfer of **Figure 4.4a**.

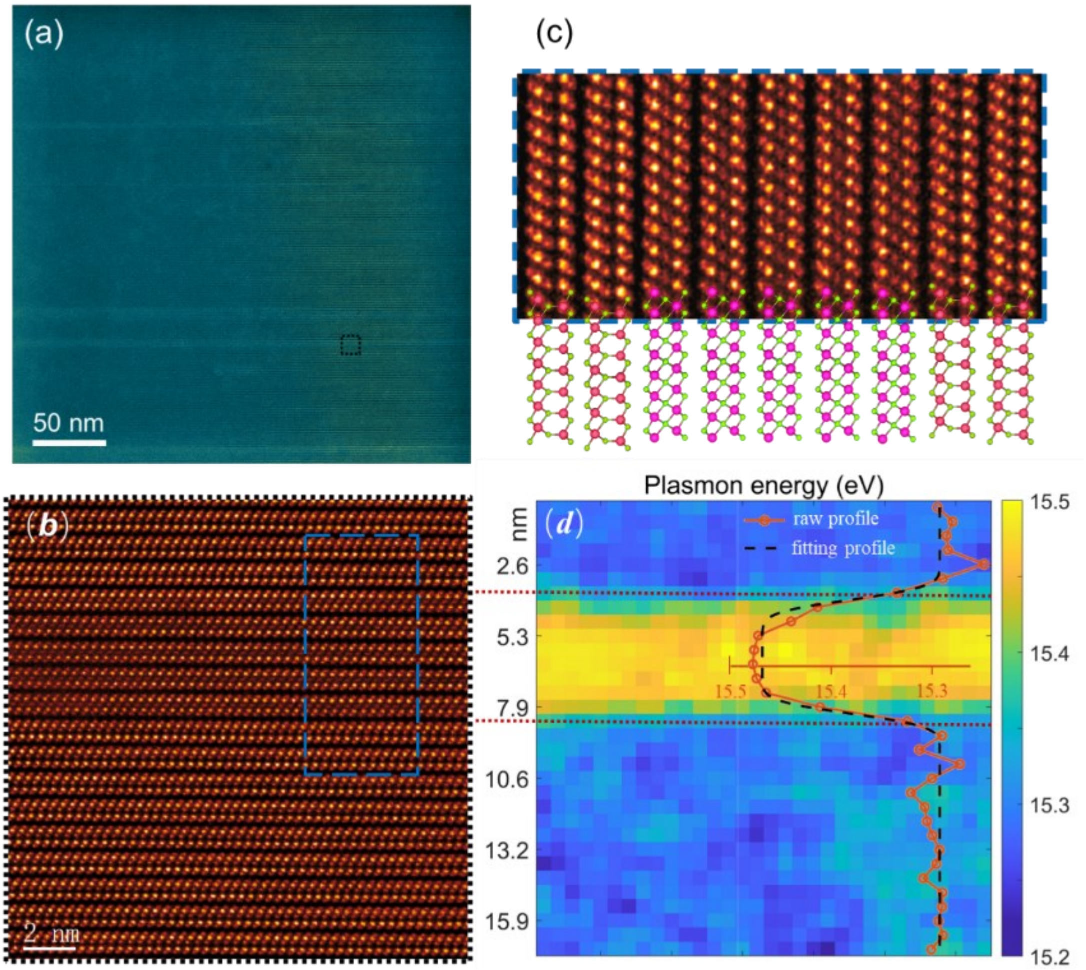

**Figure 4.3.** (a) Low-magnification image of $\alpha/\beta'$ intergrowing $In_2Se_3$ with a few $\beta'$ layers (region brighter) crossing the whole FIB sample. (b) HAADF image of five quintuple layers of $\beta'$ phase inserted in the $\alpha 3R$ main body, FOV corresponding the black square in (a). (c) Larger versions of the blue rectangle region in (b) and the atomic models. (d) EELS maximum plasmon energy map of the region of (b) and its raw (red) and fitting (black dash) energy profiles, acquired at 200 kV of Jeol 2100F where the $\beta'$ region reveals higher plasmon energy. For better visualization, a light Gaussian smoothing with a standard deviation of 0.4 is applied only in the EELS mapping.

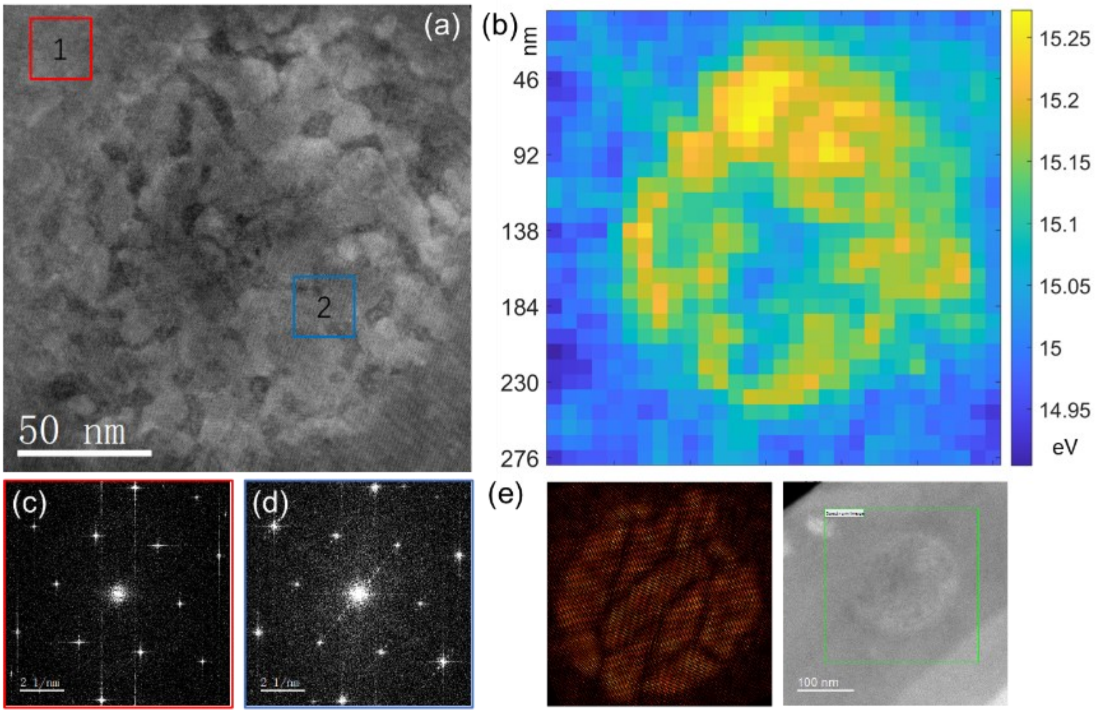

**Figure 4.4.** (a) Low-magnification image of $\alpha/\beta'$ mixture $In_2Se_3$ where $\beta'$ phase is induced by local heating effects of electron irradiation thus showing a surface damage. (b) EELS maximum plasmon energy map of the region of (a) where the region of higher plasmon energy is $\beta'$ phase generally as the irradiation area and the region showing obvious superstructure in (c). For better visualization, a light Gaussian smoothing with a standard deviation of 0.7 is applied. (c, d) Selected-area Fourier transfer of two regions in (a) showing the separation of $\alpha$ (c) and $\beta'$ (d) phases, where (d) shows the satellite peaks from the superstructure. (e) Referenced image of $\beta'$phase obtained by masking the characteristic superstructure satellite peaks in the Fourier transfer of (a). (f) Low-magnification image acquired with EELS mapping showing the region with surface damage.

However, it is important to note that the electron beam-induced phase transition is confined in controllability. This can result in uneven surface damage and inhomogeneous phase transition, making it uncertain if the phase change has completely occurred throughout the cross-section. Therefore, more investigations are needed to fully comprehend the underlying mechanisms and optimize this method for reliable phase change.

## 4.4 Origins of plasmon energies

In the previous chapter, we have demonstrated the ability of plasmon for distinguish the $\alpha$ and $\beta'$ phases of $In_2Se_3$. However, the repeatability and robustness of the plasmon-based technology and the origins of the different plasmon energies still need more research.

### 4.4.1 Verification of $In_2Se_3$ EELS

To further validate the observed difference in the first plasmon energy and uncover its origin, we conducted *in situ* temperature-change experiments of EELS. In the experiment, common thermal expansion and the $\alpha \rightarrow \beta$ phase changes around 225 °C should occur. Besides, we also conducted temperature loops without phase change for $\beta'$ and $\alpha$ phases, to exclude the possible effects of heating/cooling hysteresis and latent stress relaxation under phase change (**Appendix A.5**). **Figure 4.5** presents the first plasmon maximum energy as a function of different temperatures for $\alpha 2H/\alpha 3R$ $In_2Se_3$ samples indicating three features: 1) negative linear correlations with temperature (fitting curves in **Figure 4.5**); 2) constant energy difference of ~ 0.3 eV between $\alpha/\beta'$ phases; 3) energy leaps induced by the phase transitions around 225 °C (also confirmed by SAED in **Figure 4.6**), despite slow occurrence within tens of °C probably due to the relaxation of thin thickness [149,153,154]. Thus, the repeatable results of *in situ* EELS explicitly reveal the difference of plasmon energies in $In_2Se_3$ four phases.

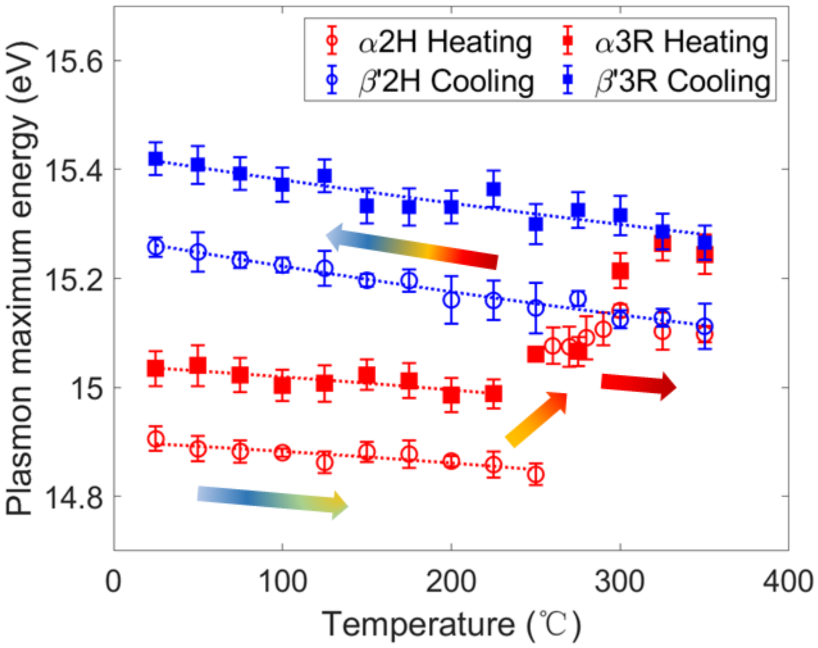

**Figure 4.5.** Plasmon maximum energy of four $In_2Se_3$ along <0001> as a function of different temperatures (arrows for the temperature change process), following a linear decrease as the fitted dot lines. Slow phase transitions occur around 250 °C and leads to the energy leaps. Error bars are the 95% confidence interval half widths.

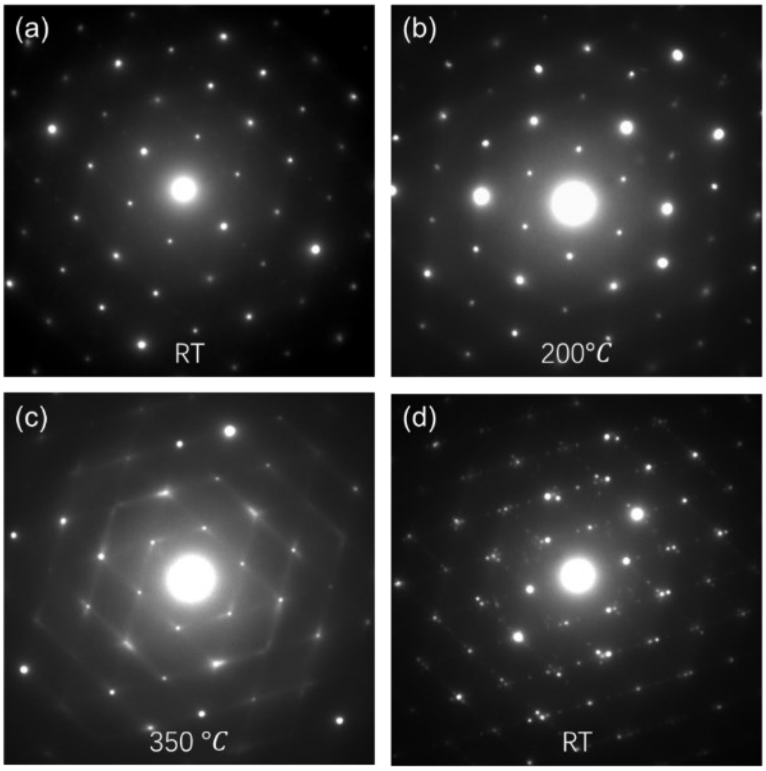

**Figure 4.6.** SAED patterns upon *in situ* heating process of $\alpha$3R $In_2Se_3$, at (a) RT, (b) 200 °C, (c) 350 °C, and back (f) RT, showing the features of $\alpha$, $\beta$, and $\beta'$.

### 4.4.2 Calculation of plasmon energy and valence electrons

The negative linear correlations of plasmon maximum energies with temperature is related in **Equation (1.3)** that $E_p(T) \propto \sqrt{n_0/V(T)}$ , and therefore the thermal expansion can lead to the shift of plasmon energy. However, the plasmon energy $E_p$ cannot be measured directly, and some modification must be applied to the measured plasmon peak $E_M$ to obtain the plasmon energy which follows the **Equation (4.2)** [98]:

$$E_p = \sqrt{E_M^2 + (\Delta E_p/2)^2 - (\hbar\omega_b)^2} \approx \sqrt{E_M^2 + (\Delta E_p/2)^2 - E_g^2} \qquad (4.2)$$

where $\Delta E_p$ is the FWMH of plasmon peaks and the $\hbar\omega_b$ is the binding energy of excitons usually slightly smaller than the band gap $E_g$. The $\Delta E_p$ and $E_g$ of four phases are close in value and almost constant. $\Delta E_p$ are about 6.7 eV for the first plasmon peak, and $E_g$ are recently reported as 1.45 (direct gap) for $\alpha$ phases [149,150] and 0.97 (indirect gap) for $\beta'$ phases [151,152]. Thus, plasmon energy $E_p$ is higher ~ 0.3 eV than the measured $E_M$. Although the correction is mathematical, it is important for the accurate valence electrons for tracing the source of plasmon energies. Consequently, another factor, valence electrons, to influence the plasmon energies is revealed.

By the *in situ* XRD measurement, the volumes of fours phase under different temperature can be obtained. **Figure 4.7** show the XRD patterns of four phases indicating the expansion with temperature increase. Their unit-cell volumes of single quintuple layer as a function of temperature by fitting XRD is demonstrated in **Figure 4.8**, following a linear decrease. Their volumes at 25 °C and volume thermal expansion coefficients (VTECs) are listed in **Table 5** consistent with the previous reports [76,143,144].

The volumes of $\alpha$ phases are greater by ~ 4 $Å^3$ than those in $\beta'$ phase, and the volumes of 2H ordering are greater by ~ 1 $Å^3$ than 3R ordering.

Based on the obtained volumes, the $n_0 = m_{eff} \times E_p^2\, V(T) \times (\hbar^2 e^2)/\epsilon_0$ can be derived. Although the exact value of $\boldsymbol{m_{eff}}$ is hard to be estimated, reasonable results can be obtained by following the convention, $\boldsymbol{m_{eff} = m_e}$ [98-100]. Moreover, it is noted that the valence electrons typically are the outer shell electrons, whereas in the case of plasma oscillations, a subset of valence electrons can also contribute to a plasmon, as observed in graphitized carbon where various types of electron orbits contribute to two plasmon peaks [98,155,156].

Therefore, the $n_0$ at different temperature can be depicted in **Figure 4.9**, basically keeping constants for four phases. More importantly, it unveils an intrinsic difference in the number of valence electrons of the four phases that $\beta'/\beta$-$In_2Se_3$ possesses ~0.5 more $n_0$ than $\alpha$-$In_2Se_3$ when comparing the same stacking structure (2H or 3R). The more valence electrons in $\beta'/\beta$-$In_2Se_3$ are consistent with their higher conductivity [97,154,157], probably from the more octahedral coordination in $\beta'/\beta$-$In_2Se_3$ which has been demonstrated to be relatively unstable [158]. Numerically, the first peak at ~15 eV corresponds to $n_0 \approx 23$ primarily from the outer electrons except electrons in 4d orbits of Indium atoms and the second peak corresponds to ~ 44 electrons equaling the total outer electrons, calculated by **Equation (1.3)** and **(4.2)**.

The results eventually prove that the measured $E_p$ difference in **Figure 4.5** is not only caused by the volume effect, as shown in **Figure 4.8**, but also due to their different valence electrons as shown in **Figure 4.9**.

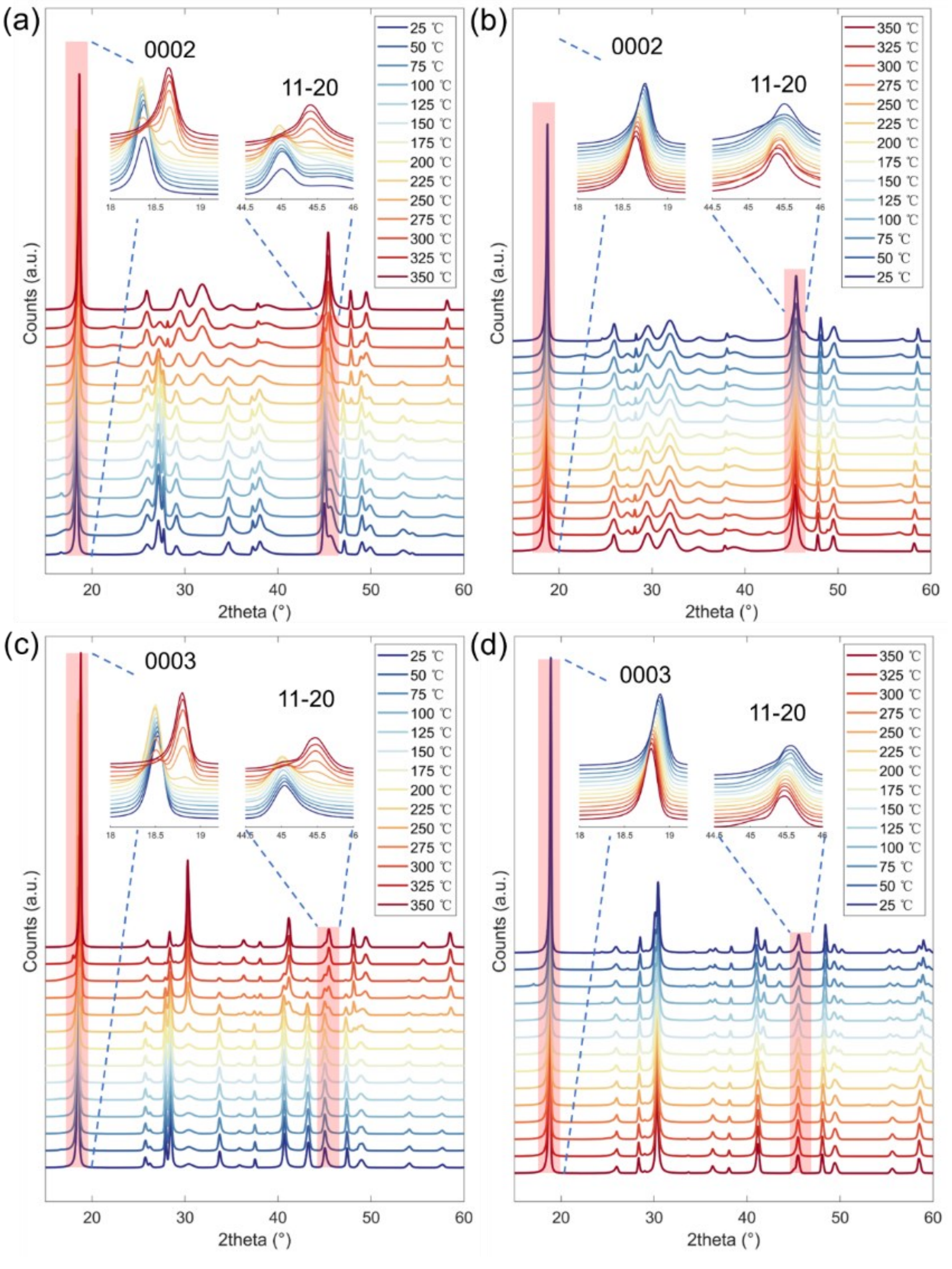

**Figure 4.7.** XRD spectra of four $In_2Se_3$ phases (a) $\alpha 2H$ (b) $\beta' 2H$ (c) $\alpha 3R$ (d) $\beta' 3R$ under different temperature showing obvious diffraction peaks shift due to the thermal expansion, and their characteristic symmetry. Spectra are shifted with an incremental constant in sequence for clear visualization. Insets show the larger versions for (0002)/(0003) and (11-20) peaks.

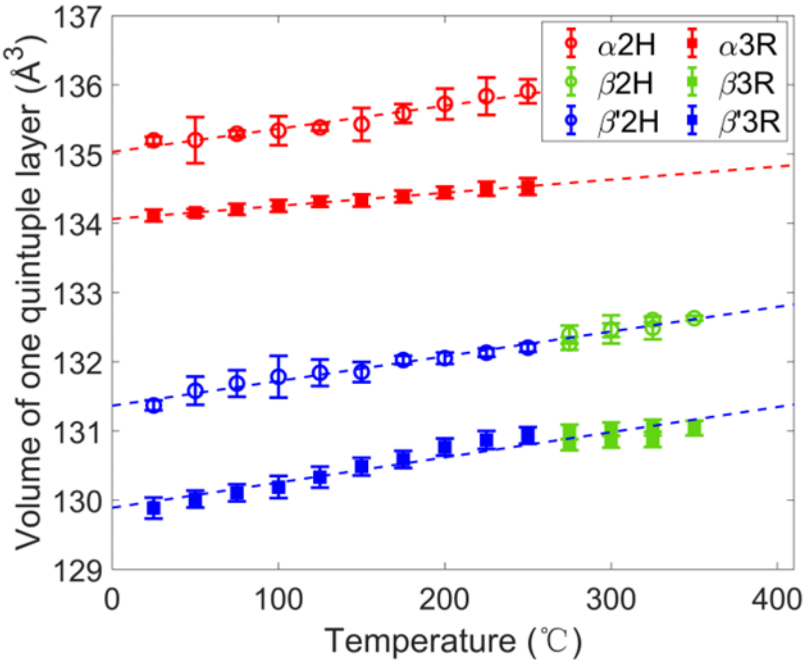

**Figure 4.8.** Unit-cell volumes of single quintuple layer, as functions of temperature for the four $In_2Se_3$. The linear thermal expansions are indicated by the fitted dashed lines. Error bars are the 95% confidence interval half widths.

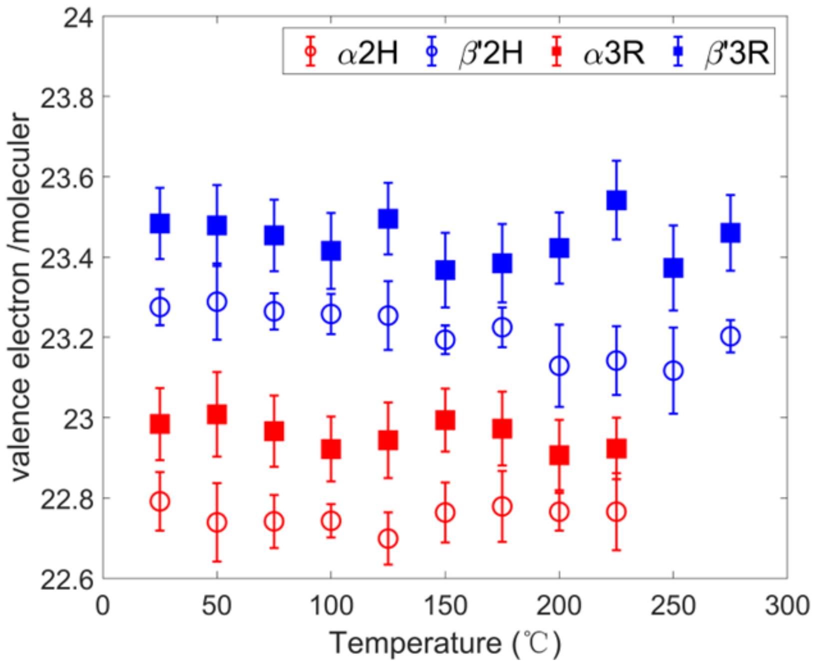

**Figure 4.9.** Derived numbers of valence electrons as functions of temperature for the four $In_2Se_3$ phases at [0001] orientation, keeping constants at different temperature. Error is from the uncertainty of volumes and plasmon positions.

**Table 5.** Linear volume thermal expansions coefficients of four $\mathrm{In_2Se_3}$, their volumes of one quintuple layer in a unit cell at 25 °C, energy position of maximums of calculated energy-loss functions, and references. [a]Ref. [143], [b]Ref. [76], [c]Ref. [144], \\ for no report. Errors are the 95% confidence interval half widths.

| | $\alpha 2H$ | $\alpha 3R$ | $\beta' 2H$ | $\beta' 3R$ |
|---|---|---|---|---|
| VTECs ($10^{-5}K^{-1}$) | 2.47 (90) | 1.41 (15)/3.1[a] | 2.72 (40) | 2.80 (89) |
| Volume ($\mathring{A}^3$) @ 25 °C | 135.2 (1) | 134.1 (1) | 131.4 (1) | 129.9 (2) |
| Reference | 134.7 (1)[b] | 134.5 (3)[b] | \\ | 130.1(8)[c] |
| Plasmon Energy (eV) | | | | |
| 1st peak | 15.44 (3) | 15.53 (3) | 15.97 (4) | 15.96 (4) |
| 2nd peak | 20.29 (4) | 20.60 (6) | 21.33 (7) | 21.55 (7) |

## 4.5 First-principles calculations

Up to this point, the origins of the measured plasmon energy difference are uncovered experimentally, from the volume change and valence electrons involved in the plasma resonance. Conceivably, the different $n_0$ often implies a variation in the bonding environment that always occur in phase transitions. From a crystal structure perspective, the $\alpha$ phases are composed of one Indium octahedral coordination and one Indium tetrahedral while $\beta'$ phases are two Indium octahedral coordination. Moreover, the octahedral coordination with longer bond length (~1.1 times of tetrahedral coordination) is reported to be more volatile [158,159], hence leading to a greater $n_0$. To further verify our experiment results and investigate the connection between the structure and the valence electron, first-principles calculations are performed.

### 4.5.1 Calculation of energy-loss function

The calculation of energy-loss function Im(-1/ϵ) are firstly conducted, as the EEL spectra are predominantly determined by it, expressed in a dielectric formulation as:

$$\frac{d^2\sigma}{d\Omega dE}=\frac{Im[-1/\epsilon(q,E)\,]}{\pi^2 a_0 m_0 v^2 n_a}\frac{1}{\theta^2+\theta_E^2} \tag{4.3}$$

where $\boldsymbol{a_0}$ is the first Bohr radius, $\boldsymbol{v}$ is the speed of the incident electron, and $\boldsymbol{n_a}$ is the number of atoms per unit volume. The calculating real parts and imaginary parts of the dielectric function (blue solid and blue dash) at q=0, as well as the energy-loss functions (red solid) of four $In_2Se_3$, are presented in **Figure 4.10a**.

The calculated energy-loss functions exhibit a similar shape and peak positions to those of the measured EEL spectra for four phases, thus reinforcing our results again. Specifically, the first plasmon peaks occur at the point (red dot lines in **Fig.** 4(a)) where $\epsilon_1$ crosses zero with a positive gradient and $\epsilon_2$ is less than 1 and negative gradient, and the second plasmon peaks occur at the intersection of $\epsilon_1$ and $\epsilon_2$ (red dash-dot lines in **Figure 4.10a)** which agree with anticipated minimums [42,98,160] and mathematical solution discussed in **Appendix A.6**. The exact positions are documented in **Table 5**, showing the higher energy position in $\beta$ phases same as our experiment results. Despite a ~ 0.5 eV difference to the experimental values, it is acceptable, considering the plasmon in EELS could be relaxed or damped by other factors.

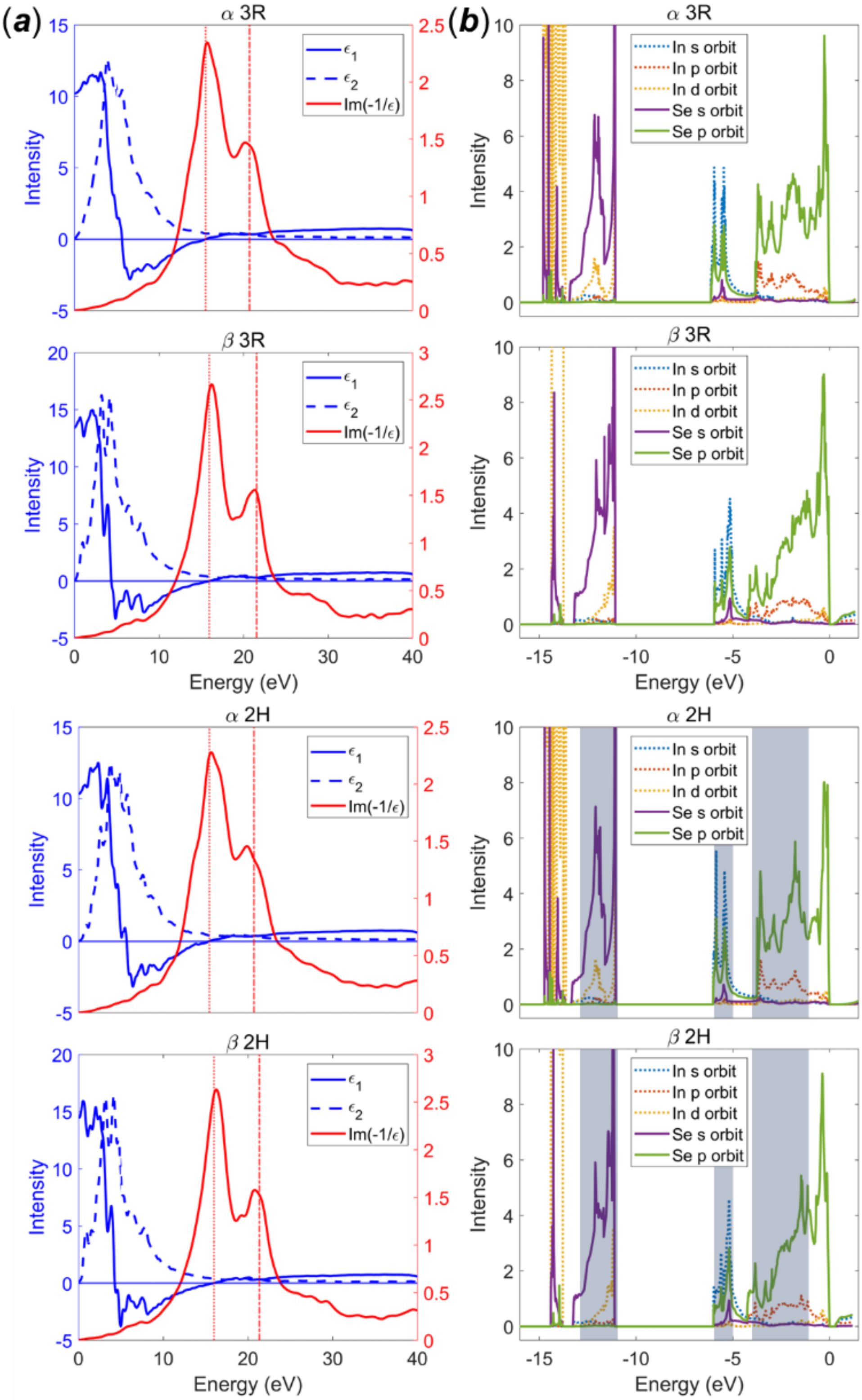

**Figure 4.10.** (a) Calculated real parts (blue solid) and imaginary parts (blue dash) of dielectric function, and energy-loss function (red solid) for four $In_2Se_3$, with dot lines and dash dot lines to indicate the plasmon position. (b) Calculated projected density of states for four $In_2Se_3$, with shadow regions to indicate the forward shift of the band structure in $\beta$ phase. From top to bottom, phases are α3R, β3R, α2H, β2H.

### 4.5.2 Calculation of projected density of states

Furthermore, the other calculation about the electronic structures of $In_2Se_3$ provide possible speculation to the underlying reason for variance in $n_0$. **Figure 4.10b** displays the projected density of electronic states for the four phases, covering electrons in 5s/5p/4d orbits of Indium, and 4s/4p orbits of Selenium. In the band structures, most of electrons in Indium 5s/5p and Selenium 4s/4p orbits are in the energy range of (-13.5, 0) eV and categorized as covalent electrons due to their substantial orbital overlap. Meanwhile, Indium 4d and a fraction of Se 4p electrons are segregated from those electrons in the (-15, -13.5) eV range due to their superior stability as lone pairs. Consequently, the electron bonding nature causes the dual-plasmon shape of $In_2Se_3$, as supported by the similar values in the valence electrons of experiment and calculation.

Distinctions between $\alpha$ and $\beta'$ phases manifest in the shaded regions with energy ranges of (-4, -1), (-6, -5), and (-13, -11) eV, with the $\beta'$ exhibiting elevated energy levels of Indium 5p/Se 4p orbits, Se 4s/Se 4p orbits, and Indium 4d/Se 4s orbits, respectively. The average energy levels of the five orbits in the energy range of (-13.5, 0) eV are consistently higher in the $\beta'$ phases than $\alpha$ phases, as tabulated in **Table** 6. The similar results emerge in the energy range of (-15, 0) eV involved in the total outer shell electrons. These findings indicate that outer electrons in $\beta'$ phases have weaker binding, making them more likely to participate in plasma oscillations under an external electrical field, which is consistent to their higher conductivity compared with $\alpha$ phases.

However, further research is needed to understand how the density of states of outer electrons influences plasma oscillations.

**Table 6.** The average energy levels of the electrons with energy between -13.5 to 0 eV (-13.5 eV located at a gap) in the Indium 5s/ 5p/ 4d and Se 4s and 4p orbits.

| Energy (eV) | In 5s | In 5p | In 4d | Se 4s | Se 4p |
|---|---|---|---|---|---|
| $\alpha$3R | -5.78 | -3.15 | -9.13 | -11.27 | -2.23 |
| $\alpha$2H | -5.74 | -3.10 | -9.02 | -11.25 | -2.15 |
| $\beta'$2H | -5.52 | -2.94 | -8.27 | -11.16 | -1.96 |
| $\beta'$3R | -5.48 | -2.89 | -8.22 | -11.12 | -1.92 |

## 4.6 Conclusion

In summary, we have demonstrated the characteristic dual-plasmon valence EEL spectra of $\alpha/\beta'$ $In_2Se_3$, which shows good agreement with the calculated energy-loss functions. One peak is primarily from the bonding valence electron, and the other peak is from the total outer-shell electron.

The ability of phase identification has been fully demonstrated at cross-sectional and plane samples. This method is effective and orientation-independent for locating the $\alpha/\beta'$ phases of $In_2Se_3$, based on the subtle differences in plasmon energy valence EELS. In the first case, the EELS mapping was conducted on nanoscale intergrowing cross-sectional samples, allowing for a high-resolution analysis. The obtained resolution of approximately 1.1 nm enables locating single quintuple layer of $In_2Se_3$. The second case involved a plane phase-mixed sample with a $\beta'$ region of ~ 200 nm in diameter which shows the ability to locate phases at sub-micrometer scale.

In addition, we utilized *in situ* XRD and EELS techniques to verify the great repeatability of phase identification based on plasmon energy and shed light on the underlying physical processes which convincingly reveal the causes of plasmon shift, the structural volumes and intrinsic equivalent valence electrons participating in plasma oscillations. This finding is further confirmed through calculated energy-loss functions and projected density of states. We also discovered that the outer valence electrons in $\beta'$ phases are more active than those in $\alpha$ phases, due to longer bonding length between octahedrally coordinated Indium atoms and neighboring Se atoms, which can contribute to the slightly greater valence electrons in $\beta'$ phases.

Our findings may have broader implications, as they can be extended to other chalcogenides and transition metal materials, highlighting the potential of plasmonic phenomena and phase identification for advancing the field of materials science.

# Chapter 5 Conclusion

## 5.1 Summary

In summary, we have presented the application of quantitative diffraction and EEL spectra on dose-sensitive materials. For probing the pristine structure of polymers, the beam effects on PE, PCL, and P3HT spherulite thin films were researched based on the time-series SAED and EELS, revealing some intriguing details on degradation. In PE and PCL spherulites, radiolysis dominates initially, resulting in amorphization and lattice expansion, and then surface sputtering dominates. EELS analysis provides a mechanism for amorphization and lattice expansion which is caused by the formation of unsaturated polyenyl group. Conversely, P3HT spherulites exhibit a more complex two-stage damage process at cryogenic temperatures, with preferential damage to sidechain ordering before π-stacking ordering which is attributed to cryo-protection and the ultrathin film thickness compared to the inelastic mean free path. Additionally, cryo-protection is found to effectively suppress most beam effects.

With an understanding of beam degradation of polymers, advanced 4D-STEM system, and algorithm for solving 4D datasets, we explicitly demonstrated microstructures and phase distributions in PE and PCL in great details. PE exhibits a crystal rotation around the crystallographic b axis and a growth direction along [1-10] in the radial direction, with continuous orientation over the polar angle. As a result, PE spherulites uniformly extend outward from their core with a twist in the crystal structure in the radial direction. Moreover, PCL spherulites without local twists also exhibit an outward growth direction along [1-10], while azimuthally a radial pattern is separated by an amorphous gap resulting from inhomogeneous crystallinity verified by phase mapping.

For another dose-sensitive materials, 2D $In_2Se_3$, we have demonstrated phase identification with resolution of ~ 1.1 nm on its polymorphs, utilizing their distinct plasmon energies in EELS. The characteristic plasmon energies of $In_2Se_3$ polymorphs have been explicitly validated using first-principles calculations and *in situ* EELS, which have also been applied to study phase transitions. Correlating with *in situ* X-ray diffraction, we further reveal a subtle difference in the valence electron density of $In_2Se_3$ polymorphs.

## 5.2 Perspective

The 4D-STEM technology possesses several advantageous characteristics, like high resolution, ultralow dose, and large FOV, making it a valuable tool for exploring dose-sensitive materials. Diffraction-based 4D datasets also provide a wealth of information, including local orientation, stress, and phase. However, interpreting this rich dataset requires in-depth analysis and the development of suitable algorithms to extract and comprehend relevant information.

Moreover, the EELS-based phase identification technique offers high resolution and a relatively low dose requirement. This technique is also independent of sample orientation, allowing for quick and efficient differentiation of polymorphic materials. Therefore, it is a favorable choice for future investigation on the mechanism of phase switching and nucleation of the secondary phase.

In summary, both 4D-STEM and EELS-based techniques offer unique advantages for exploring and characterizing materials at the nanoscale, presenting valuable tools in studying dose-sensitive materials.

# Appendix

## A.1 Heating effects of electron beam

Heating is a main electron effects on samples, and the rising temperature can be estimated by the thermal equilibrium between the input of energy from electrons beam and the output as the radiation and conduction of heat to the periphery of the specimen. Therefore, the evolution of the temperature of illuminated region can be written as

$$T(t) = T_o + \frac{LP_{dep}}{kA_s}[1 - e^{-t/t_{sys}}] \tag{S1}$$

where

$$t_{sys} = \rho c_p V/hA_s \tag{S2}$$

$P_{dep}$ is the deposited power (J/s) to the specimen, $A_s$ is the area through which heat is conducted, $T_o$ is the initial temperature of the sample, $k$ is the heat conductivity, $L$ is the mean distance from illuminated area to the copper grid, $V$ is the volume of the illuminated sample, $c_p$ is the specific heat capacity of the sample. By heating simulations, for polymers the thermal balance can be reached within milliseconds after exposure, and beam heating is limited (tens of K) at about 1 e/Å$^2$ electron dose [31,140]. Additionally, the coefficients of linear thermal expansion of three polymers are all less than $2\times10^{-4}$/K (usually PCL>PE> P3HT). To reach the result as measured in our experiments, at least 200K temperature rise is needed. Thus, for the three polymers, the heating takes a limited effect on the lattice expansion.

### A.2 Degradation of polymers

Under the electron beam, the degradation of crystalline polymers involves two main aspects: radiolysis and knock-on. Radiolysis leads to amorphization, transforming the crystalline component into the amorphous state. Knock-on, on the other hand, causes total mass loss which decreases the total diffraction signals combining the intensity of amorphous component and crystalline intensity. The transformation of the crystalline component is approximately an exponential function of the electron dose, but the evolution of diffraction signal *I* is complex, due to decreasing rate of mass loss with losing mass.

In this section, we simply estimated the diffraction signal with mass loss based on the scatter theory. It is assumed that in some thickness range (within one inelastic mean free path), the diffraction intensity is determined by total diffraction probability $\sigma_D$ which is proportional to *T*, the thickness of samples. Note the probabilities for crystalline and amorphous components should be different, so it is improper to merge them together, and the diffraction intensity for different phases should be discussed separately. We get:

$$I = C_1\sigma_D \qquad (S4)$$

$$\sigma_D = C_2 T \qquad (S5)$$

where $C_n$ denote different positive constant. While the thickness of sample would be thinned because of knock-on which is related to the electron dose *D*, and can be expressed as

$$T = T_o - \int_o^D \sigma_T \, C_3 \, dD \qquad (S6)$$

where $\sigma_T$ is the probability of thinning. In reality, the thinning probability is related to many factors, but here we use a simple model to describe the thinning process: the atom in the surface has a maximum probability $\sigma_1$ of being knocked out, while the interior scattered atoms due to the probable recombination with neighboring atoms contributes less probability to sample thinning which can be assumed as:

$$\sigma_{int} = (1 - LC_4)\sigma_1 \qquad (S7)$$

where $L$ is the distance between atom to surface, $C_4$ is the rate of recombination which should be positively related to temperature because of shorter mean free path for atom recombination/collision in higher temperature. Thus, there are two cases must be discussed $for\ T \leq 2/C_4$ and for $\mathrm{T} > 2/\mathrm{C}_4$. In the first case, the $\sigma_T$ can be expressed as the integration to thickness:

$$\sigma_T = 2C_5 \int_o^{T/2} (1 - LC_4)\sigma_1 \, dL = (T - C_4T^2/4)\sigma_1 C_5 \qquad (S8)$$

Then, substituting **Equation S8** into **S6**, get

$$T = T_o - \sigma_1 C_5 C_3 \int_o^D (T - C_4T^2/4) \, dD \qquad (S9)$$

and **Equation S8** can be written as a second-order linear homogeneous differential equation with constant coefficients:

$$T'' + \sigma_1 C_3 C_5 (T' - C_4 T/2) = 0 \qquad (S10)$$

Its general solution is:

$$T = \mathrm{A}_1 \mathrm{e}^{r_1 \mathrm{D}} + \mathrm{A}_2 \mathrm{e}^{r_2 \mathrm{D}} \qquad (S11)$$

where $r_1$ and $r_2$ are $0.5\sigma_1 C_3 C_5\left(-1 \pm \sqrt{1 - 2C_4/\sigma_1 C_3 C_5}\right)$ and $A_1$, $A_2$ are any constant. Only considering the realistic condition, thickness should be decreasing with dose and positive, and then $\mathrm{r}_1$ and $\mathrm{r}_2$ are distinct and negative and $\mathrm{A}_1$, $\mathrm{A}_2$ are positive. In most cases, the **Equation S11** can been fitted by a general exponent function.

In the second case, $\mathrm{T} > 2/\mathrm{C}_4$, $\sigma_T=\sigma_1 \mathrm{C}_5/\mathrm{C}_4$ is a constant, and the thickness is linearly decreasing. Due to the **Equation S4** and **S5**, the intensity of total diffraction signals should have a same linear decrease with dose accumulation.

As we have shown, the total diffraction signals $I_{total}$ exhibit two different evolutionary paths with the accumulation of electron dose. At cryogenic conditions, such as the results of P3HT at 98K, its total diffraction signals (both amorphous and crystalline signal are exponentially related to accumulated dose) exhibit an exponential decrease. In contrast, for the RT results of P3HT and results of PE and PCL, they are either high in recombination rate or thick, and thus the total diffraction signals (amorphous signal is close to the total signals when accumulated dose is over 20 e/Å$^2$) show a linear decrease. They are both consistent with the observed degradation under high-energy electron beam irradiation.

### A.3 Electron damage in 4D-STEM measurements

The HAADF image of PCL thin film after raster scanning shows an evident array of scorch marks in **Figure A.1** (data acquired at Jeol ARM 300CF), and these spots have an inverse contrast to their neighboring area, measured about 100 nm. The bright represents high-crystalline and the dark means low-crystalline/amorphous or potential structure change. So, the contrast of spots also proves that the damage of electron beam inflicts radiolysis and knock-on effect on the sample, that reduce the crystallinity and attenuate the sample respectively. Although the size cannot represent that the diffraction signal is from a corresponding area with this size, it gives a reference about the size of the damaged area by a STEM probe.

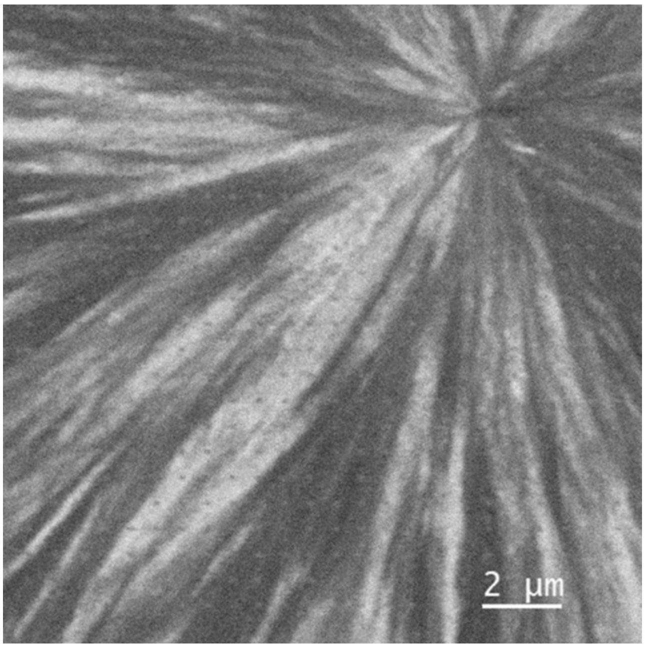

**Figure A.1.** The HAADF image of PCL thin film after raster scanning presenting an evident array of scorch spots with an inverse contrast to their circumjacent region.

### A.4 Orientation maps based on other diffraction points

If following the direction of (200) diffraction or the orientation of (110) diffraction, the orientation maps are different distinctly showing vortex flows out from the nucleus as presented in **Figure A.2a, b**. The orientation maps following normal of (200) and (1-10) diffraction (vertical to the direction of (110) and (200) diffraction) also show a vortex around the nucleus as presented in **Figure A.2c, d**, which are counterintuitive.

Although it is possible for a spherulite thin films to follow a vortex growth, the HAADF images and POM images of this model will show different patterns but concentric circles.

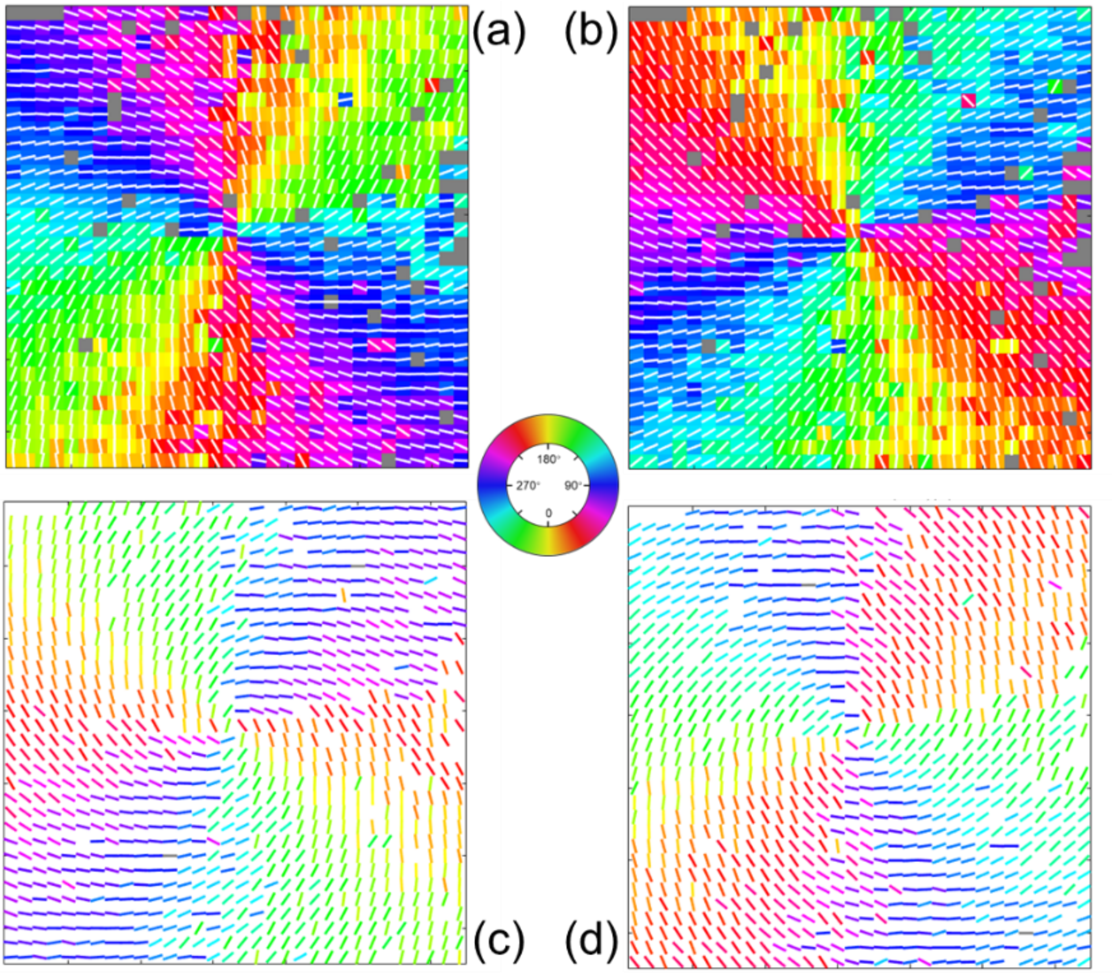

**Figure A.2.** Orientation maps by following the normal of (200) and (110) diffraction (a, b), and equivalent growing orientation maps for (a) and (b) by rotating the local direction 90°. The blank positions represent that the diffraction is absent or missed due to technical reasons.

## A.5 Contrast of cross-sectional $\alpha/\beta'$ intergrowing $In_2Se_3$

In the images acquired from different collection angles, the intensities of the $\alpha$ and $\beta'$ phases have different changing paths. In the HAADF images, the $\beta'$ phase appears to have a stronger contrast, while in the Low-Angle ADF (LAADF) images, the α phase exhibits stronger contrast. This distinction is clearly illustrated in **Figure A.3**, where the two phases are easily distinguishable, and no surface contamination is observed. **Figure A.2d** displays the intensity ratio of the two phases as a function of the collection angle. The results demonstrate a significant mass for the $\beta'$ phases, indicating a higher concentration compared to the $\alpha$ phase. The smaller cell lattice of the $\beta'$ phase leads to a higher number of atoms in a unit volume, thus a greater mass thickness. Additionally, these results help to exclude the possibility of surface contamination, as the observed contrast variation is attributed to the inherent differences in the two phases rather than external factors which are often seen in LAADF images [148].

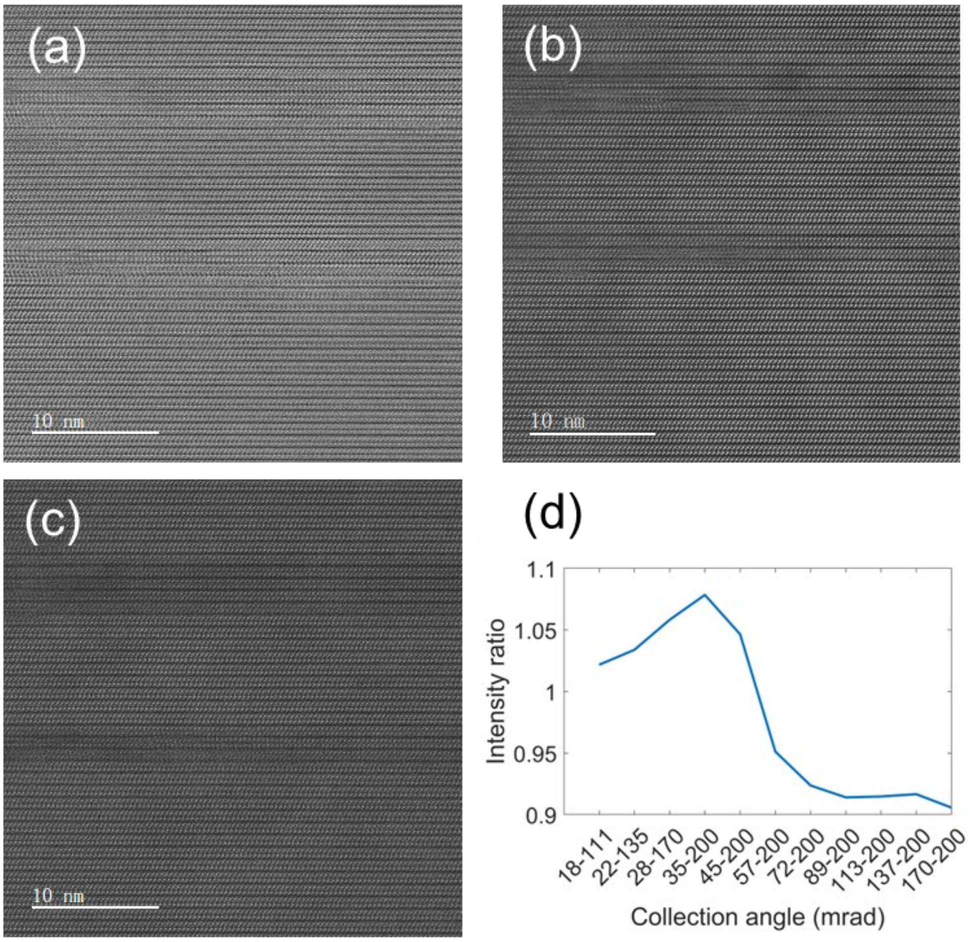

**Figure. A.3.** (a-c) STEM images acquired from collection angle of 18-111, 28-170, 113-200 mrad. (d) The intensity ratio of $\alpha$ and $\beta'$ under different collection angles.

## A.6 Estimation of plasmon resolution

If considering the intrinsic plasmon energy map as a step function, the measuring result is a convolution of the step function and the object-probe, which is the exiting beam from the incident beam delocalized by inelastic scattering. For simplicity the function of object-probe is assumed as a Gaussian function, thus the measurement equivalent to an error function. By fitting the error function (dash line in **Figure 4.3d**, the standard deviation of error function is about 0.54 (14) nm, thus deducing a resolution of ~1.10 (43) nm under the Rayleigh criterion. This resolution is higher than the theoretical estimation of ~ 2.34 nm at 200 kV based on **Equation S12** introduced by Egerton [98]:

$$d_{50} = \sqrt{(\lambda/(2\theta_E^{3/4}))^2 + (0.6\lambda/\beta)^2} \qquad (S12)$$

where the electron wavelength λ = 1.98 pm, the characteristic scattering angle $\theta_E$ ~ 0.04 mrad at 15eV and the collection semi-angle $\beta$ = 8.9 mrad. For comparison, at 300 kV, the resolution is ~1.04 (51), and the theoretical estimation is ~ 2.39 nm (**Figure. A.4**). The higher resolution in experiments probably arises from the high signal-noise-ratio and energy-sensitive detectors (enough to identify the signal in width containing less than 50% of the scattered electrons) and the underestimate of $\theta_E$.

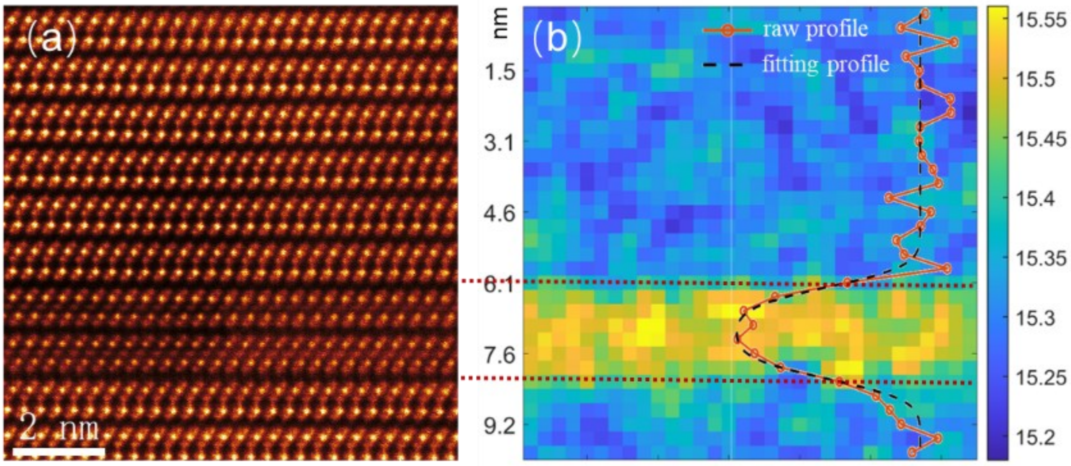

**Figure. A.4.** (a) HAADF image of two quintuple-layer $\beta'$ phase inserted in the $\alpha$ phase matrix. (b) EELS maximum plasmon energy map of the region of (a) and its raw (red) and fitting (black dash) energy profiles, acquired at 300 kV of Spectra 300, where the $\beta'$ region reveals higher plasmon energy. For better visualization, a light Gaussian smoothing with a standard deviation of 0.6 is applied only in the EELS mapping.

### A.7 More *in situ* EELS

As stated in Chapter 4.4.1, the first plasmon maximum energies of four phases exhibit a linear decrease with the increased temperature. The results shown in **Figure 4.5** only mainly exhibit the heating process of $\alpha$ phases and cooling process of $\beta'$ phases. Therefore, to exclude the effects of heating/cooling hysteresis and probable stress relaxation under phase changes, other temperature-changing processes are implemented. **Figure A.5** display the plasmon energies are not changed by the temperature-changing direction within a tolerable error (less than 0.05 eV). Moreover, *in situ* EELS has been repeated with good reproducibility. One of the repeating results is shown in **Figure A.6** which is exactly similar to that shown in **Figure 4.5**. Thus, our robust EELS results demonstrate the intrinsic change but from other factors.

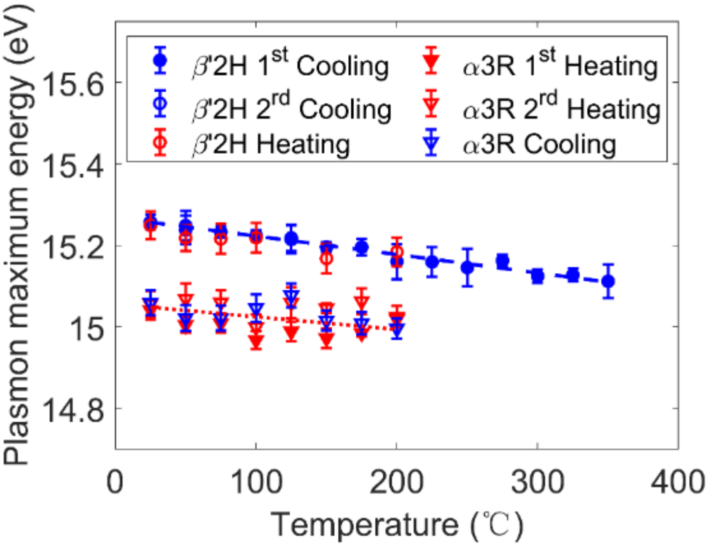

**Figure A.5.** Plasmon maximum energy as a function of different temperature for $\alpha$3R and $\beta'$2H without phase change. The plasmon energy under different temperatures is repeatable within the allowed error range, verifying the robustness of measurement and excluding the effects from temperature-changing direction and probable stress relaxation under phase changes.

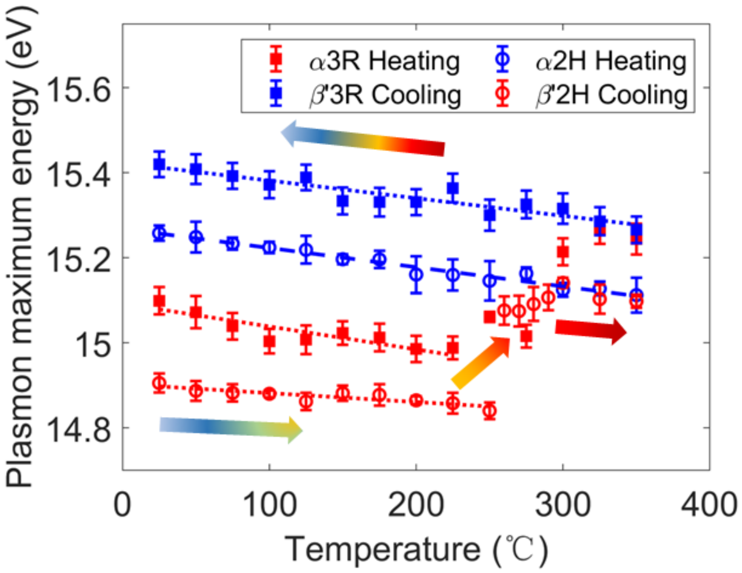

**Figure A.6.** Repeating experiments for the results in **Figure 4.5**, showing similar results within acceptable error. Plasmon maximum energy of four $In_2Se_3$ along <0001> as a linear function of different temperatures.

### A.8 Mathematical explanation of plasmon peaks

The loss function ***L(ϵ)*** is related to the imaginary part $\epsilon_1$ and real part $\epsilon_2$ of dielectric function following:

$$\boldsymbol{L(\epsilon) = \frac{\epsilon_2}{\epsilon_1^2 + \epsilon_2^2}} \qquad (S13)$$

Thus, its first derivative can be written as:

$$\boldsymbol{L'(\epsilon) = \frac{-2\epsilon_1\epsilon_1'\epsilon_2 + \epsilon_2'(\epsilon_1^2 - \epsilon_2^2)}{\left(\epsilon_1^2 + \epsilon_2^2\right)^2}} \qquad (S14)$$

Now, depending on the calculated dielectric function in **Figure 4.10** and **4.11**, there are two cases to generate a maximum of loss function:

1) When $\epsilon_1 \sim 0, \epsilon_1' > 0, \epsilon_2 > 0, \epsilon_2' < 0$,

in **Equation S14**, the first term from positive to negative, the second term positive, thus a maximum at $\omega \approx \omega_{\epsilon_1 = 0}$.

2) When $\epsilon_1 \sim \epsilon_2 > 0, \epsilon_1' > 0, \epsilon_2' < 0$,

in **Equation S14**, the first term negative, the second term from positive to negative, thus a maximum at $\omega \approx \omega_{\epsilon_1 = \epsilon_2}$.

# Reference

1. Chen, Q., Dwyer, C., Sheng, G., Zhu, C., Li, X., Zheng, C., Zhu, Y., Imaging Beam-Sensitive Materials by Electron Microscopy. *Adv. Mater.,* **2020,** *32*, 1907619.

2. Hu, W., The physics of polymer chain-folding. *Phys. Rep,* **2018,** *747,* 1-50.

3. Wunderlich, B., *Macromolecular Physics, in: Crystal Structure, Morphology, Defects*, New York, **1973**.

4. Eppe, R., Fischer, E. W., Stuart, H. A., Morphologische strukturen in polyäthylenen, polyamiden und anderen kristallisierenden hochpolymeren. *J.Polym. Sci.*, **1959**, XXXIV, 721-740.

5. Uyeda, N., Direct imaging of organic molecules in crystals by high resolution electron microscopy at atomic level. *Dye. Pigment.,* **1985**, 6, 115-134.

6. Discher, B. M., Won, Y. Y., Ege, D. S., Lee, J. C., Bates, F. S., Discher, D. E., Hammer, D. A., Polymersomes: tough vesicles made from diblock copolymers. *Science*, **1999**, *284*, 1143-1146.

7. Pochan, D. J., Chen, Z., Cui, H., Hales, K., Qi, K., Wooley, K. L., Toroidal triblock copolymer assemblies. *Science*, **2004**, 306, 94-97.

8. Yamauchi, K., Takahashi, K., Hasegawa, H., Iatrou, H., Hadjichristidis, N., Kaneko, T., Furukawa, H., Microdomain morphology in an ABC 3-miktoarm star terpolymer: a study by energy-filtering TEM and 3D electron tomography. *Macromolecules,* **2003**, 36, 6962–6966.

9. Sun, J., Jiang, X., Lund, R., Downing, K. H., Balsara, N. P., Zuckermann, R. N., Self-assembly of crystalline nanotubes from monodisperse amphiphilic diblock copolypeptoid tiles. *Proc. Natl. Acad. Sci.,* **2016**, 113, 3954–3959.

10. Yang, Y.; Chen, H.; Li, H., Polymer single crystal dielectrics for organic field-effect transistors. *Polymer*, **2018,** *137*, 255-260.

11. Li, Y., Wang, Z., & He, T., Morphological control of polymer spherulites via manipulating radial lamellar organization upon evaporative crystallization: A mini review. *Crystals*, **2017**, *7*, 115.

12. Li, Y., Huang, H., Wang, Z., & He, T., Tuning radial lamellar packing and orientation into diverse ring-banded spherulites: effects of structural feature and crystallization condition. *Macromolecules*, **2015**, *47*, 1783-1792.

13. Nurkhamidah, S.; Woo, E.M. Unconventional Non-birefringent or Birefringent Concentric Ring-Banded Spherulites in Poly(L-lactic acid) Thin Films. *Macromol. Chem. Phys.*, **2013**, *214*, 673–680

14. Lugito, G.; Woo, E.M.; Hsieh, Y.T. Transitional Ring Bands Constructed by Discrete Positive- and Negative-Birefringence Lamellae Packed in Poly(1,6-hexamethylene adipate) Spherulites. *Macromolecules*, **2015**, *48*, 7953–7967.

15. Ye, H.M.; Xu, J.; Guo, B.H.; Iwata, T. Left- or Right-Handed Lamellar Twists in Poly[(R)-3-hydroxyvalerate] Banded Spherulite: Dependence on Growth Axis. *Macromolecules*, **2009**, *42*, 694–701.

16. Panova, O.; Ophus, C.; Takacs, C. J.; Bustillo, K. C.; Balhorn, L.; Salleo, A.; Balsara, N.; Minor, A. M., Diffraction imaging of nanocrystalline structures in organic semiconductor molecular thin films. *Nat. mater.*, **2019,** *18*, 860-865.

17. Xu, H.; Lebrette, H.; Clabbers, M. T.; Zhao, J.; Griese, J. J.; Zou, X.; Högbom, M., Solving a new R2lox protein structure by microcrystal electron diffraction. *Sci. Adv.*, **2019,** *5*, eaax4621.

18. Clabbers, M. T. B.; van Genderen, E.; Wan, W.; Wiegers, E. L.; Gruene, T.; Abrahams, J. P., Protein structure determination by electron diffraction using a single three-dimensional nanocrystal. *Acta Crystallogr. D*, **2017,** *73*, 738-748.

19. Duyvesteyn, H. M. E.; Kotecha, A.; Ginn, H. M.; Hecksel, C. W.; Beale, E. V.; de Haas, F.; Evans, G.; Zhang, P.; Chiu, W.; Stuart, D. I., Machining protein microcrystals for structure determination by electron diffraction. *Proc. Natl. Acad. Sci.*, **2018,** *115*, 9569-9573.

20. Cui, P.; Svensson Grape, E.; Spackman, P. R.; Wu, Y.; Clowes, R.; Day, G. M.; Inge, A. K.; Little, M. A.; Cooper, A. I., An expandable hydrogen-bonded organic framework characterized by three-dimensional electron diffraction. *J. Am. Chem. Soc.*, **2020,** *142*, 12743-12750.

21. Navas, J.; Sánchez-Coronilla, A.; Gallardo, J. J.; Piñero, J. C.; De los Santos, D.; Martín, E. I.; Hernández, N. C.; Alcántara, R.; Fernández-Lorenzo, C.; Martín-Calleja, J., The impact of Pd on the light harvesting in hybrid organic-inorganic perovskite for solar cells. *Nano Energy*, **2017,** *34*, 141-154.

22. Yamaguchi, A.; Nemoto, T.; Kurata, H., Study of C K-Edge High Energy Resolution Energy-Loss Near-Edge Structures of Copper Phthalocyanine and Its Chlorinated Molecular Crystals by First-Principles Band Structure Calculations. *J. Phys. Chem. A.*, **2020,** *124*, 1735-1743.

23. Stoeckel, M. A.; Olivier, Y.; Gobbi, M.; Dudenko, D.; Lemaur, V.; Zbiri, M.; Guilbert, A. A. Y.; D'Avino, G.; Liscio, F.; Migliori, A.; Ortolani, L.; Demitri, N.; Jin, X.; Jeong, Y. G.; Liscio, A.; Nardi, M. V.; Pasquali, L.; Razzari, L.; Beljonne, D.; Samori, P.; Orgiu, E., Analysis of External and Internal Disorder to Understand Band-Like Transport in n-Type Organic Semiconductors. *Adv. Mater.*, **2021,** *33*, 2007870.

24. Pedrosa, M.; Drazic, G.; Tavares, P. B.; Figueiredo, J. L.; Silva, A. M. T., Metal-free graphene-based catalytic membrane for degradation of organic contaminants by persulfate activation. *Chem. Eng. J.*, **2019,** *369*, 223-232.

25. Duan, X.; Ao, Z.; Zhang, H.; Saunders, M.; Sun, H.; Shao, Z.; Wang, S., Nanodiamonds in sp 2 /sp 3 configuration for radical to nonradical oxidation: Core-shell layer dependence. *Appl. Catal. B: Environ.*, **2018,** *222*, 176-181.

26. Jiang, N., Electron beam damage in oxides: a review. *Rep. Prog. Phys.*, **2015,** 79, 016501.

27. Egerton, R. F., Radiation damage to organic and inorganic specimens in the TEM. *Micron*, **2019,** *119*, 72-87.

28. Egerton, R. F.; Li, P.; Malac, M., Radiation damage in the TEM and SEM. *Micron*, **2004,** *35*, 399-409.

29. Carter, C. B.; Williams, D. B., *Transmission electron microscopy: Diffraction, imaging, and spectrometry*. Springer: 2016.

30. Sawyer, L.; Grubb, D. T.; Meyers, G. F., *Polymer microscopy*. Springer Science & Business Media: 2008.

31. Karuppasamy, M.; Karimi Nejadasl, F.; Vulovic, M.; Koster, A. J.; Ravelli, R. B., Radiation damage in single-particle cryo-electron microscopy: effects of dose and dose rate. *J. Synchrotron Radiat.*, **2011,** *18*, 398-412.

32. Ueno, T., Nakashima, E., & Takeda, K. (2010). Quantitative analysis of random scission and chain-end scission in the thermal degradation of polyethylene. *Polym. Degrad. Stab.*, **2010,** *95*, 1862-1869.

33. Uchida, K.; Shimizu, N., The effect of temperature and voltage on polymer chain scission in high-field region. *IEEE Trans. Dielectr. Electr. Insul.*, **1991,** *26*, 271-277.

34. Kuei, B.; Bator, C.; Gomez, E. D., Imaging 0.36 nm Lattice Planes in Conjugated Polymers by Minimizing Beam Damage. *Macromolecules*, **2020,** *53,* 8296-8302.

35. Kuei, B.; Gomez, E. D., Pushing the limits of high-resolution polymer microscopy using antioxidants. *Nat. Commun.*, **2021,** *12*, 153.

36. D. Zhang, Y. Zhu, L. Liu, X. Ying, C. E. Hsiung, R. Sougrat, K. Li, Y. Han, Atomic-resolution transmission electron microscopy of electron beam–sensitive crystalline materials. *Science*, **2018,** 359, 675.

37. Y. Zhu, J. Ciston, B. Zheng, X. Miao, C. Czarnik, Y. Pan, R. Sougrat, Z. Lai, C. E. Hsiung, K. Yao, I. Pinnau, M. Pan, Y. Han, Unravelling surface and interfacial structures of a metal–organic framework by transmission electron microscopy. *Nat. Mater.*, **2017,** 16, 532.

38. Rothmann, M. U., Kim, J. S., Borchert, J., Lohmann, K. B., O'Leary, C. M., Sheader, A. A., Herz, L. M., Atomic-scale microstructure of metal halide perovskite. *Science*, **2020**, 370, eabb5940.

39. Leijten, Z.; Keizer, A. D. A.; de With, G.; Friedrich, H., Quantitative Analysis of Electron Beam Damage in Organic Thin Films. *J. Phys. Chem. C*, **2017**, *121*, 10552-10561.

40. Kobayashi, K.; Sakaoku, K., The Changes of Polymer Crystals due to Irradiation with Electrons Accelerated at Various Voltages (Special Issue on Electron Microscopy). *Bull. inst. chem. res., Kyoto univ.* **1965,** *42*, 473-493.

41. Hayward, S. B., Glaeser, R. M., Radiation damage of purple membrane at low temperature. *Ultramicroscopy*, **1979,** *4,* 201-210.

42. Ritsko, J. J., Electron energy loss spectroscopy of pristine and radiation damaged polyethylene. *J. Chem. Phys.*, **1979,** *70*, 5343-5349.

43. Guo, C.; Allen, F. I.; Lee, Y.; Le, T. P.; Song, C.; Ciston, J.; Minor, A. M.; Gomez, E. D., Probing Local Electronic Transitions in Organic Semiconductors through Energy-Loss Spectrum Imaging in the Transmission Electron Microscope. *Adv. Funct. Mater.*, **2015,** *25*, 6071-6076.

44. Leijten, Z. J., Wirix, M. J., Lazar, S., Verhoeven, W., Luiten, O. J., de With, G., Friedrich, H., Nanoscale chemical analysis of beam-sensitive polymeric materials by cryogenic electron microscopy. *J. Polym. Sci.*, **2021,** *59,* 1221-1231.

45. Varlot, K., J. M. Martin, C. Quet, EELS analysis of PMMA at high spatial resolution. *Micron*, **2001,** *32,* 371-378.

46. Tate, M. W., Purohit, P., Chamberlain, D., Nguyen, K. X., Hovden, R., Chang, C. S., Gruner, S. M., High dynamic range pixel array detector for scanning transmission electron microscopy. *Microsc. Microanal.*, **2016,** 22, 237-249.

47. Philipp, H., Tate, M., Shanks, K., Mele, L., Peemen, M., Dona, P., Muller, D. Wide dynamic range, 10 kHz framing detector for 4D-STEM. *Microsc. Microanal.*, **2021,** 27, 992-993.

48. McMullan, G., Faruqi, A.R., Clare, D. and Henderson, R, Comparison of optimal performance at 300 keV of three direct electron detectors for use in low dose electron microscopy. *Ultramicroscopy*, **2014,** 147, 156-163.

49. Jiang, Y., Chen, Z., Han, Y., Deb, P., Gao, H., Muller, D. A., Electron ptychography of 2D materials to deep sub-ångström resolution. *Nature*, **2018,** *559,* 343-349.

50. Zhang, H., Li, G., Zhang, J., Zhang, D., Chen, Z., Liu, X., Han, Y, Three-dimensional inhomogeneity of zeolite structure and composition revealed by electron ptychography. *Science*, **2023,** 380, 633-638.

51. Chen, F. R., Van Dyck, D., Kisielowski, C., In-line three-dimensional holography of nanocrystalline objects at atomic resolution. *Nat. Commun.*, **2016,** 7, 10603.

52. Drummy, L. F.; Yang, J.; Martin, D. C., Low-voltage electron microscopy of polymer and organic molecular thin films. *Ultramicroscopy*, **2004,** *99*, 247-56.

53. Kisielowski, C., Specht, P., Freitag, B., Kieft, E. R., Verhoeven, W., van Rens, J. F., Yancey, D. F., Discovering hidden material properties of MgCl2 at atomic resolution with structured temporal electron illumination of picosecond time resolution. *Adv. Funct. Mater.*, **2019,** *29,* 1807818.

54. VandenBussche, Elisah J., David J. Flannigan, Reducing radiation damage in soft matter with femtosecond-timed single-electron packets. *Nano letters*, **2019,** *19,* 6687-6694.

55. Panova, O., Ophus, C., Takacs, C. J., Bustillo, K. C., Balhorn, L., Salleo, A., Balsara, N., Minor, A. M., Diffraction imaging of nanocrystalline structures in organic semiconductor molecular thin films. *Nat. mater.*, **2019,** *18*, 860-865.

56. Panova, O., Chen, X. C., Bustillo, K. C., Ophus, C., Bhatt, M. P., Balsara, N., & Minor, A. M., Orientation mapping of semicrystalline polymers using scanning electron nanobeam diffraction. Micron, **2016**, *88*, 30-36.

57. Ophus, C., Four-dimensional scanning transmission electron microscopy (4D-STEM): From scanning nanodiffraction to ptychography and beyond. *Microsc. Microanal.*, **2019,** *25,* 563-582.

58. Agostinelli, T., Lilliu, S., Labram, J. G., Real-time investigation of crystallization and phase-segregation dynamics in P3HT: PCBM solar cells during thermal annealing. *Adv. Funct. Mater.*, **2011,** *21,* 1701-1708.

59. Dargazany, R., Khiêm, V. N., Poshtan, E. A., & Itskov, M., Constitutive modeling of strain-induced crystallization in filled rubbers. *Physical Review E*, **2014,** *89,* 022604.

60. Li, W.; Qian, X.; Li, J., Phase transitions in 2D materials. *Nat. Rev. Mater.*, **2021**, *6*, 829–846.

61. Bergeron, H., Lebedev, D., & Hersam, M. C. (2021). Polymorphism in post-dichalcogenide two-dimensional materials. *Chem. Rev.*, **2021**, *121*, 2713-2775.

62. Cho, S., Kim, S., Kim, J. H., Zhao, J., Seok, J., Keum, D. H., & Yang, H., Phase patterning for ohmic homojunction contact in MoTe2. *Science*, **2015**, *349*, 625-628.

63. Cheon, Y., Lim, S. Y., Kim, K., & Cheong, H., Structural phase transition and interlayer coupling in few-layer 1T′ and Td MoTe2. *ACS nano*, **2021**, *15*, 2962-2970.

64. Lin, Y. C., Dumcenco, D. O., Huang, Y. S., & Suenaga, K., Atomic mechanism of the semiconducting-to-metallic phase transition in single-layered MoS2. *Nat. nanotechnol.*, **2012**, *9*, 391-396.

65. Zhang, F., Zhang, H., Krylyuk, S., Milligan, C. A., Zhu, Y., Zemlyanov, D. Y., & Appenzeller, J., Electric-field induced structural transition in vertical MoTe2-and Mo1–x W x Te2-based resistive memories. *Nat. mat.*, **2019**, *18*, 55-61.

66. Yang, H., Kim, S. W., Chhowalla, M., & Lee, Y. H., Structural and quantum-state phase transitions in van der Waals layered materials. *Nat. Phys.*, **2017**. *13*, 931-937.

67. Balents, L., Dean, C. R., Efetov, D. K., & Young, A. F., Superconductivity and strong correlations in moiré flat bands. *Nat. Phys.*, **2020**, *16*, 725-733.

68. Huang, B., McGuire, M. A., May, A. F., Xiao, D., Jarillo-Herrero, P., & Xu, X., Emergent phenomena and proximity effects in two-dimensional magnets and heterostructures. *Nat. Mat.*, **2020**, *19*, 1276-1289.

69. Tang, X., & Kou, L., Two-dimensional ferroics and multiferroics: platforms for new physics and applications. *J. Phys. Chem. Lett.*, **2019**.*10*, 6634-6649.

70. Nicolosi, V., Chhowalla, M., Kanatzidis, M. G., Strano, M. S., & Coleman, J. N., Liquid exfoliation of layered materials. *Science*, **2013**, *340*, 1226419.

71. Chhowalla, M., Shin, H. S., Eda, G., Li, L. J., Loh, K. P., & Zhang, H., The chemistry of two-dimensional layered transition metal dichalcogenide nanosheets. *Nat. Chem.*, **2013**, *5*, 263-275.

72. Liu, L., Dong, J., Huang, J., Nie, A., Zhai, K., Xiang, J., & Liu, Z., Atomically resolving polymorphs and crystal structures of In2Se3. *Chem. Mater.*, **2019**, *31*, 10143-10149.

73. Van Landuyt, J., Van Tendeloo, G., & Amelinckx, S., Phase transitions in In2Se3 as studied by electron microscopy and electron diffraction. *Phys. Status Solidi A*, **1975**, *30*, 299-314.

74. Manolikas, C., New results on the phase transformations of In2Se3. *J. Solid State Chem.*, **1988**, *74*, 319-328.

75. Tao, X., Gu, Y., Crystalline–Crystalline phase transformation in two-dimensional In2Se3 thin layers. *Nano Lett.*, **2013**, *13*, 3501–3505.

76. Küpers, M., Konze, P. M., Meledin, A., Mayer, J., Englert, U., Wuttig, M., & Dronskowski, R., Controlled crystal growth of indium selenide, In2Se3, and the crystal structures of α-In2Se3. *Inorg. Chem.*, **2018,** *57*, 11775-11781.

77. Ding, W., Zhu, J., Wang, Z., Gao, Y., Xiao, D., Gu, Y., & Zhu, W., Prediction of intrinsic two-dimensional ferroelectrics in In2Se3 and other III2-VI3 van der Waals materials, *Nat. Commun.*, **2017**, *8*, 14956.

78. Novoselov, K. S., Mishchenko, A., Carvalho, A., & Castro Neto, A. H., 2D materials and van der Waals heterostructures. *Science*, **2016**, *353*, aac9439.

79. Lu, J. M., Zheliuk, O., Leermakers, I., Yuan, N. F., Zeitler, U., Law, K. T., & Ye, J., Evidence for two-dimensional Ising superconductivity in gated MoS2. *Science*, **2015**, *350*, 1353-1357.

80. Navarro-Moratalla, E., Island, J. O., Manas-Valero, S., Pinilla-Cienfuegos, E., Castellanos-Gomez, A., Quereda, J., & Coronado, E., Enhanced superconductivity in atomically thin TaS2. *Nat. Commun.*, **2016**, *7*, 11043.

81. Cao, Y., Fatemi, V., Fang, S., Watanabe, K., Taniguchi, T., Kaxiras, E., & Jarillo-Herrero, P., Unconventional superconductivity in magic-angle graphene superlattices. *Nature,* **2018***, 556*, 43-50.

82. Huang, B., Clark, G., Navarro-Moratalla, E., Klein, D. R., Cheng, R., Seyler, K. L., & Xu, X., Layer-dependent ferromagnetism in a van der Waals crystal down to the monolayer limit. *Nature*, **2017**, *546*, 270-273.

83. Gong, C., Li, L., Li, Z., Ji, H., Stern, A., Xia, Y., & Zhang, X., Discovery of intrinsic ferromagnetism in two-dimensional van der Waals crystals. *Nature*, **2017**, *546*, 265-269.

84. Xu, C., Chen, Y., Cai, X., Meingast, A., Guo, X., Wang, F., & Zhu, Y., Two-dimensional antiferroelectricity in nanostripe-ordered In2Se3. *Phys. Rev. Lett.*, **2020**, *125*, 047601.

85. Zheng, C., Yu, L., Zhu, L., Collins, J. L., Kim, D., Lou, Y., & Fuhrer, M. S., Room temperature in-plane ferroelectricity in van der Waals In2Se3. *Sci. Adv.*, **2018**, *4*, eaar7720.

86. Xu, C., Mao, J., Guo, X., Yan, S., Chen, Y., Lo, T. W., & Zhu, Y., Two-dimensional ferroelasticity in van der Waals β'-In2Se3. *Nat. Commun.*, **2021**, *12*, 3665.

87. Zhou, Y., Wu, D., Zhu, Y., Cho, Y., He, Q., Yang, X., & Lai, K., Out-of-plane piezoelectricity and ferroelectricity in layered α-In2Se3 nanoflakes. *Nano Lett.*, **2017**, *17*, 5508–5513.

88. Martin, L., Rappe, A., Thin-film ferroelectric materials and their applications. *Nat. Rev. Mater.*, **2016**, *2*, 16087.

89. Liu K, Zhang T, Dang B, et al. Liu, K., Zhang, T., Dang, B., Bao, L., Xu, L., Cheng, C., & Yang, Y., An optoelectronic synapse based on α-In2Se3 with controllable temporal dynamics for multimode and multiscale reservoir computing. *Nat. Electron.*, **2022**, *5*, 761-773.

90. Jiang, J., Zhang, L., Ming, C., Zhou, H., Bose, P., Guo, Y., & Shi, J., Giant pyroelectricity in nanomembranes. *Nature*, **2022**, *607*, 480-485.

91. Han, W., Zheng, X., Yang, K., Tsang, C. S., Zheng, F., Wong, L. W., & Zhao, J. (2023). Phase-controllable large-area two-dimensional In2Se3 and ferroelectric heterophase junction. *Nat. nanotechnol.*, **2023**, *18*, 55-63.

92. Choi, M. S., Cheong, B. K., Ra, C. H., Lee, S., Bae, J. H., Lee, S., & Yoo, W. J., Electrically driven reversible phase changes in layered In2Se3 crystalline film. *Adv. Mater.*, **2017**, *29*, 1703568.

93. Zheng, X., Han, W., Yang, K., Wong, L. W., Tsang, C. S., Lai, K. H., & Zhao, J., Phase and polarization modulation in two-dimensional In2Se3 via in situ transmission electron microscopy. *Sci. Adv.*, **2022**, *8*, eabo0773.

94. Chang, K., Liu, J., Lin, H., Wang, N., Zhao, K., Zhang, A., & Ji, S. H., Discovery of robust in-plane ferroelectricity in atomic-thick SnTe. *Science*, **2016**, *353*, 274-278.

95. Liu, F., You, L., Seyler, K. L., Li, X., Yu, P., Lin, J., & Liu, Z., Room-temperature ferroelectricity in CuInP2S6 ultrathin flakes. *Nat. Commun.*, **2016**, *7*, 1-6.

96. Zhou, Y., Wu, D., Zhu, Y., Cho, Y., He, Q., Yang, X., & Lai, K., Out-of-plane piezoelectricity and ferroelectricity in layered α-In2Se3 nanoflakes. *Nano Lett.*, **2017**, *17*, 5508-5513.

97. Peng, H., Xie, C., Schoen, D. T., Cui, Y. Large anisotropy of electrical properties in layer-structured In2Se3 nanowires. *Nano Lett.*, **2008**, *8*, 1511-1516.

98. Egerton, R. F., *Electron energy-loss spectroscopy in the electron microscope*. Springer: 2011.

99. Mecklenburg, M., Hubbard, W. A., White, E. R., Dhall, R., Cronin, S. B., Aloni, S., & Regan, B. C., Nanoscale temperature mapping in operating microelectronic devices. *Science*, **2015,** *347,* 629-632.

100. Hu, X., Yasaei, P., Jokisaari, J., Öğüt, S., Salehi-Khojin, A., & Klie, R. F. (2018). Mapping thermal expansion coefficients in freestanding 2D materials at the nanometer scale. *Phys. Rev. Lett.*, **2018,** *120,* 055902.

101. Eswara Moorthy, S. K., & Howe, J. M., Temperature dependence of the plasmon energy in liquid and solid phases of pure Al and of an Al-Si alloy using electron energy-loss spectroscopy. *J. Appl. Phys.*, **2011,** *110,* 043515.

102. Shen, L., Mecklenburg, M., Dhall, R., Regan, B. C., & Cronin, S. B., Measuring nanoscale thermal gradients in suspended MoS2 with STEM-EELS. *Appl. Phys. Lett.*, **2019,** *115,* 153108.

103. Gaulandris, F., Simonsen, S. B., Wagner, J. B., Mølhave, K., Muto, S., & Kuhn, L. T., Methods for calibration of specimen temperature during in situ transmission electron microscopy experiments. *Microsc. Microanal.*, **2020,** *26,* 3-17.

104.Egerton, R.; Rauf, I., Dose-rate dependence of electron-induced mass loss from organic specimens. *Ultramicroscopy*, **1999,** *80*, 247-254.

105.Drummy, L. F.; Yang, J.; Martin, D. C., Low-voltage electron microscopy of polymer and organic molecular thin films. *Ultramicroscopy* **2004,** *99*, 247-56.

106.Egerton, R. F.; Lazar, S.; Libera, M., Delocalized radiation damage in polymers. *Micron* **2012,** *43*, 2-7.

107.Egerton, R.; Crozier, P.; Rice, P., Electron energy-loss spectroscopy and chemical change. *Ultramicroscopy* **1987,** *23*, 305-312.

108.Bodily, D. M.; Dole, M., Ultraviolet Spectroscopy of Irradiated Polyethylene. *J. Chem. Phys.* **1966,** *45*, 1428-1432.

109.Jones Jr, L.; Taylor, L., Far ultraviolet absorption spectra of unsaturated and aromatic hydrocarbons. *Anal. Chem.* **1955,** *27*, 228-237.

110.Singh, A., Irradiation of polyethylene: Some aspects of crosslinking and oxidative degradation. *Radiat. Phys. Chem.* **1999,** *56*, 375-380.

111.Dole, M.; Cracco, F., Radiation chemistry of polyethylene. V. Hydrogen isotope exchange studies. *J. Phys. Chem.* **1962,** *66*, 193-201.

112.Clough, R. L., Isotopic exchange in gamma-irradiated mixtures of C24H50 and C24D50: Evidence of free radical migration in the solid state. *J. Chem. Phys.* **1987,** *87*, 1588-1595.

113.Waterman, D.; Dole, M., Radiation chemistry of polyethylene. X. Kinetics of the conversion of alkyl to allyl free radicals. *J. Phys. Chem.* **1970,** *74*, 1913-1922.

114.Suehiro, K.; Takayanagi, M., Structural studies of the high temperature form of trans-1, 4-polybutadiene crystal. *J. Macromol. Sci. B* **1970,** *4*, 39-46.

115.Iwayanagi, S.; Sakurai, I.; Sakurai, T.; Seto, T., X-ray structure analysis of trans-1, 4-polybutadiene. *J. Macromol. Sci. B* **1968,** *2*, 163-177.

116.Kleis, J.; Lundqvist, B. I.; Langreth, D. C.; Schröder, E., Towards a Working Density-Functional Theory for Polymers: First-Principles Determination of the Polyethylene Crystal Structure. *Phys. Rev. B* **2007,** *76*, 100201.

117.Teare, P. W., The crystal structure of orthorhombic hexatriacontane, C36H74. *Acta Crystallogr.* **1959,** 12(4), 294-300.

118.Toda, A., Okamura, M., Hikosaka, M., Nakagawa, Y. Three-dimensional shape of polyethylene single crystals grown from dilute solutions and from the melt. *Polymer* **2005,** *46,* 8708-8716.

119.Wittmann, J. C., and B. Lotz. Polymer decoration: the orientation of polymer folds as revealed by the crystallization of polymer vapors. *J. Polym. Sci. Polym. Phys. Ed.* **1985,** *23,* 205-226.

120.Weber, C. H., Chiche, A., Krausch, G., Rosenfeldt, S., Ballauff, M., Harnau, L., Single lamella nanoparticles of polyethylene. *Nano Letters* **2007,** *7,* 2024-2029.

121.Hu, Wenbing, Daan Frenkel, and Vincent BF Mathot. Intramolecular nucleation model for polymer crystallization. *Macromolecules* **2003,** *36,* 8178-8183.

122.Brinkmann, M., Structure and morphology control in thin films of regioregular poly (3-hexylthiophene). *J. Polym. Sci. B: Polym. Phys.* **2011**, 49, 1218-1233.

123.Lu, G.; Li, L.; Yang, X., Achieving Perpendicular Alignment of Rigid Polythiophene Backbones to the Substrate by Using Solvent-Vapor Treatment. *Adv. Mater*. **2007**, 19, 3594-3598.

124.Lu, G.; Li, L.; Yang, X., Morphology and crystalline transition of poly(3-butylthiophene) associated with its polymorphic modifications. *Macromolecules* **2008**, 41, 2062-2070.

125.Rahimi, K.; Botiz, I.; Stingelin, N.; Kayunkid, N.; Sommer, M.; Koch, F. P. V.; Nguyen, H.; Coulembier, O.; Dubois, P.; Brinkmann, M., Controllable processes for generating large single crystals of poly(3-hexylthiophene). *Angew. Chem. Int. Ed.*, **2012,** 51, 11131-11135.

126.Zhugayevych, A.; Mazaleva, O.; Naumov, A.; Tretiak, S., Lowest-energy crystalline polymorphs of P3HT. *J. Phys. Chem. C* **2018**, 122, 9141-9151.

127.Koch, F. P. V.; Heeney, M.; Smith, P., Thermal and structural characteristics of oligo(3-hexylthiophene)s(3HT) n, n= 4–36. *J. Am. Chem. Soc.* **2013**, 135, 13699-13709.

128.Crossland, E. J.; Tremel, K.; Fischer, F.; Rahimi, K.; Reiter, G.; Steiner, U.; Ludwigs, S., Anisotropic Charge Transport in Spherulitic Poly (3-hexylthiophene) Films. *Adv. Mater*. **2012**, 24, 839-844.

129.Sirringhaus, H.; Brown, P.; Friend, R.; Nielsen, M. M.; Bechgaard, K.; Langeveld-Voss, B.; Spiering, A.; Janssen, R. A.; Meijer, E.; Herwig, P., Two-dimensional charge transport in self-organized, high-mobility conjugated polymers. *Nature* **1999**, 401, 685-688.

130.Kline, R. J.; McGehee, M. D.; Kadnikova, E. N.; Liu, J.; Fréchet, J. M.; Toney, M. F., Dependence of regioregular poly (3-hexylthiophene) film morphology and field-effect mobility on molecular weight. *Macromolecules* **2005,** *38*, 3312-3319.

131.Cumpson, P. J., Estimation of inelastic mean free paths for polymers and other organic materials: use of quantitative structure–property relationships. *Surf. Interface. Anal.* **2001,** *31*, 23-34.

132.Iakoubovskii, K., Mitsuishi, K., Nakayama, Y., Furuya, K., Mean free path of inelastic electron scattering in elemental solids and oxides using transmission electron microscopy: Atomic number dependent oscillatory behavior. *Phys. Rev. B* **2008,** *77*, 104102.

133.Li, Q., Das Sarma, S., Finite temperature inelastic mean free path and quasiparticle lifetime in graphene. *Phys. Rev. B* **2013,** *87*, 085406.

134.Al-Ibrahim, M., Roth, H.-K., Schroedner, M., Konkin, A., Zhokhavets, U., Gobsch, G., Scharff, P., Sensfuss, S., The influence of the optoelectronic properties of poly (3-alkylthiophenes) on the device parameters in flexible polymer solar cells. *Org. Electron.* **2005,** *6*, 65-77.

135.Bustillo, K. C., Zeltmann, S. E., Chen, M., Donohue, J., Ciston, J., Ophus, C., & Minor, A. M., 4D-STEM of beam-sensitive materials. *Acc. Chem. Res.*, **2021**, *54*, 2543-2551.

136.Guo, M., Guo, C., Han, J., Chen, S., He, S., Tang, T., & Shen, Y., Toroidal polar topology in strained ferroelectric polymer. *Science*, **2021,** 371, 1050-1056.

137.Crist, B., Schultz, J. M. Polymer Spherulites: A Critical Review. *Prog. Polym. Sci.* **2016**, *56*, 1–63.

138.Xu H, Keawwattana, W, Kyu T., Effect of thermal transport on spatiotemporal emergence of lamellar branching morphology during polymer spherulitic growth. *J. Chem. Phys.* **2005,** *123,* 124908.

139.Armistead, J. P., & Hoffman, J. D., Direct evidence of regimes I, II, and III in linear polyethylene fractions as revealed by spherulite growth rates. *Macromolecules* **2002,** *35,* 3895-3913.

140.Mareau, V.H., Prud'homme, R.E., In-situ hot stage atomic force microscopy study of poly(ε-caprolactone) crystal growth in ultrathin films. *Macromolecules* **2005**, *38*, 398–408.

141.Kuzay, Tuncer M., Michael Kazmierczak, & B. J. Hsieh. X-ray beam/biomaterial thermal interactions in third-generation synchrotron sources. *Acta Cryst. D* **2001**, 57, 69-81.

142.Igo, J., Zhou, S., Yu, Z. G., Amnuayphol, O. P., Zhao, F., & Gu, Y., Anharmonic phonon coupling in single-crystal semiconducting and metal-like van der Waals In2Se3. *J. Phys. Chem. C*, **2018,** *122*, 22849-22855.

143.Gržeta, B., Popović, S., Cowlam, N., & Čelustka, B., Low-temperature X-ray diffraction examination of In2Se3. *J. Appl. Cryst.*, **1990,** *23*, 340-341.

144.Balakrishnan, N., Staddon, C. R., Smith, E. F., Stec, J., Gay, D., Mudd, G. W., & Beton, P. H., Quantum confinement and photoresponsivity of β-In2Se3 nanosheets grown by physical vapour transport. *2D Materials*, **2016,** *3*, 025030.

145.Li W, Sabino F P, de Lima F C., Large disparity between optical and fundamental band gaps in layered In2Se3. Phys. Rev. B, **2018,** *98*, 165134.

146.Muller, D. A., & Silcox, J., Delocalization in inelastic scattering. *Ultramicroscopy*, **1995,** *59*, 195-213.

147.Nakagawa, N., Hwang, H. & Muller, D., Why some interfaces cannot be sharp. *Nature Mater.*, **2006,** *5*, 204–209.

148.Wang, Z., Chen, C., Wang, D., Zhu, Y., & Zhang, B., Stabilizing Interfaces in High-Temperature NCM811-Li Batteries via Tuning Terminal Alkyl Chains of Ether Solvents. *Angew. Chem. Int. Ed.*, **2023,** e202303950.

149.Lyu, F., Sun, Y., Yang, Q., Tang, B., Li, M., Li, Z., & Chen, Q., Thickness-dependent band gap of α-In2Se3: from electron energy loss spectroscopy to density functional theory calculations. *Nanotechnology*, **2020,** *31*, 315711.

150.Li, C. F., Li, Y. Q., Tang, Y. S., Zheng, S. H., Zhang, J. H., Zhang, Y., & Liu, J. M., Band structure, ferroelectric instability, and spin–orbital coupling effect of bilayer α-In2Se3. *J. Appl. Phys.*, **2020,** *128*, 234106.

151.Collins, J. L., Wang, C., Tadich, A., Yin, Y., Zheng, C., Hellerstedt, J., & Edmonds, M. T., Electronic band structure of in-plane ferroelectric van der Waals β′-In2Se3. *ACS Appl. Electron. Mater.*, **2020,** *2*, 213-219.

152.Almeida, G., Dogan, S., Bertoni, G., Giannini, C., Gaspari, R., Perissinotto, S., & Manna, L., Colloidal monolayer β-In2Se3 nanosheets with high photoresponsivity. *J. Am. Chem. Soc.*, **2017,** *139*, 3005-3011.

153.Wu, D., Pak, A. J., Liu, Y., Zhou, Y., Wu, X., Zhu, Y., & Lai, K., Thickness-dependent dielectric constant of few-layer In2Se3 nanoflakes. *Nano Lett.*, **2015,** *15*, 8136-8140.

154.Lyu, F., Li, X., Tian, J., Li, Z., Liu, B., & Chen, Q., Temperature-Driven α-β Phase Transformation and Enhanced Electronic Property of 2H α-In2Se3. *ACS Appl. Mater. Interfaces*, **2022,** *14*, 23637-23644.

155.Liang, W. Y., Cundy, S. L., Electron energy loss studies of the transition metal dichalcogenides. *Philos. Mag.*, **1969,** *19*, 1031-1043.

156.Kapetanakis, M. D., Zhou, W., Oxley, M. P., Lee, J., Prange, M. P., Pennycook, S. J., & Pantelides, S. T., Low-loss electron energy loss spectroscopy: an atomic-resolution complement to optical spectroscopies and application to graphene. *Phys. Rev. B*, **2015,** *92*, 125147.

157.Julien, C., Eddrief, M., Kambas, K., Balkanski, M., Electrical and optical properties of In2Se3 thin films. *Thin Solid Films*, **1986,** *137*, 27-37.

158.Yan, S., Xu, C., Zhong, C., Chen, Y., Che, X., Luo, X., Zhu, Y., Phase Instability in van der Waals In2Se3 Determined by Surface Coordination. *Angew. Chem. Int. Ed.*, **2023,** *62*, e202300302.

159. Watanabe Y., Kaneko S., Kawazoe H., Yamane M., Imperfections in amorphous chalcogenides. IV. A model of electrical conduction processes in amorphous and crystalline In2Se3. *Phys. Rev. B*, **1989,** *40*, 3133.

160. Simsek, S, Mamedov, A. M., Ozbay, E., Electron Energy-Loss Spectroscopy and the Electronic Structure of ABO3 Ferroelectrics: First Principle Calculations. *arXiv preprint*, **2012,** arXiv:1204.4024.